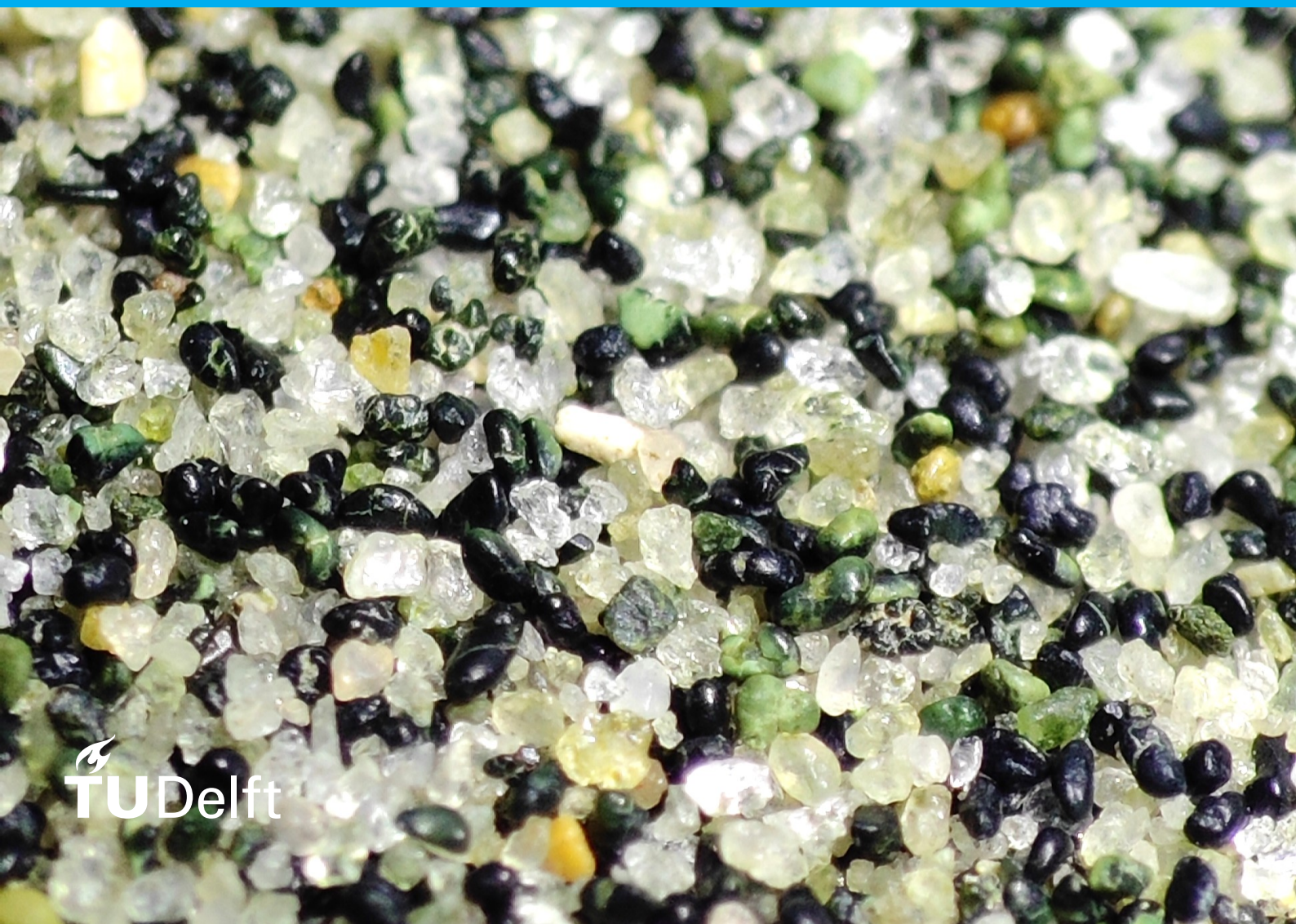
First steps into the calibration chamber pile tests with glauconitic sands

On the behaviour of the sand fraction from glauconitic sand of the Kattendijk formation in Antwerp, Belgium

Alba Rodríguez Piedrabuena



TU Delft

First steps into the calibration chamber pile tests with glauconitic sands

On the behaviour of the sand fraction from glauconitic sand of the Kattendijk formation in Antwerp, Belgium

by

Alba Rodríguez Piedrabuena

to obtain the degree of Master of Science in Civil Engineering
at the Delft University of Technology,
to be defended publicly on Friday March 8, 2024 at 10:45 AM.

Student number:	5629225	
Project duration:	March 2023 – December 2023	
Thesis committee:	Prof. dr. ir. K.G.G. Gavin,	TU Delft
	Dr. Ir. E. Kementzetzidis,	TU Delft
	Ir. M. Mento,	IQIP
	Dr. ir. J. van Wijk,	IQIP

An electronic version of this thesis is available at http://repository.tudelft.nl/.

TU Delft

Abstract

The Global Wind Energy Council (GWEC) forecasts an accelerated increase in wind installations as a result of the aggressive climate change and green energy objectives set by the majority of countries. As a consequence, new regions worldwide that were previously thought to be unsuitable for the construction of offshore wind farms due to the soil characteristics are planned to be explored. This is the case of glauconite sands, which include glauconite pellets that are very susceptible to crushing. The crushing transforms the coarse-grained sand into a fine-grained soil, changing the geotechnical characteristics of the soil. This poses particular geotechnical challenges, since the soil-structure interaction between the pile being driven and the sand changes, the side friction increases with depth and the prediction of blow counts in drivability analyses is underpredicted. In addition to this, the glauconitic sand influences the response in cone penetration tests (CPTs), characterised by high cone tip resistance (q_c) and sleeve frictions (f_s), leading to high friction ratios (R_f) and resulting in misleading soil classifications. IQIP, as a company specialised in installation and foundation projects internationally that provides innovative and high-quality equipment and solutions for construction projects related to Offshore Wind industry, is interested in better understanding the mechanical behaviour of glauconite sand during pile installation due to the risks posed by this sand, e.g. premature pile installation refusal. In order to understand this soil that poses geotechnical challenges, laboratory test programs should be designed in order to capture the soil behaviour and physical modelling is a cost effective and valuable tool. This research aims to obtain detailed information on the soil response of glauconitic sand in saturated conditions during pile installation with a new sample preparation method for glauconitic sand containing fines. It will investigate the feasibility of cone penetration testing, cyclic loading, pile driving, as well as the analysis of the shear band and grain crushing around the instrumentation penetrated in the sample in a calibration chamber (CC). Based on the results from the three performed tests it could be concluded that the preparation method led to a good procedure to prepare repeatable and homogeneous samples under fully saturated conditions, as well to a representative response to pile penetration. With this, it is possible to perform further research on the sand fraction of glauconitic sands using the same sample preparation method and testing equipment.

Preface

As I write this, my mind is recapping all the moments I lived at this university since the day I arrived, from meeting my colleagues to the excitement of passing the last exams. Now, finishing the master brings up emotions and I think about the Alba that started 2,5 years ago and I am proud of her. I also think about the beginning of this research, when glauconite was unknown to me. I challenged myself embarking into this project and I can definitely say it was worth it. Through this 11 months of endeavor, I explored laboratory testing and practical research, as I improved my programming skills. I have also learned that struggling is part of the process, that there is never a unique solution and, what I like the most, that researching is endless.

I would like to express my gratitude to IQIP, specially Jort and Mirko, for giving me the opportunity to take part in the geotechnical team since my internship until the end this research. Mirko, thank you for supervising me during my internship and relying on me for starting the first tests of your PhD. I wish you a lot of success in the continuity of your investigation. Also, to all the colleagues from IQIP who have always supported me and from who I have learnt since I started my internship at the company.

My supervisor, Ken Gavin, to whom I am very grateful to be my supervisor and my mental support in those meetings in which I was feeling down. Thank you for suggesting performing experimental research, for sharing all your knowledge and for teaching me that ambition is great but always step by step.

To Vagelis, who woke up my interest for Offshore engineering during his lectures and gave me advice during the meetings we had together.

I would like to thank Deltares for providing the installations and equipment needed to perform the tests. My appreciation goes to all the technicians and researchers that helped me during all this time in the laboratory making me feel like one of them. Without them, the experiments would not have been possible. Their experience was essential in this research, and I learned valuable lessons both personal and professionally. Thank you for your warm and inviting stay.

I want to express my sincere appreciation to Dirk de Lange, who was my main support during all the time in the laboratory and without him this research could not have been possible. Your passion for science and research motivates and encourages the people around you.

Miguel Cabrera, I appreciate you transmitting so much calm in the few conversations we have had. Also, for coming to the laboratory and sharing your experimental knowledge, showing interest and supporting me during this time.

Appreciate to the company Lantis, specially Wim van Riel and Benoît Stuyck, for helping providing the sand. It was great news and it made us all very happy knowing the research could start after obtaining the material.

I want to thank my family whose support during the whole master was essential for me. Despite the distance, I always feel you close.

To my boyfriend, with whom I have been sharing my life since some years now and together we encourage to be the best version of ourselves.

To all my friends, especially the ones that have been also working on their MSc thesis at the same time as me, who encouraged me during all this time to do the best of myself and supported me.

And to you, dear reader. I sincerely hope that you can feel the passion and dedication I put in this research and that you find enjoyment and inspiration in the following pages.

Alba Rodríguez Piedrabuena
Delft, March 2024

Contents

1 Introduction **1**
1.1 Outline of the report . . . 2

2 Literature review **3**
2.1 Pile driving in clay . . . 3
2.2 Pile driving in sand . . . 5
2.3 Glauconite sand . . . 6
2.3.1 Composition and formation . . . 6
2.3.2 Mechanical properties . . . 9
2.3.3 Geotechnical challenges with glauconite sand . . . 11

3 Thesis statement **14**
3.1 Problem description . . . 14
3.2 Hypothesis . . . 14
3.3 Experimental approach and goal of the experiment . . . 14
3.4 Material: glauconitic sand from the Kattendijk formation . . . 15

4 Characterisation and soil preparation **17**
4.1 General description of test material . . . 17
4.1.1 Glauconite pellets . . . 18
4.1.2 Geotechnical characterisation: as-received soil . . . 19
4.2 Soil preparation: removal of fines . . . 21
4.2.1 Description of the process . . . 21
4.2.2 Geotechnical characterisation: sand fraction . . . 22
4.2.3 Discussion . . . 23

5 Chamber test **25**
5.1 Experimental setup . . . 25
5.2 Cone . . . 26
5.3 Instrumented pile . . . 27
5.4 Test procedure . . . 28
5.4.1 Sample preparation . . . 28
5.4.2 Pressurizing and consolidating the sample . . . 31
5.5 Testing program . . . 31
5.5.1 Initial conditions . . . 32
5.5.2 Cone penetration test (CPTu) . . . 33
5.5.3 Impact driving . . . 33
5.5.4 Jacking . . . 33
5.6 Local relative density measurements . . . 34

6 Results **35**
6.1 Local relative density measurements after tests . . . 35
6.2 Test 1 - CPTu . . . 35
6.2.1 Static CPTu . . . 36
6.2.2 Cyclic CPTu - 0,1Hz and 1Hz . . . 37
6.3 Test 2 - Impact driving . . . 42
6.4 Test 3 - Jacking . . . 43
6.5 Shear band and tip . . . 44
6.5.1 Test 1 - CPTu Static and cyclic . . . 45
6.5.2 Test 2 - Impact driving . . . 47
6.5.3 Test 3 - Jacking . . . 47

6.6 Crushing of the glauconite pellets . . . 49
6.7 Discussion of the results . . . 50

7 Conclusions and recommendations 54
7.1 Conclusions . . . 54
7.2 Recommendations . . . 55

References 56

Appendix 58

A Site investigation data 59

B Geotechnical characterisation 63
B.1 Particle size distribution (PSD) analysis . . . 63
B.2 Specific gravity, G_s . . . 63
B.3 Maximum and minimum density . . . 65

C Calibration chamber setup 70
C.1 Bottom ring . . . 70
C.2 Sensors . . . 71
C.2.1 Pore pressure transducers . . . 71
C.2.2 Pressure transducer of the membrane . . . 72
C.3 Inner lining installation . . . 72
C.3.1 Foam installation . . . 72
C.3.2 Membrane installation . . . 73
C.4 Top plate . . . 74
C.4.1 CPT and jacking . . . 74
C.4.2 Impact driving . . . 74

D Cone drawing 75

E Description of the tests 76
E.1 Test 1: Cone penetration test (CPTu) . . . 76
E.1.1 Test 2: Impact driving . . . 77
E.1.2 Test 3: Jacking . . . 78

F Relative density 80
F.1 Relative density, D_{rel} . . . 80

G Additional measurements Test 1 83
G.1 Pore pressure, u_2, after static CPTu . . . 85
G.2 Pore pressure, u_2, after cyclic CPTu at 0,1 Hz . . . 85
G.3 Pore pressure, u_2, after cyclic CPTu at 1 Hz . . . 86

H Additional measurements Test 2 87

I Additional measurements Test 3 90

Nomenclature

γ_d	Dry unit weight of the soil	[kN/m^3]
γ_t	Unit weight of the soil	[kN/m^3]
γ_w	Unit weight of water	[kg/m^3]
ρ_d	Dry density of the soil	[g/cm^3]
ρ_t	Bulk density	[g/cm^3]
ρ_w	Density of water at 20ºC equal to 1	[g/cm^3]
σ_h	Horizontal stress	[kPa]
σ_v	Vertical stress	[kPa]
Δw_{cyclic}	Cyclic displacement half-amplitude	[mm]
h/D	Distance from the pile tip normalised by the pile width	[-]
B_{inring}	Inner diameter rings	[mm]
B_{soil}	Diameter of soil sample	[mm]
D	Pile diameter	[mm]
D_{rel}	Relative density	[%]
e	Void ratio	[-]
E1	Total pressure transducer side North at h/D = 3,6	[kPa]
E2	Total pressure transducer side North at h/D = 1,6	[kPa]
E3	Total pressure transducer side North at h/D = 0,4	[kPa]
E4	Total pressure transducer side South at h/D = 3,4	[kPa]
E5	Total pressure transducer side South at h/D = 1,6	[kPa]
E6	Total pressure transducer side South at h/D = 0,4	[kPa]
g	Acceleration of gravity equal to 9,81	[m/s^2]
G_s	Specific gravity	[g/cm^3]
h	Distance from the pile tip	[mm]
H_{soil}	Height of soil sample	[mm]
L_{depth}	Embedded pile length	[mm]
L_{pile}	Length of the pile	[mm]
M_1	Mass of the bowl	[g]
M_2	Mass of the bowl and humid soil	[g]
M_3	Mass of the bowl and dry soil	[g]

M_s	Mass of the soil	[g]
PPT_1	Pore pressure transducer at depth 440mm	[kPa]
PPT_2	Pore pressure transducer at depth 290mm	[kPa]
PPT_3	Pore pressure transducer at depth 140mm	[kPa]
Pt100	Temperature sensor	ºC
V_c	Volume calibration chamber	[m^3]
V_s	Volume of the soil	[cm^3]
W	Sample soil weight	[kg]
w	Water content of the soil sample	[%]

Chapter 1

Introduction

Over the previous forty years, the wind industry has changed radically and according to the International Energy Agency (IEA), almost all of the additional electricity generated between 2022 and 2025 is expected to originate from renewable energy sources. Moreover, due to the aggressive climate change and green energy objectives set by the majority of countries, the Global Wind Energy Council (GWEC) forecasts an accelerated increase in wind installations since, for the first time, more than 25GW will be installed offshore in a single year in 2025, as well as more than 1000GW onshore by 2024 (GWEC, 2023). Moreover, worldwide, 680GW of wind capacity are expected to be added between 2023 and 2027, from which 130GW will be generated in offshore wind farms (Figure 1.1). In addition to this, 2000GW of offshore wind capacity is estimated by 2050 in order to achieve Paris Agreement objectives (IRENA and GWEC, 2021).

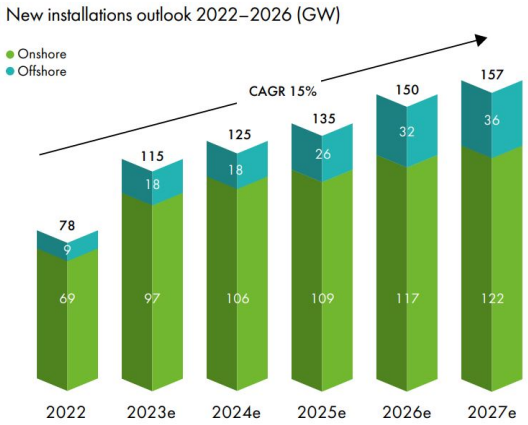


Figure 1.1: Industry perspective for expected installations of new capacity between 2022 and 2027, based on GWEC's Market Outlook, indicating a compound annual growth rate of 15%. (Figure from GWEC, 2023).

Nonetheless, the pace and scale of the aforementioned ambitions present, among others, offshore geotechnical challenges (Gourvenec, 2023b). Figure 1.2 shows an indication of associated geotechnical requirements for the expected growth in offshore wind by 2050, regarding the offshore wind capacity, the number of turbines, foundation and anchor designs, the area of the seabed to be characterised and CPTs needed and the number of element tests (Gourvenec, 2023a). Moreover, this includes exploring new regions worldwide that were previously thought to be unsuitable for the construction of offshore wind farms due to the soil characteristics. This is the case of glauconite sands, which include glauconite pellets that are very susceptible to crushing. The crushing transforms the coarse-grained sand into a fine-grained soil, thus showing a change in permeability and strength, a strong thixotropic behaviour and a reduction in shear strength (Westgate, McMullin, and DeGroot, 2022). This poses particular geotechnical challenges, as observed by different authors (De Nijs et al., 2015, Perikleous et al., 2023, Westgate, McMullin, and DeGroot, 2022), since the soil-structure interaction between the pile being driven and the sand changes, the pile capacity reduces with depth, the side friction increases with depth and the prediction of blow counts in drivability analyses is underpredicted. In addition to this, the glauconitic sand influences the response in cone penetration tests (CPTs), characterised by high cone tip resistance (q_t) and sleeve frictions (f_s), resulting in misleading soil classifications.

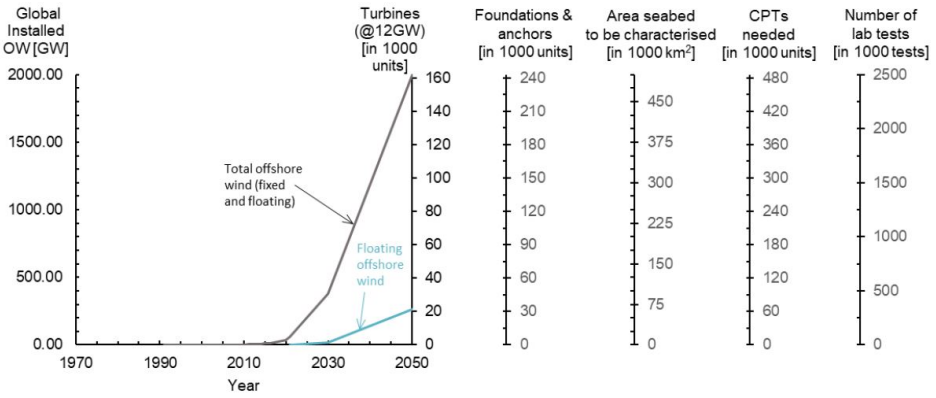


Figure 1.2: Indication of the associated geotechnical requirements for the global offshore wind ambitions by 2050 (Gourvenec, 2023a)

IQIP, as a company specialised in installation and foundation projects internationally that provides innovative and high-quality equipment and solutions for construction projects related to Offshore Wind industry, is interested in better understanding the mechanical behaviour of glauconite sand during pile installation, due to the risks posed by this sand, e.g. premature pile installation refusal (Westgate, McMullin, and DeGroot, 2022). In order to understand these soils that pose geotechnical challenges, laboratory test programs should be designed in order to capture the soil behaviour and physical modelling is a cost effective and valuable tool. Therefore, future research should focus on soils that pose relevant engineering problems, such as crushable soils, like is the case of glauconite sands. This is the reason why this research focuses in the performance of several tests with glauconitic sand in a calibration chamber (CC), where the boundary conditions are well controlled. It should be noted that from this point, the sand used for testing is referred to as *glauconitic* according to geological terminology, due to its low glauconite content (<30%) (Westgate, DeGroot, et al., 2023).

1.1. Outline of the report

Glauconite sands undergo large degradation levels during pile driving operations (Westgate, DeGroot, et al., 2023) due to the transformation from a coarse-grained soil to a clay-soil type, leading to a pile drivability process that starts in sandy soil and evolves to a silty/clayey soil. Moreover, in sandy soils the end-bearing resistance or cone resistance (q_c) is high, and the sleeve friction (f_s) is small, leading to relatively small friction ratio (R_f) values. On the other hands, in glauconitic sands q_c are large, in combination with high f_s that lead to high R_f. Therefore, this report starts explaining the processes of pile driving in clay and sand followed by an introduction into the glauconite sand, including an explanation on the global distribution, its composition and formation, mechanical properties and geotechnical challenges.

To continue, as a result of the literature review and the analysis of the received soil, in Chapter 3 the research questions are formulated, together with the hypothesis and the explanation of the experimental approach followed and the goal of the experiment and the material used for the research. The latter is explained in more detail in Chapter 4. This chapter focuses only on the analyses of the glauconitic sand, the soil preparation prior to sample preparation and a detailed characterisation of the soil including descriptions of the laboratory tests.

Chapter 5 includes all the information regarding the calibration chamber tests, including the setup, the cone and instrumented pile being penetrated through the soil, the test procedure and the testing program.

To finish, Chapter 6 includes all the results regarding the sample preparation and tests performed in the calibration chamber and Chapter 7 includes the conclusions obtained and some recommendations for further research.

Chapter 2

Literature review

2.1. Pile driving in clay

Randolph and Gourvenec (2011) describe the life cycle of a driven pile in clay in five separate stages (Figure 2.1). Firstly, importance should be given to the overconsolidation ratio (OCR) of the clay since its mechanical behaviour under shearing, and therefore, the final capacity of the pile, will differ depending on its stiffness. In case of a stiff or overconsolidated clay (OC), it will tend to dilate whereas a soft or normally consolidated clay (NC) will tend to contract upon shearing.

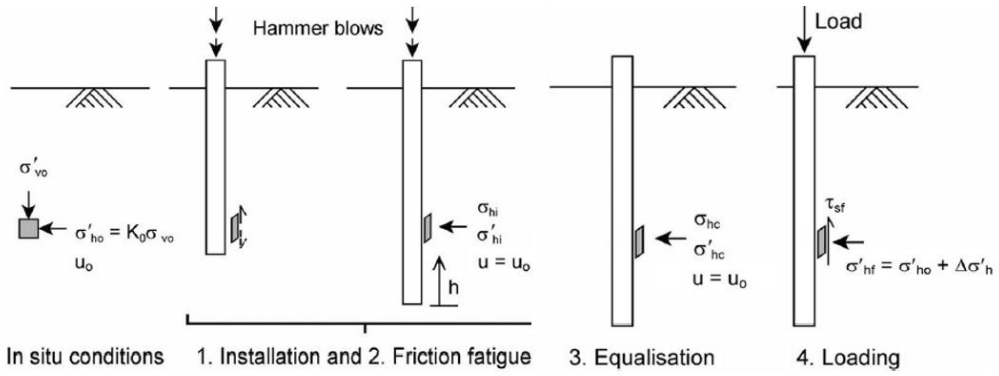


Figure 2.1: Driven pile in clay: installation and loading stages. (Figure from Randolph and Gourvenec (2011)).

When the displacement pile is driven into the clay, the soil from the immediate area surrounding the pile will be pushed outwards in order for the pile to be accommodated and it will undergo high shear strains. Therefore, this leads to an increment of total stresses, which amount will depend on the undrained shear strength (s_u) of the clay, typically ranging from 4 to 6 times s_u. The displaced soil will lead to a high degree of remoulding and hence, a residual shear plane may deform adjacent to the shaft (Bond and Jardine, 1991). This is considered an undrained process, where the condition of no volume change is kept, leading to the generation of excess pore pressures arising, firstly, from the aforementioned increase of total stresses and, secondly, as a result of the shearing of the soil that causes changes in mean effective stress. The shearing process, however, will contribute positively to the excess pore pressure in case of a soft or NC clay, whereas in case of a stiff or OC clay, the contribution will be negative. As a result, the horizontal effective stress acting on the pile immediately after installation will be higher in the case of stiff (OC) clays, due to their tendency to dilate and suck water in, in comparison to the soft (NC) clays that will tend to contract and expel water upon shearing. Due to the latter tendency, and the reduction of horizontal effective stresses in the soil, these are lower at points that have experienced more shearing cycles during driving, in this case, the further points from the pile tip. Heerema (1978) described this phenomena of reduction of shaft resistance with the influence of larger distances from the tip as 'friction fatigue'. After the installation of the pile, the effective stresses change as a result of the dissipation of the excess pore pressures generated, and with it, the shaft resistance. The more impermeable the clay is, the longer the equalisation process takes. In case of a silty clay,

this can take minutes.

During pile loading, shaft friction along the pile is mobilised. The limiting shaft friction (τ_{sf}) is determined by the local radial effective stress at failure (σ'_{rf}) and the interface friction angle (δ) and follows Coulomb's failure criterion as follows:

$$\tau_{sf} = \sigma'_{rf} tan\delta \tag{2.1}$$

From τ_{sf}, the ultimate shaft resistance (Q_{sf}) is calculated as follows:

$$Q_{sf} = \pi D \int_0^L \tau_{sf}\, dz \tag{2.2}$$

Being:			
	τ_{sf}	Local unit shaft resistance at failure	[kPa]
	σ'_{hf}	Horizontal effective stress at failure	[kPa]
	δ	Interface friction angle	[º]
	Q_{sf}	Ultimate shaft resistance	[kN]

According to the American Petroleum Institute (API, 1993) guidelines, the ultimate shaft friction (τ_{sf}) can be estimated using two approaches:

- **Alpha method**
  The correlation between the shaft friction (τ_{sf}) and the undrained shear strength (s_u) in this approach is:

  $$\tau_{sf} = \alpha s_u \tag{2.3}$$

  This method distinguishes between soft (NC) and stiff (OC) clays, since their contractive or dilative behaviour, respectively, will affect the stresses. In this approach, α is correlated to with the strength ratio (s_u / σ'_{v0}) as follows:

  $$\text{For soft (NC) clays, } s_u < \sigma'_{v0} : \alpha = \frac{1}{2}\left(\frac{s_u}{\sigma'_{v0}}\right)^{-1/2} \quad \Rightarrow \quad \tau_{sf} = \frac{1}{2}\sqrt{s_u \sigma'_{v0}} \tag{2.4}$$

  $$\text{For stiff (OC) clays, } s_u > \sigma'_{v0} : \alpha = \frac{1}{2}\left(\frac{s_u}{\sigma'_{v0}}\right)^{-1/4} \quad \Rightarrow \quad \tau_{sf} = \frac{1}{2} s_u^{0.75} \sigma'_{v0} \tag{2.5}$$

- **Beta method**
  This approach expresses the shaft friction (τ_{sf}) in terms of effective stresses as follows:

  $$\tau_{sf} = \beta \sigma'_{v0} = K \sigma'_{v0} tan\delta = \sigma'_{hf} tan\delta \tag{2.6}$$

  To correlate α and β, the aforementioned strength ratio (s_u / σ'_{v0}) is used:

  $$\beta = \alpha \left(\frac{s_u}{\sigma'_{v0}}\right) \tag{2.7}$$

The ultimate base resistance (Q_{bf}) is calculated from the bearing capacity (q_{bf}):

$$Q_{bf} = \frac{\pi D^2}{4} q_{bf} \tag{2.8}$$

$$q_{bf} = N_c s_u \frac{\pi D^2}{4} q_{bf} \tag{2.9}$$

Being:			
	q_{bf}	Bearing capacity	[kPa]
	Q_{bf}	Ultimate base resistance	[kN]
	N_c	Empirical deep bearing capacity factor (N_c = 9) (Skempton, 1951)	[-]
	s_u	Undrained shear strength	[kPa]

2.2. Pile driving in sand

In comparison to pile driving in clay, due to the permeability of sand, pile driving in sand does not consider an equalisation stage in which excess pore pressures generated during installation need to be dissipated, since it is a drained process where water can drain freely and changes in volume can occur. Nonetheless, the in situ conditions and the stress changes during installation and loading need to be analysed. In Figure 2.2, a summary of the stages of pile driving in sand is shown.

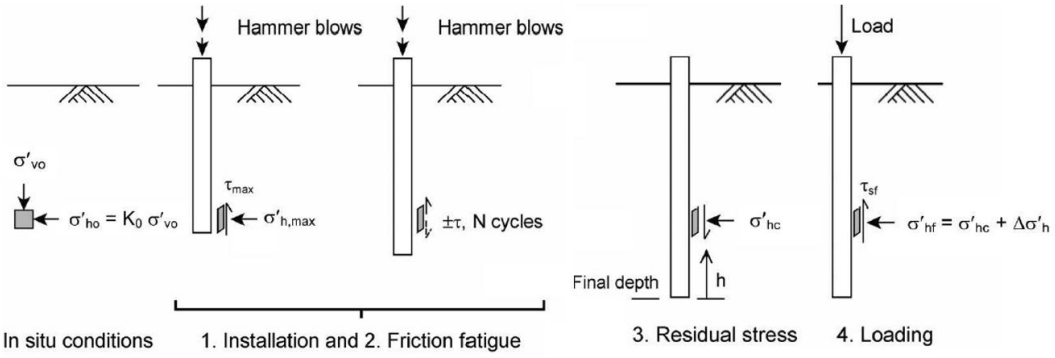


Figure 2.2: Driven pile in sand: installation and loading stages (White, 2005).

While the displacement pile is driven into the sand, the sand particles around the pile tip are pushed away radially to allow the penetration and accommodation of the pile, and they reach the pile shaft (Figure 2.3). This leads, first, to an increase in stress levels, followed by a drop due to the sand being pushed outwards. The former stresses are comparable to the cone resistance (q_c) reading of a cone penetration test (CPT), and the latter to the sleeve friction (f_s). During pile installation, the soil around the pile will tend to contract, since the cyclic shearing is applied in drained conditions with volume changes allowed. As a result, a reduction in the horizontal stresses acting on the shaft will occur and lead to the aforementioned process of 'friction fatigue' (Heerema, 1978.) This causes a decrease in unit shaft resistance as the distance behind the tip is larger. This mobilised shaft friction also follows Coulomb's failure criterion from equation 2.1. After installation, the presence of residual stresses at the pile base and at the shaft close to it will appear as a consequence of the decompression of the soil after no the disturbance of the soil (Fellenius, 2015).

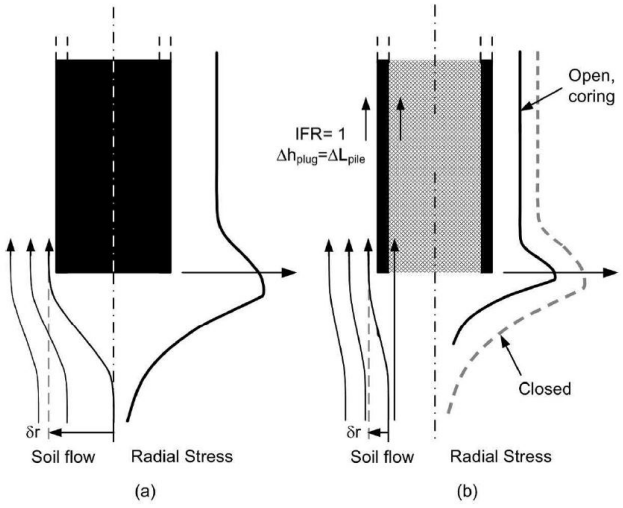


Figure 2.3: Scheme of the soil flow streamlines in a) closed-ended pile, b) open-ended pile (unplugged) (White, 2005).

The ultimate shaft friction (τ_{sf}) can be estimated according to the American Petroleum Institute (API, 1993) guidelines using equation 2.6 from the 'Beta method', and the toe resistance (q_b) is calculated

as follows:

$$q_b = N_q \sigma'_{v0} \tag{2.10}$$

Being: q_{bf} Bearing capacity [kPa]
N_q Dimensionless bearing capacity factor (API, 1993) [-]

2.3. Glauconite sand

2.3.1. Composition and formation

Glauconite sand, often referred to as greensand, consists of a green peloidal sand-size grains (G. S. Odin and Matter, 1981) composed of mineral glauconite and other mineral peloids such as quartz, feldspar and 2:1 interlayer deficient mica clay (López-Quirós et al., 2020). The molecular structure of the glauconite mineral is:

$$K_{x+y}(Si_{a-x}, Al_x)_{\sim 4}(Fe^{3+}, Al, Mg, Fe^{2+})_{\sim 2}O_{10}(OH)_2$$

Where x ranges between 0,2 and 0,6 and the sum of dioctahedral cations, y, ranges between 0,4 to 0,6. (Thompson, 1975). These iron potassium mica peloids are mainly characterised by its morphology variability and its chemical and physical properties (G. S. Odin and Matter, 1981).

Banerjee et al. (2020) described four main zones where glauconite formed across the world during the Paleogene Period, which account for more than 90% of the global record: A) North American continental margin, B) Paleo-Tethys (including North Africa, parts of South Europe, Middle East and East India), C) Paleo-North Sea (from the United Kingdom to northern Germany), and D) High southern latitudes (including New Zealand, eastern Tasman Plateau and Argentina) (2.4). Their study showed formations of glauconite occurring mainly on the well-developed continental margin on the northern hemisphere.

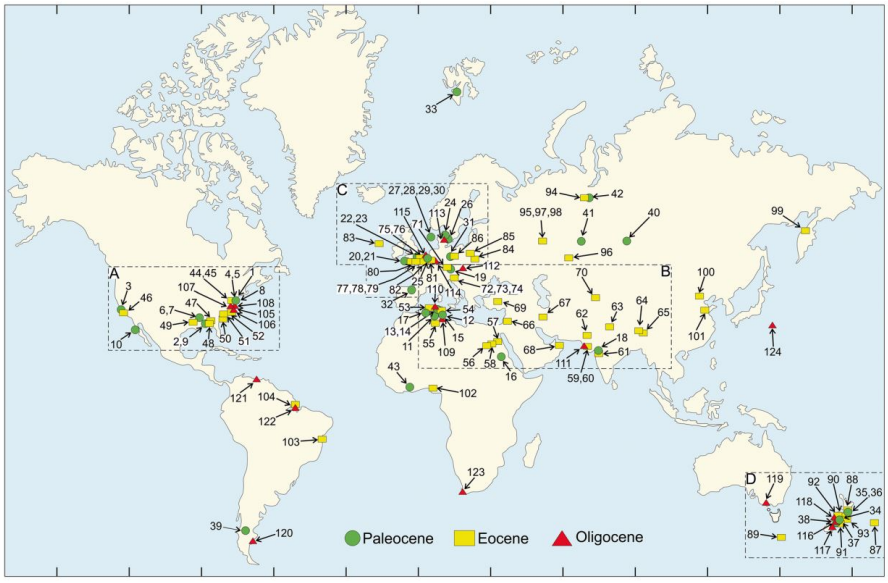


Figure 2.4: Global distribution of Paleogene glauconite. The four main zones are marked in the map. (The numbers belong to the 124 occurrences presented in their study) (Figure from Banerjee et al. (2020))

Authors have described the formation of glauconite minerals originating mainly from porous granular substrate particles found in organic matter such as fecal pellets (Figures 2.6a and 2.6b) and bioclasts (Banerjee et al., 2016; López-Quirós et al., 2020) although they can also be formed through the transformation of other particles, for instance, foraminiferal, carbonate particles and other mineral grains and rock fragments (G. S. Odin and Matter, 1981). It is still unclear how and when exactly glauconite genesis occurs (López-Quirós et al., 2020) and the present widely recognized theory for the origin

and evolution of glauconite is from G. S. Odin and Matter (1981) (López-Quirós et al., 2020). The *Precipitation-dissolution-recrystallization theory* dates back from 1981 and it comprises four stages of evolution process, namely (1) nascent, (2) slightly evolved, (3) evolved and (4) highly evolved (G. S. Odin and Matter, 1981). According to G. S. Odin and Matter (1981) and Obasi et al. (2011), this classification can be described as shown in the next Figure 2.5, with the following explanation:

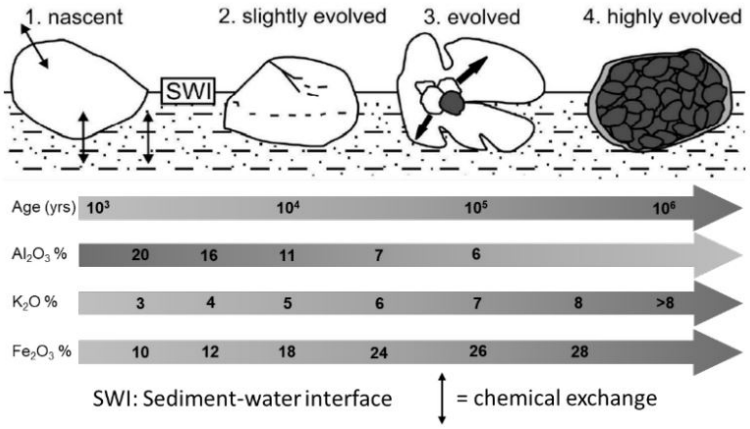
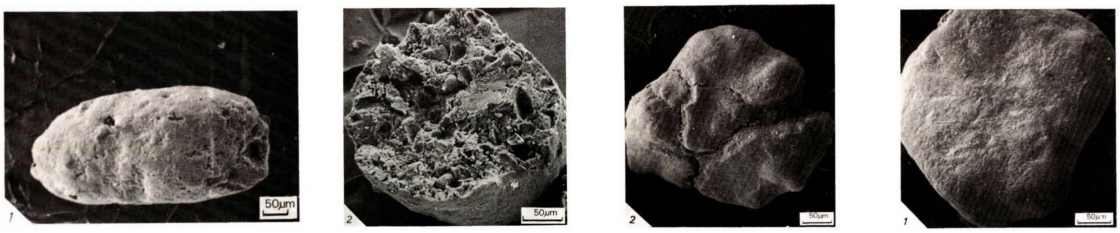


Figure 2.5: Evolution of the stages of glauconite maturity and mineralogy: 1) iron enrichment and low K_2O concentration, 2) glauconite streaks form within the particle, 3) cracking of the particle to allow K^+ difussion into the center of the particle and start of neoformation of glauconite outwards the pellet and 4) complete precipitation of bulbous glauconite and maximum potassium concentration. (Figure from Westgate, McMullin, and DeGroot (2022); modified after Obasi et al. (2011) and López-Quirós et al. (2020). As described by Obasi et al. (2011))

- **Nascent:** In this initial granular and highly porous substrate with pores between 5 $\sim$ 10 μm size, is where the first green crystals of iron and potassium rich glauconitic smectites start to grow in the simple and soft pellet shape leading to a light green colored particle. The organic matter and amount of aluminium decreases, and the particles becomes softer.
- **Slightly evolved:** The decrease of organic matter continues and the amount of iron and potassium keep increasing since the pores of the particle are completely filled with the crystals. The particles become darker, similarly to an olive-green color, and harder.
- **Evolved:** Shape and textural changes occur in the particles which look deformed resembling rosettes and they are cracked due to further recrystallisation (Figure 2.6c). The organic matter has completely disappeared and the amount of potassium increases further, unlike the amount of iron that increases slowly. The particles continue darkening.
- **Highly evolved:** The potassium content continues increasing and the previously formed cracks and fissures in the particle are infilled with crystals, which swell the grains. Eventually, a crust of little-evolved glauconitic material is formed around the grain (Lamboy and Odin, 1975), leading to a more spherical particle (Figure 2.6d). The color is now even darker, from dark green to fully black. The texture of the particle is shinier since the particles are polished and they became harder due to the cementation of iron, calcium or phosphate minerals (Tedrow, 2002). This chemical process will stop and the particles will remain stable after burial or after extended exposure at the interface between sediment and water (Hesselbo and Huggett, 2001).

In the sketch from the following Figure 2.7 is illustrated the aforementioned diffusion of potassium from the overlying seawater and iron from reactive detrital minerals, through sediment pore fluids (G. Odin and Dodson, 1982).

The glauconite pellets can range from 0,5 to 0,05mm diameter and as much as 4mm (Tedrow, 2002). Figure 2.13 shows clay-size mica and sand-size particles.



(a) (b) (c) (d)

Figure 2.6: Coprolite (fecal pellet) from the Gulf of Guinea at the nascent stage of glauconitisation: a) entire particle, b) same particle broken showing internal structure with numerous pores.
Glauconite particle from the North West Spanish shelf at: c) evolved stage with cracks being filled up with glauconitic minerals, d) highly evolved stage with crust around the particle. (From Giresse et al. (1980)).

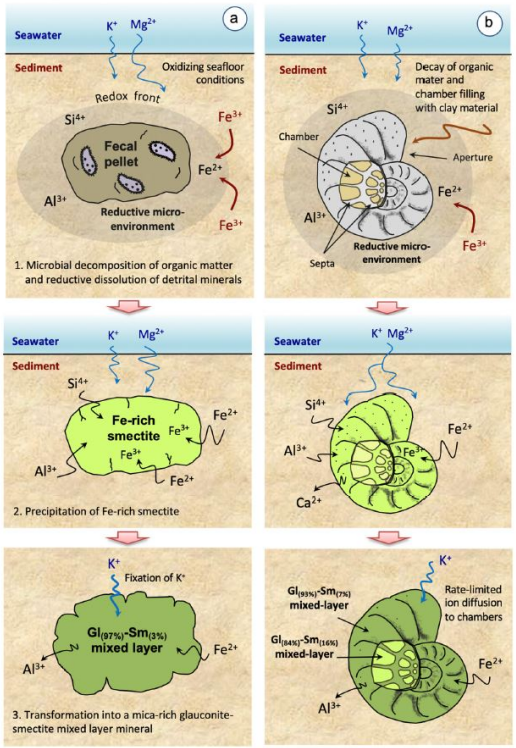
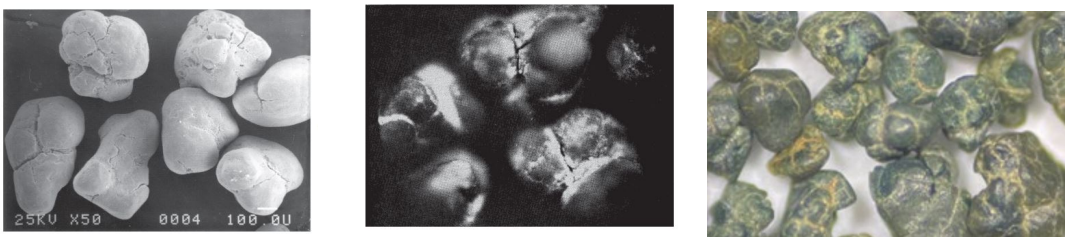


Figure 2.7: Sketch showing the schematic evolutionary process of glauconitisation from fecal pellet substrate (left) and foraminiferal substrate (right). (From Fernández-Landero and Fernández-Caliani, 2021).



(a) (b) (c)

Figure 2.8: Gluconite pellets from the Hornestown formation in New Jersey observed with a) Electron microscope (Photograph by R.Holzer), of size from 0,5 to 0,005mm. b) Microscope, of grain-size. (From Tedrow, 2002); c) Photograph of Poricy Navesink Formation (From DeGroot et al., 2023)

Formation of glauconite occurs in shallow marine environments with low sedimentation rates, semiconfined and suboxic (low oxygen levels) conditions, near the sediment-water interface (G. S. Odin and

Matter, 1981; López-Quirós et al., 2020). Glauconite formation dates back from the end of the Cretaceuos Period (over 65 million years ago) and through the Paleogene Period (25 to 65 million years ago) (Banerjee et al., 2020) (see Figure 2.9). The maximum depth of glauconitisation process depends on the particle size, composition, porosity and permeability of the sediment (G. Odin and Dodson, 1982).

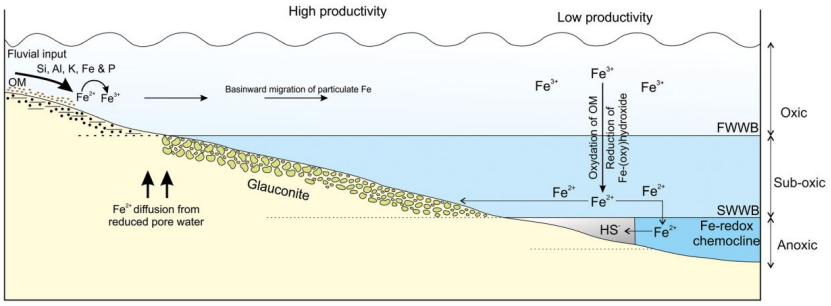


Figure 2.9: Sketch explaining the model of formation of glauconite in shallow marine environment during the Paleogene time. (From Banerjee et al., 2020).

2.3.2. Mechanical properties

The glauconitic sand is classified by many authors as fine to medium sand (Demars, 1982; Joustra and De Gijt, 1982; Westgate, McMullin, and DeGroot, 2022) and poorly graded silty sand (DeGroot et al., 2023). An example of a typical particle size distribution curve from fine to medium glauconitic sand from the vicinity of Antwerp in Belgium is plotted in the following Figure 2.10.

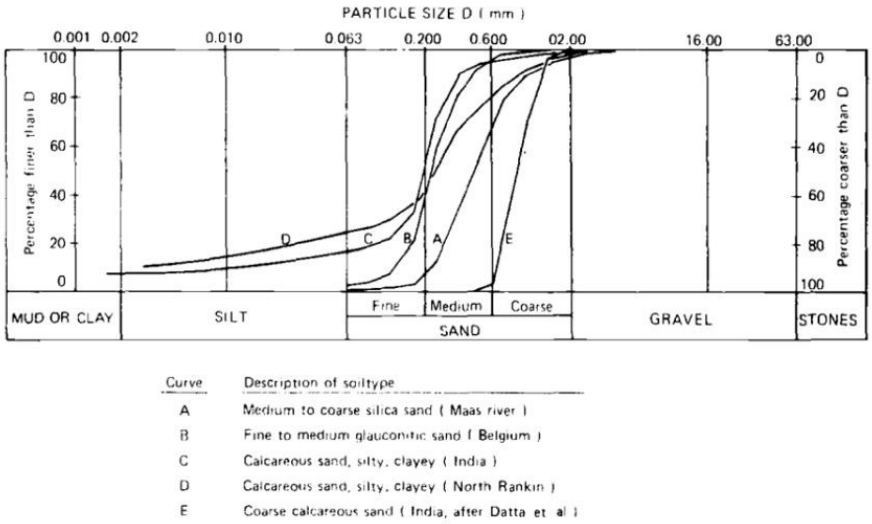


Figure 2.10: Particle size distribution (PSD) curve of glauconitic sand from Belgium (B) compared to calcareous and silica sands (From Demars, 1982)

Glauconite particles will remain stable when buried below the floor surface or when they are not in the boundary between the sediment and the water, since its formation and evolution needs this condition (Hesselbo and Huggett, 2001). Nonetheless, due to its crushability, when low stresses are applied, the sand becomes very brittle and it can even be easily crushed by hand (Long et al., 2019). Moreover, crushing is more significant from shear-induced than from compression (Van Raak, 2009).

Its crushability will depend on glauconite content, particle angularity (Westgate, McMullin, and DeGroot, 2022), uniformity coefficient (uniform distribution of particle strength where all the particles break around a same yield stress) (Di Emidio et al., 2009), grain dimension (Joustra and De Gijt, 1982; Di Emidio et al., 2009), with an increment in breakage susceptibility with an increasing size of grains due

to interparticle stresses, particle strength and more likelihood of the presence of imperfections, e.g. cracks (Di Emidio et al., 2009) and strain rate (decrease of breakage with increasing strain rate) (Di Emidio et al., 2009).

From literature, different laboratory studies have shown the friability or susceptibility of crushing from glauconite. Demars (1982) observed from applying increments of pressure in a high-pressure confining cell, larger volumetric strains at lower confining pressures consistent with the low bulk compression modulus (160MPa) and high crushing coefficient. Similar observations are reported from Joustra and De Gijt (1982) where the plastic deformation due to crushing increased the trend of compression modulus in a pressure cell applying pressure increments reaching 40MPa. Bellotti et al. (1991) investigated the crushability potential of sand from a marine Belgium deposit using an oedometer apparatus and observed crushing initiating at 2MPa (see Figure 2.11 for the results of sieve analyses of glauconite sand subjected to consolidation pressures from 1 to 50MPa). Di Emidio et al. (2009) performed a strain-controlled one-dimensional (CRS) test also to a Belgian glauconitic sand at a strain-rate 1,2%/min reaching 30 MPa in vertical stress to study the effect of the total breakage factor (Bt) of the samples They concluded there was higher breakage in coarser uniform samples rather than in uniform finer and well-graded samples, as well as a decrease of crushability with increasing strain rate. The glauconitic sand exhibited higher crushing than many carbonate sands.

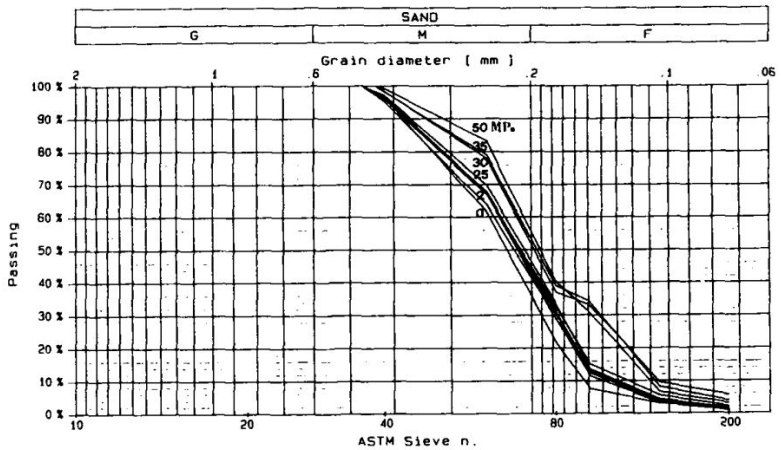


Figure 2.11: Sieve analysis results of glauconitic sand from Belgium deposit after being subjected to consolidation pressures between 1 - 50 MPa. (From Bellotti et al., 1991).

Glauconite's hardness measured on the Mohs scale, is found to range between 2 and 2,3 (Osborne Hutton and Seelye, 1941; Di Emidio et al., 2009; Westgate, McMullin, and DeGroot, 2022). Hardness can be compared to that of gypsum, 2, or calcite, 3; but the difference is clear to the hardness of quartz that is 7. Regarding the specific gravity (G_s), various authors reported a wide range of values from analysed specimens. For instance, the glauconite sand from the Berchem formation in Antwerp, (glauconite content 53%) it is found to be 2,807 (Yoon and Van Impe, 1991), the Thanet Sand from London (glauconite content <10%) is 2,65 (Ventouras and Coop, 2009), from New Zealand between 2,55 and 2,79 (Osborne Hutton and Seelye, 1941). New Jersey glauconite sands from the Hornerstown formation can range from 2,3 to 2,9 (Tedrow, 2002), whereas from the Sewell Hornerstown and Poricy Navesink formations, the specific gravity is 3,01 and 3,04, respectively. These sands contain 95-98% glauconite content (DeGroot et al., 2023). The change in hardness and G_s values is thought to be dependent on composition and the degree of drying (Tedrow, 2002)

.

The particle crushing of the glauconitic sand and hence, the large increments of clay content and plasticity (Westgate, McMullin, Zeppilli, et al., 2022; DeGroot et al., 2023; Westgate, Beemer, et al., 2023; Long et al., 2019; De Nijs et al., 2015; Di Emidio et al., 2009) transform the sand into a fine-grained soil thus showing a change in permeability, and strength, a strong thixotropic behaviour and reduction in shear strength (Westgate, McMullin, Zeppilli, et al., 2022). An example of the decrease in

effective friction angle after drained shear tests is shown in Figure 2.12.

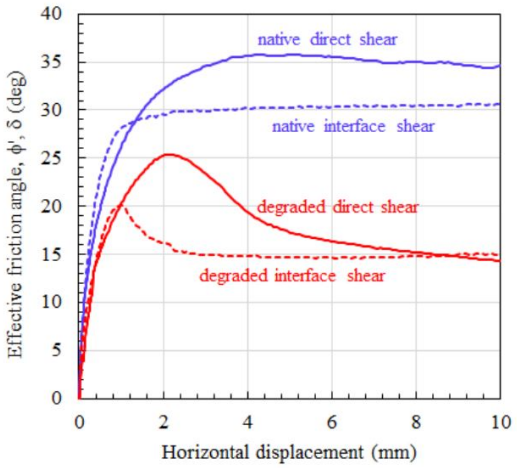


Figure 2.12: Test results after shearing under drained conditions native specimens air pluviated and 1hr mixed moist-tampered, both to 40% relative density under 150kPa normal stress. (From Westgate, McMullin, Zeppilli, et al., 2022).

2.3.3. Geotechnical challenges with glauconite sand

Glauconite sand poses particular geotechnical challenges due to the crushing of glauconite and its transformation into a high plasticity soil, as observed by different authors (De Nijs et al., 2015; Perikleous et al., 2023; Westgate, McMullin, Zeppilli, et al., 2022). Figure 2.13a shows a visual example of the resulting soil after crushing New Jersey glauconite sand (98% content by weight) at an onshore site. The plasticity of the soil can be noticed from the clayey texture.

The crushing process and its following transformation into a clayey soil poses risks to foundation installation due to the change in the soil-structure interaction (Westgate, McMullin, Zeppilli, et al., 2022), as well as influencing the unique response in cone penetration tests (CPT), characterised by high cone tip resistances (q_t) and sleeve friction (f_s), which lead to high friction ratios (R_f), that can range from 3% to more than 10%. (De Beer, 1974; Van Raak, 2009; Van Alboom et al., 2012; Long et al., 2019). If CPTu are performed, variations in excess pore pressures (u_2) are also noticed (see Figure 2.14). All of this can mislead the classification of undisturbed glauconite sand (2.13b) behaviour when using typical CPT-based classification (e.g. Robertson, 2016), as well as creating a significant uncertainty for pile drivability analyses (DeGroot et al., 2023; Perikleous et al., 2023).



(a) (b)

Figure 2.13: a) Crushed glauconite sand during hollow stem augering (From Westgate, Beemer, et al., 2023, courtesy of Rutgers University); b) Glauconitic sand of the Diest Formation (39% glauconite content) intercalated with clay layers (left) and slightly glauconitic sand of the Kasterlee Formation (5% glauconite content) with thin intercalated clay. (From Adriaens et al., 2014)

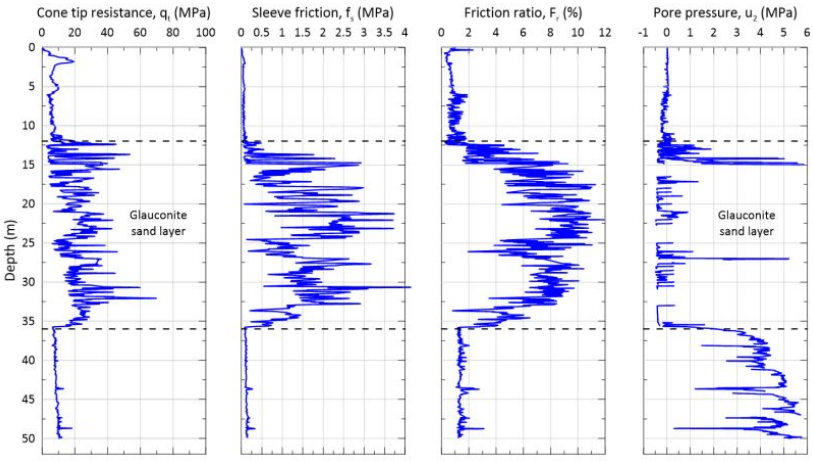


Figure 2.14: Example of a CPT reading in a US North Atlantic OCS glauconite sand. (From DeGroot et al., 2023)

An example for geotechnical challenges is the recent back-analysis of the driving records performed after installation of 94 monopile foundations in the North Sea, which revealed the influence of glauconitic soil minerals showing increased driving resistance of sand layers comprising glauconite contents ranging between 5% and 20%, resulting in an increment of blow counts compared to the predicted for some locations (Figure 2.15). Prior to the back-analysis, the soil layers would have been described as silty sands and consequently modelled as non-cohesive materials for installation analysis (Perikleous et al., 2023). During this analysis, it was concluded that modelling the glauconitic sand as a clay material with the Alm and Hamre (2001) clay method for estimating the soil resistance to driving (SRD) predicted the blow counts closely to the recorded ones.

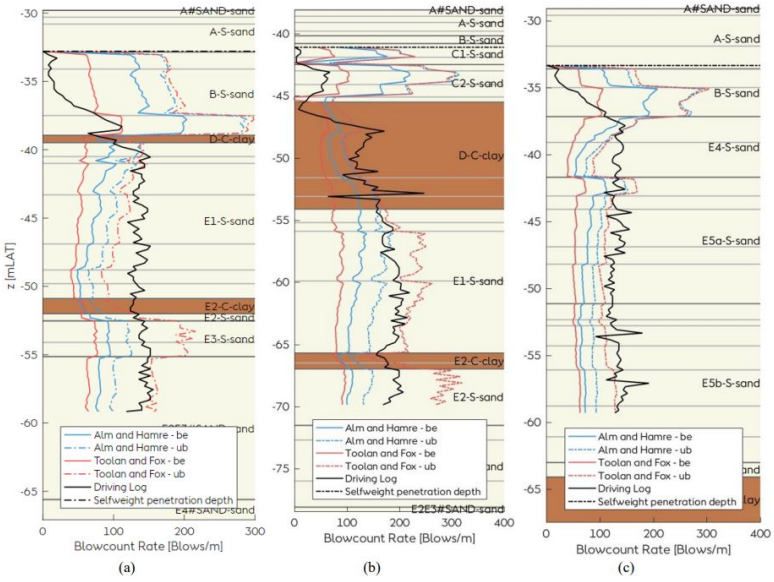


Figure 2.15: Examples of higher recorded blow count curves than the predicted ones due to underprediction of driving resistances with different SRD methods (From Perikleous et al. (2023)).

Previously, De Nijs et al. (2015) also observed higher number of blows required and more time-consuming installation of sheet piles in Antwerp, Belgium, where the glauconite content (by weight) ranged from 35 to 65% (Van Raak, 2009). This was due to the increment of fines and clay content leading to high plasticity clay like behaviour due to particle crushing. The 3cm thick clay plaster adhered to both sides of the retrieved sheet pile was characterised by a fines content 14% higher than the original soil (2.16).

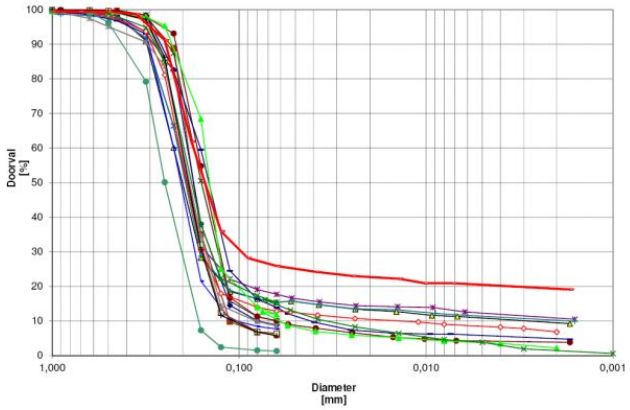


Figure 2.16: Grain size distribution curves on the Berchem formation samples before installations highlighting in red the curve representing the soil sample adhered to the sheet pile walls after retrieval (From De Nijs et al., 2015).

Regarding pile foundations, the crushability of glauconite and the following transformation of soil type, increases the side friction. This, in combination with the high tip resistance at the pile head due to the undisturbed granular soil pose a significant geotechnical challenge and it can lead to early pile driving refusal (Westgate, McMullin, Zeppilli, et al., 2022).

Chapter 3

Thesis statement

3.1. Problem description

During pile driving operations, great stresses are achieved and cyclic loading conditions are applied. Therefore, particles around the pile are crushed as a result of this combination. Nonetheless, because glauconitic sand particles have low strength, they are more prone to crushing under stresses leading to greater crushing during pile installation due to the significant degradation they undergo under these conditions. This process transforms the sand into a low-permeable fine-grained clay-like material leading to a change in soil behaviour from a sandy to a clayey behaviour (Westgate, McMullin, and DeGroot, 2022), which plays a role in the soil-structure interaction. As a consequence, this results in higher pile shaft frictions and high driving resistances than previously expected, due to the formed clay-like barrier created by the crushed particles. This poses significant high risks to pile installation, e.g. premature pile installation refusal (Westgate, McMullin, and DeGroot, 2022).

This research aims to obtain detailed information on the soil response of glauconitic sand in saturated conditions during pile installation with a new sample preparation method for glauconitic sand containing fines. It will investigate the feasibility of cone penetration testing, cyclic loading, pile driving, as well as the analysis of the shear band and grain crushing around the instrumentation penetrated in the soil. With it, a better understanding of the geotechnical properties and the mechanical behaviour of this geomaterial during cone penetration and pile installation will be provided. Therefore, the following research questions will be answered:

(1) How to prepare a large-scale sample for a calibration chamber test with glauconitic sand from a natural deposit in Antwerp, Belgium?
(2) What is the soil response to cone penetration and pile installation in a calibration chamber using the previously prepared sample?

3.2. Hypothesis

For the research questions described above, firstly, it is expected to be able to prepare a dense sample with the non-homogeneous glauconitic sand in order to resemble reality and secondly, observe the transformation from a coarse-grained to a fine-clayey soil as a result of the crushing of glauconite pellets, emphasising in the increase of fines and plasticity around the shaft and the tip of the cone and pile. Moreover, high cone resistance (q_c) and sleeve friction (f_s) are expected to be achieved, as well as higher driving resistance with depth leading to higher blow counts with depth as a result of the high tip resistance of the dense sample and the applied stresses.

3.3. Experimental approach and goal of the experiment

The behavior of the glauconitic sand under axial and cyclic loading can be studied in a lab-scale instrumented calibration chamber (CC) penetrating a cone and driving an instrumented model pile simulating different installation methods (a detailed description of the experimental setup and instrumented pile is found in Chapter 5). Hence, this research aims to perform 3 tests on the sand fraction of large size specimens of glauconitic sand of the Kattendijk formation obtained from a construction project in Antwerp, Belgium. In the following Chapter 4, a detailed description of the material used in the tests is

provided. The samples will be prepared at a stress state $\sigma'_{h0}/\sigma'_{v0}$ = 200/100 [kPa] and the soil will be characterised after testing in order to assess the degraded properties.

The findings of the new sample preparation method and the tests in the calibration chamber are expected to provide a new method for sample preparation for glauconitic sand containing fines and to better understand the geotechnical properties and mechanical behaviour of the sand fraction of the glauconitic sand during cone penetration and pile driving.

3.4. Material: glauconitic sand from the Kattendijk formation

The glauconitic sand used for this research was obtained from the Oosterweel connection project in Antwerp, Belgium. The company involved in this project, Lantis, provided the cut and cover area where the sample could be obtained from. In Figure 3.1 the excavation area is shown highlighting the CPTs (orange) and boreholes (green) available. The geotechnical data from the Flemish subsurface could be accessed through the online platform Databank Ondergrond Vlaanderen Portaal (DOV-Portaal). Among them are cone penetration tests (CPTs) and borehole data.

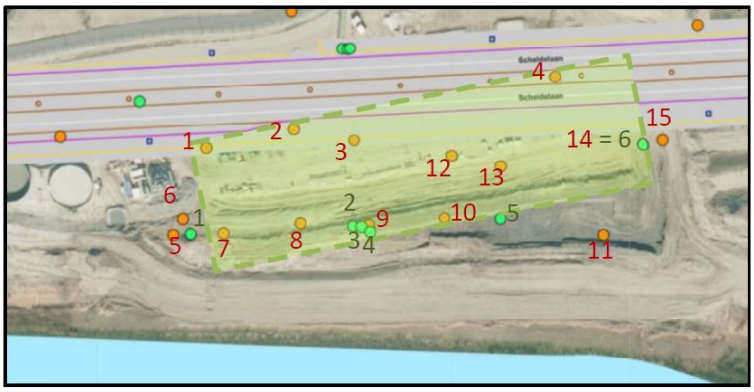


Figure 3.1: Cut and cover area in Antwerp (Brussels).

After analysing all the CPTs and boreholes reports from this area, three main formations could be identified: Kattendijk, Berchem and Boom clay. Due to excavation phases of the construction, the Kattendijk formation was the one used for this research. The high cone resistances (q_t), sleeve frictions (f_s) and friction ratios (R_f) within the sand layers indicated the presence of glauconite in the CPT data at about level -6 mTAW. Therefore, the location found more significant for this research due to the larger presence of glauconite content (about 20-25%) and high cone tip resistance (44MPa) was location 7. In Figure 3.2 the corresponding CPT profile is shown. Appendix A contains the original CPT data obtained from DOV.

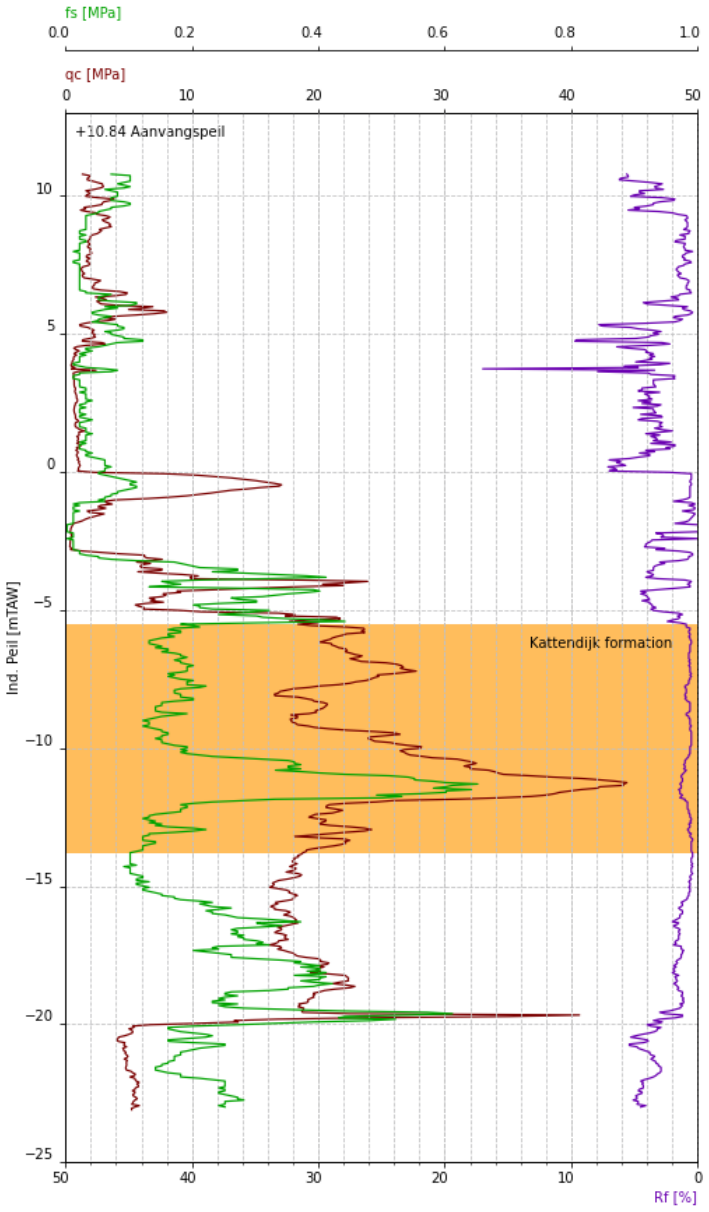


Figure 3.2: Profile CPT 7 (from DOV-Portaal dataset).

Chapter 4

Characterisation of the soil and description of the soil preparation

4.1. General description of test material

The glauconitic sand was obtained from direct excavation from the natural deposit in Antwerp, Belgium, and it belonged to the Kattendijk Formation. This fine-grained to medium-fine grained with clay admixture introduced by De Meuter and Laga (1976) was characterised by the presence of shells and fragments and larger particles, e.g. tiles, boulders, bricks and gravel, as well as fossils and big clumps of organic matter (see Figure 4.1). The latter, were analysed in the microscope showing an intense orange paste indicating high plasticity clumps (Figure 4.2). To avoid the impact of larger particles on friction resistance and crushing characteristics during the performance of the tests, the soil was pre-sieved through a 5mm opening using a mechanical sieving machine. The resulting soil is denoted as *as-received* throughout the report.



(a) (b) (c)

Figure 4.1: a) Carbonates and minerals found in the soil; b) Big clumps of organic matter and conglomerate; c) Big clump separated in half.



(a) (b) (c) (d)

Figure 4.2: Clump taken from the as-received soil showing a high plasticity orange paste indicating iron composition. All photos are the same piece: a) General view of the clump; b) Closer image of the clump; c) Clump rolled; d) Drops of water on top of the splashed roll.

4.1.1. Glauconite pellets

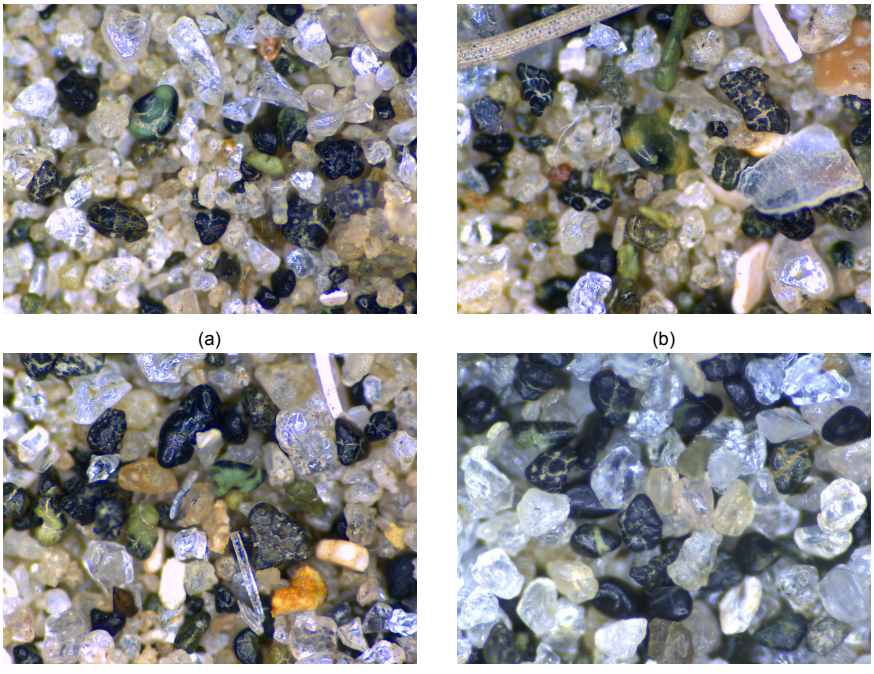
Magnetic separation test results performed by Qmineral indicated 11,1% of averaged glauconite content in the as-received soil. This contained pellets of different maturities, observed by the color of the particles, the smoothness of the surface and the presence of cracks. This can be seen in Figure 4.3, where several photos obtained from the digital microscope Leica DMS300 with a magnification range of 6x are shown: from nascent pellets, greener than the rest, to slightly evolved particles in transition of chemical composition, and therefore, becoming darker but still being greenish, to evolved deformed pellets with cracks and infilled crystals, to a highly evolved glauconite black pellet with a smooth and shiny surface. According to the results obtained from the X-Ray Diffraction analysis performed by Qmineral (Table 4.1), the major component of the glauconitic sand was quartz (largest mineralogical composition (SiO_2)), followed by glauconite with the following molecular structure:

$$(K, Na)(Fe^{3+}, Al, Mg)_2(Si, Al)_4O_{10}(OH)_2$$

According to the chemical composition results and considering the potassium oxide concentration (K_2O) the only reliable chemical indicator of glauconite maturity (Huggett, 2013), the majority of the glauconite pellets were in the initial phase of maturity: nascent.

Element	Al_2O_3	K_2O	Fe_2O_3	SiO_2	MnO	MgO	CaO	Na_2O	TiO_2	P_2O_5
[%]	3,59	1,75	4,7	79,96	0,015	0,68	3,1	0,32	0,38	0,08

Table 4.1: Chemical composition of the samples determined by XRF analysis performed by Qmineral.



(a) (b) (c) (d)

Figure 4.3: Different images captured with the digital microscope using magnification range of 6x showing mineralogy of the glauconitic sand, e.g. quartz (transparent particles), glauconite pellets (green and black), among others. It should be highlighted the presence of fragments of fossils and carbonates.

Some glauconite particles were carefully separated and measured using the digital microscope (see Figure 4.4). It should be highlighted that the particles might have been disturbed upon excavation and following transportation, in addition to being crushed before this process (as stated in the description of the boreholes of the zone). The size of the glauconite particles ranged between 400μm and 190μm, sometimes finding larger particles of 500μm, but not smaller than 150μm, unless crushed or occurring in clay-sized fractions (Adriaens et al., 2014). Visual identification of these particles was possible with

the naked eye due to their size, although challenging due to the amount of other minerals. However, when the soil was wet, they were attached to the fingers and observed with the naked eye (Figure 4.5).

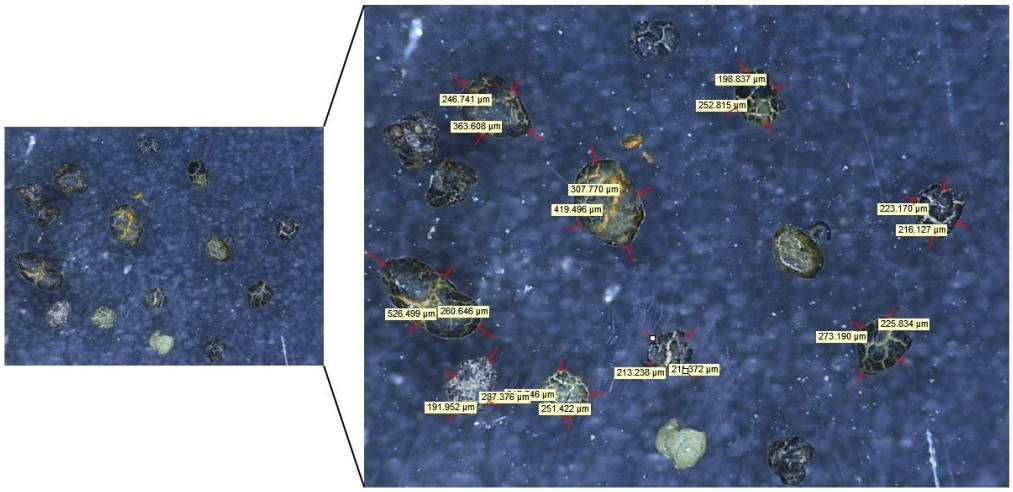
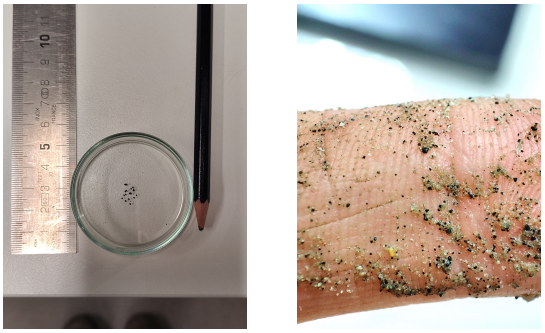


Figure 4.4: Measurements of glauconite particles using digital microscope with magnification range of 6x. The average size particle is 270μm.



(a) (b)

Figure 4.5: Glauconite pellets a) in the Petri dish and b) on the finger (in black and green and among other minerals).

4.1.2. Geotechnical characterisation: as-received soil

- **Particle size distribution (PSD)**

  The grain-size analyses of the as-received soil were performed using two different methods: (1) laser diffraction using the particle size analyser Malvern Mastersizer 3000 and (2) traditional manual method according to ASTM D422 (ASTM, 2007). A detailed description on the procedures and specifications are presented in Appendix B.1.

  Figure 4.6 presents the obtained PSD curves from the as-received soil combining the results of both methods (Malvern results are marked in the legend with an *M.*). Differences are observed using different methods, mainly in the measurement of fines. The grading curves using the Malvern equipment indicate that approximately 90% of the particles are coarser than 50μm, whereas using the traditional method, this value is more than double. However, this difference relies on the lack of accuracy in the determination of the fines that keep retained in the sieves and attached to the particles, and the coarser clumps created after oven-drying the material, acting as coarser particles even though they are clumps that can be broken with the fingers, but not in the shaker. This indicates a better quantification of fines using the Malvern equipment. The difference in the curves using this equipment relies on the small amount of soil that is needed for performing the analysis, and therefore, in the

heterogeneity of the sample being tested.

According to the uniformity coefficient (C_u) (equation 4.2) values obtained from the particle size values, the as-received soil can be classified as well graded for the traditional method (since C_u > 4 to 6) but poorly graded for the Malvern method. On the other hand, according to the coefficient of curvature (C_c) (equation 4.1) the as-received soil is classified as well graded, since 1 < C_c < 3. The results are summarised in Table 4.2, where the values corresponding to the same method are obtained by averaging the results.

$$C_c = \frac{(D_{30})^2}{D_{60} \times D_{10}} \tag{4.1}$$

$$C_u = \frac{D_{60}}{D_{10}} \tag{4.2}$$

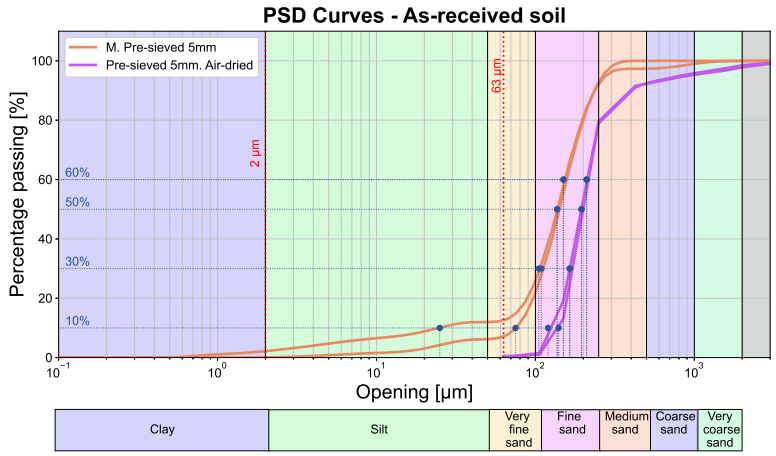


Figure 4.6: PSD curves from as-received soil.

	D_{60} [μm]	D_{50} [μm]	D_{30} [μm]	D_{10} [μm]	C_u [μm]	Cc [μm]
Malvern 3000	160	137	107	50	3,20	1,43
ASTM D422	210	195	164	130	7	0,985

Table 4.2: Summary of particle sizes for as-received glauconitic sand

Eventually, the as-received soil can be classified as silty sand with 2% clay content, 10% silt and 88% sand, according to the Unified Soil Classification System (USCS). In addition to this, in order to understand better the fines composition of the soil, only the fine fraction from the sample marked in green in Figure 4.6 was analysed with the Malvern equipment. This shown that the fines mainly consist of silt: 23% clay, 72% silt and 5% sand.

- **Specific gravity, G_s**

  To measure the specific gravity (G_s) of the glauconitic sand, the Gas Pycnometer type Ultrapyc 5000 was used in the Geoscience and Engineering Laboratory at TUDelft. The advantages of performing the measurement in this pycnometer were that very accurate results were obtained in a small amount of time, since each test provided an average value from a 5 times iteration process. A detailed description of the procedure, the samples tested and the results are presented in Appendix B.2. The obtained specific gravity (G_s) value for the as-received soil was 2,728 g/cm^3.

- **Minimum and maximum density and unit weight**

  The minimum and maximum density soil parameters were obtained in accordance with standards ASTM D4254-16 (ASTM, 2016b) and ASTM D4253-16e1 (ASTM, 2016a), following the dry method. However, small variations with the used apparatus were made. A detailed description of the procedure and calculations are presented in Appendix B.3. The minimum and maximum density ($\rho_{d,min}$, $\rho_{d,max}$) values measured were, respectively, 1,06 and 1,33 g/cm^3.

4.2. Soil preparation: removal of fines

As seen, the glauconitic sand collected from Antwerp was not homogeneous and contained approximately >15% of fines. This caused the soil structure to be mainly dominated by the finer particles and it made very difficult the sample preparation and the obtention of high densities and compaction. Although there are well established methods for preparation of clean sands and cohesionless soils such as silica sands, these approaches could not be directly used in case of the glauconitic sand. Therefore, before preparing the full-scale samples in the calibration chamber, a familiarisation phase was started with the as-received material with the objective to assess the applicability of the available preparation methods used for silica sand in relation to glauconitic sand specimens.

After a study on literature review based on sample preparation techniques for sand and silty sand specimens and many attempts on preparing smaller scale samples, it was decided to perform the tests in an idealised material which enabled the preparation of repeatable and homogeneous dense samples in fully saturated conditions. A paper including the aforementioned literature review, practical information and limitations of the preparation of large-scale samples with glauconitic sands is to be published. This soil consisted on the sand fraction of the as-received soil after the removal of fines, since it was previously analysed that the glauconite granules were part of the coarser fraction of the soil. The process is explained in the following subsection 4.2.1 and it was considered a good compromise to create the glauconitic samples in the calibration chamber for the purpose of the research.

4.2.1. Description of the process

After the familiarisation phase, it was decided to adopt an idealised material consisting of a reduced particles size distribution ranging between 63μm and 5mm. With this, a better evaluation of the crushing phenomenon during the experiments and a reduction of sample preparation uncertainties due to the presence of fine particles were aimed. This procedure consisted in the removal of fines by means of washing them out with water (see setup in Figure 4.7), since it had to be a cautious process in order to avoid the occurrence of the crushing phenomenon of the glauconite granules before the tests. The steps followed are showed in Figure 4.8 and they were as follows:

(a) Fill approximately half of the cylinder with as-received glauconitic sand.

(b) Fill the cylinder containing sand with pressured water to the top, so that the soil was properly mixed and remove the formed foam.

(c) Allow segregation to occur, waiting approximately 5 minutes. Check with a beaker the fines remaining floating in the water and repeat steps a-c until almost no fines are observed (approximately 5-8 times).

(d) - (e) Pump the water out containing fines that did not sink and lift the cylinder up in order to flush the soil out into a drained bag.

(f) Lift the bag some days before the sample preparation in order to avoid fully saturated soil and be able to quantify moisture content.

A visual comparison of the change in texture between the soil as-received and the sand fraction resulting after the removal of fines is showed in Figure 4.9.

This process had a similar equivalency to performing wet sieving using a 63 μm opening sieve, since it was proofed by passing the pumped water through this mesh. It could also be checked that the

glauconite particles were retained in the sieve and therefore, they remained in the sand fraction of the soil. Magnetic separation test results performed by Qmineral indicated 13,2% of averaged glauconite content in the resulting sand fraction of the soil after washing out the fines.



Figure 4.7: Setup for removing the fines.

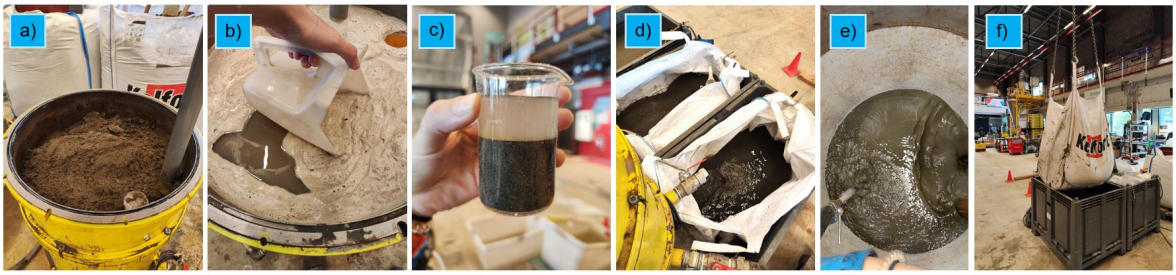


Figure 4.8: Soil preparation process based on the removal of fines. Description of the steps described above.



(a)



(b)

Figure 4.9: Visual comparison between (a) the soil as-received and (b) the soil after removal of fines used for sample preparation. These are frames from a video in which the soil is poured and mixed during 30 seconds in water.

4.2.2. Geotechnical characterisation: sand fraction

- **Particle Size Distribution (PSD): sand fraction**

  The grain-size analyses of the sand fraction were performed using the aforementioned methods for the as-received soil, namely (1) Malvern Mastersizer 3000 and (2) traditional method following standard ASTM D422 ASTM (2007). In this case, the soil used was oven-dried to 110ºC, since there were no small clumps created by fines that were acting as coarser particles. The resulting PSD curves are shown in the following Figure 4.10, in comparison with the as-received soil PSD curves. Importance

should be given to the decrease in fines contents comparing the Malvern curves and an increase in medium sand fraction using the traditional method. The increase in verticality of the curve, indicating a uniformly graded soil, should also be highlighted. According to the uniformity coefficient (C_u) and coefficient of curvature (C_c), this steep curve indicates a poor graded soil (uniformly graded and homogeneous) since C_u <4 and 1 < C_c < 3 (see Table 4.3).

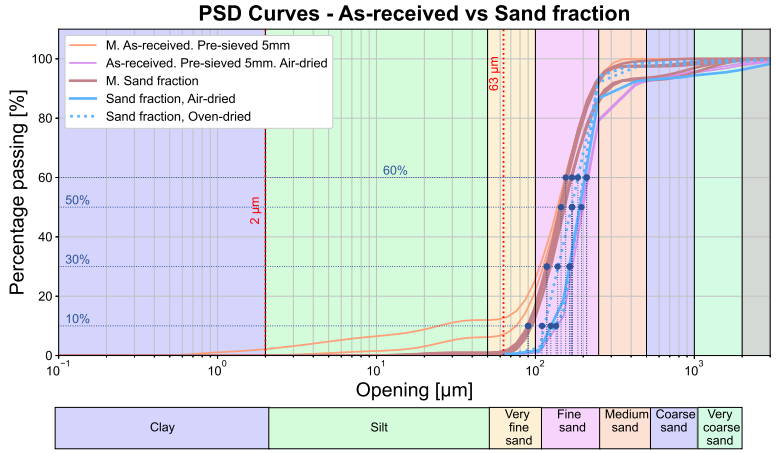


Figure 4.10: PSD curves comparing the soil before and after removal of fines.

	D_{60} [μm]	D_{50} [μm]	D_{30} [μm]	D_{10} [μm]	C_u [μm]	Cc [μm]
Malvern 3000	162,5	145	118	90	0,95	1,81
ASTM D422	197,5	183,5	155	123	0,99	1,61

Table 4.3: Summary of particle sizes for sand fraction of glauconitic sand after washing out the fines.

- **Specific gravity, G_s**

  The specific gravity (G_s) of the sand fraction resulting from the removal of fines was also determined using the Gas Pycnometer type Ultrapyc 5000. A detailed description of the procedure, the samples tested and the results are presented in Appendix B.2. The obtained specific gravity (G_s) value for the sand fraction of the glauconitic sand was 2,667 g/cm^3.

- **Minimum and maximum density and unit weight**

  The minimum and maximum density soil parameters were obtained in accordance with standards ASTM D4254-16 (ASTM, 2016b) and ASTM D4253-16e1 (ASTM, 2016a). For this soil, dry and wet methods were followed. However, the wet method results were considered more representative regarding the similarity to the future sample preparation. A detailed description of the procedure and calculations are presented in Appendix B.3. The minimum and maximum density ($\rho_{d,min}$, $\rho_{d,max}$) values measured were, respectively, 1,48 and 1,66 g/cm^3.

4.2.3. Discussion

Regarding the grain-size analyses, as observed from the measurements obtained, differences were found in the determination of particle size using the two different methods, indicating a better quantification of fines using the Malvern equipment. Although, both methods did not rely on similar techniques and the results should not be compared directly to each other, a clear reduction of fines was observed in the PSD curves after washing out the fines.

With reference to the geotechnical parameters, differences were noticed after the removal of fines of the as-received soil, leading to a lower value for G_s, and to larger values for $\rho_{d,min}$ and $\rho_{d,max}$. In relation to the G_s, while the as-received values were similar to the Belgian sand (Berchem formation)

and New Jersey sand, with G_s = 2,8 (Westgate, McMullin, Zeppilli, et al., 2022) and the sand fraction after removal of fines, like the London sand, with G_s = 2,65 (Westgate, McMullin, Zeppilli, et al., 2022), the values for both types of soil were in the ranges between 2,5 and 3,0 as observed from G. S. Odin and Matter, 1981, Tedrow, 2002, Van Alboom et al., 2012. With respect to the $\rho_{d,min}$ and $\rho_{d,max}$, as observed from the results, the wet method lead to higher density results (and lower porosity and void ratio) than using the dry method. Therefore, these results would introduce significant uncertainties and affect in later calculations of the relative density of the samples obtained after excavation of the soil. Because of this reason, and because of a resemblance between the sample preparation and the performance of the wet method in the determination of $\rho_{d,min}$ and $\rho_{d,max}$, the wet method results were used for further calculations. These were in range of the values obtained for the Poricy Navesink glauconite sand from New Jersey, with a $\rho_{d,min}$ and $\rho_{d,max}$ of 1,37 g/cm^3 and 1,64 g/cm^3, respectively (Westgate, Beemer, et al., 2023).

The following Table 4.4 summarises the geotechnical parameters used for further calculations, and belong to the soil used for preparing the samples: the sand fraction of the glauconitic soil after removal of fines.

Parameter		**Value**
Maximum dry density ($\rho_{d,max}$)	[g/cm^3]	1,66
Minimum dry density ($\rho_{d,min}$)	[g/cm^3]	1,48
Maximum unit weight ($\gamma_{d,max}$)	[kN/m^3]	16,24
Minimum unit weight ($\gamma_{d,min}$)	[kN/m^3]	14,55
Maximum porosity (n_{max})	[-]	0,44
Minimum porosity (n_{min})	[-]	0,38
Maximum void ratio (e_{max})	[-]	0,80
Minimum void ratio (e_{min})	[-]	0,61
Specific gravity (G_s)	[g/cm^3]	2,667

Table 4.4: Summary of the geotechnical parameters of the sand fraction of the glauconitic soil after removal of fines used for preparing the samples in the calibration chamber.

Chapter 5
Chamber test

5.1. Experimental setup

In order to perform the tests, the calibration chamber (CC) setup used was designed and constructed by Deltares and used for the PhD study of Dirk de Lange (not yet published). The CC consisted of six cylindrical stackable steel rings of 895mm inner diameter and 240mm height with rubber o-rings in between of the cells to act as sealing. Two different actuators were used to drive the cone and the 510mm closed-ended instrumented pile into the soil, using jacking and impact installation methods. The former used a hydraulic actuator to continuously push the pile and the latter a manual driving system comprised of a hammer, a 4kg weight, and a 12kg tube to guide the weight. (See section 5.5 for all specifications of driving methods.)

The chamber was filled with two different materials in two layers: the lowest is 460mm height of Baskarp B15 sand and on top, 500mm of glauconitic sand. In total, 960mm height of soil was used and a close-ended instrumented pile was penetrated using different installation methods.

Starting from the bottom of the setup, at Ring 0, three load cells were installed to measure the force applied on top of them by the soil of the sample located between Ring 1 and Ring 4. Moreover, this ring included a valve to allow drainage through the bottom of the soil sample where a geotextile, a porous filter and a filter plate were placed. (See Appendix C.1 for more details on the installation of the bottom ring.)

The setup was comprised between Ring 1 and Ring 4 with a flexible rubber membrane 3mm thick and stiffness 1200kPa and a foam 25mm thick through which air could enter to apply a constant radial pressure, eliminate friction along the wall and achieve a flexible boundary condition. (See Appendix C.3 for more details on the installation of Rings 1 to 4.)

In order to fix the membrane in place when the stresses were applied, a ring with long bolts was placed on top of the membrane. Moreover, to apply the vertical pressure to the soil sample, a steel plate with five hydraulic jacks that displaced vertically and the pressure distributor that distributes an equal pressure to the jacks was placed on top of the glauconitic sand. The contact between the soil and the plate was ensured by three layers of thin foam that were placed in between. The central 35mm hole in the top plate allowed for drainage and soil penetration of the pile or cone. With an extra plate above, the ring and the top plate applied the reaction force to the membrane and the soil, respectively. This plate was used for guidance of the three potentiometric displacement sensors that measured the displacement of the top plate.(See Appendix C.4 for more details on the top configuration).

The setup also included a configuration with three miniature pore pressure transducers (PPTs) of 6,4mm diameter, facing the cone/pile shaft, loaded at different depths within the specimen to assess the potential development of pore pressures along the shaft and tip of the pile (see Figure 5.1 and Table 5.1). The heights of the sensors were chosen assuming the pile reached the target penetration of 400mm below the soil in each test. In addition to this, the distance from the tip of the pile and the top of the Baskarp B15 soil was tried to be kept 3D, D being the diameter of the pile (25mm) (based on Hölscher et al. (2012) and Ciantia et al. (2019)). The sensors were type EPB-PW-7bs-Zo/PC0.5/L5M with pressure

range of 7bar.

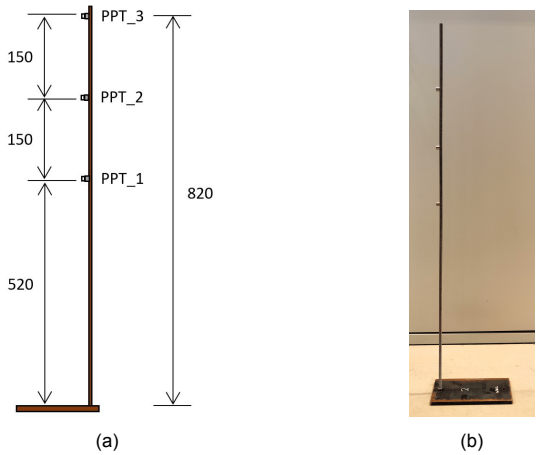


Figure 5.1: PPTs configuration: a) Drawing (dimensions in millimetres) and b) Used in the tests.

Name sensor	Works	Distance from the top of the sample [mm]
PPT_1	Yes	450
PPT_2	Yes	300
PPT_3	Yes	150

Table 5.1: Overview of the PPTs and their location in the setup with an indication if the sensor is working.

The following drawing in Figure 5.2 shows the geometry of the calibration chamber and the final setup.

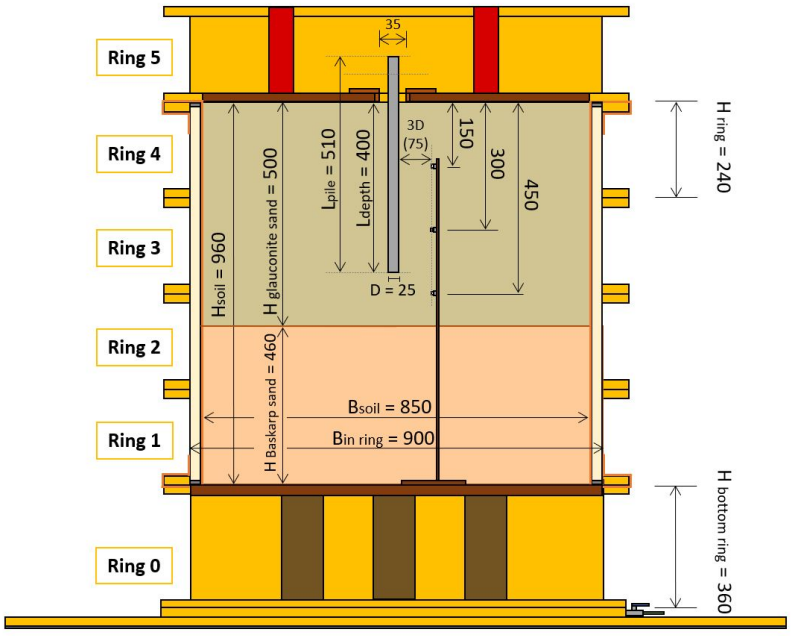


Figure 5.2: Drawing of the calibration chamber and PPTs (measurements in millimetres). Soil sample resting on top of the load cells, between Ring 1 and Ring 4.

5.2. Cone

The cone used for performing the CPTu tests had a diameter of 16mm and a cross sectional area of 2cm^2. It was equipped with a pore pressure transducer 17,9mm above the cone tip, from which excess

pore pressures (u_2) were measured during sounding. Besides, the friction sleeve was 59,7mm long, indicating an offset between the cone tip and the centre of the friction sleeve of 29,85mm. Details of the sensors and dimensions can be seen in the drawing from the cone in Appendix D.

The cone was aimed to be penetrated with the hydraulic plunger up to 400mm below top surface at a controlled rate of 10mm/s.

5.3. Instrumented pile

The model pile was designed and constructed by Deltares and used for the PhD study of Dirk de Lange (not yet published). This instrumented pile was the hollow close-ended pile that penetrated the chamber filled with the geomaterial. It was made with aluminium the walls of which were 3mm thick. The pile had a flat squared base 25mm wide and it was 510mm long, from which 400mm were aimed to be penetrated into the soil.

The pile was instrumented with 6 miniature 3 MPa total pressure transducers (earth pressure sensors) type Kyowa PS-30KC M2 located close to the base at different heights above the pile tip. They were 2mm thick and 6mm diameter, placed in circular grooves of 8mm diameter at opposite sides of the instrumented pile: 3 sensors were located at the side North and 3 at the side South (see Figure 5.4). In order for the cables of the sensors not to move, the instrumented pile was filled with a low viscosity gel type Magic Gel 300. This prevented the cables to be harmed from the impacts and accelerations when performing impact driving.

Table 5.2 summarises this information, in addition to showing the capability of the sensors to perform measurements.

Side of the pile	Name sensor	Works	Distance from the pile tip, h [mm]	Depth [mm]	h/D
North	E1	Yes	90	420	3,6
	E2	No	45	465	1,8
	E3	Yes	15	495	0,6
South	E4	Yes	90	420	3,6
	E5	No	45	465	1,8
	E6	Yes	15	495	0,6

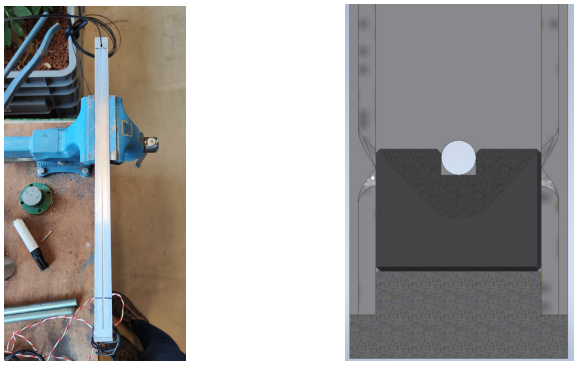
Table 5.2: Overview of the sensors and their location in the instrumented pile in terms of distance from the pile tip (h) normalised by the pile width (D) and an indication if the sensor is working.

The instrumented pile also had a groove in all its four sides in order to glue the 300Hz fibre optic cable (see Figure 5.3a). In this case, only East and West sides were used. The Optical Distributed Sensor Interrogator (ODiSI-B) measured the strains continuously along the length of the fibre optic cable at each millimetre of the pile length, starting 50mm from the top of the pile to leave freedom for the cable to move since it was not driven entirely. Unfortunately, when the instrumented pile was driven using the impact driving method, the cable was not capable of producing any measurements since the frequency was too low due to the short duration of each blow. In this research, the recordings from the fibre optic will not be analysed.

In order to have continuous measurements and not harm the cable at the base of the pile during installation, this crossed through the pile via a 3D printed piece located inside (see Figure 5.3b).

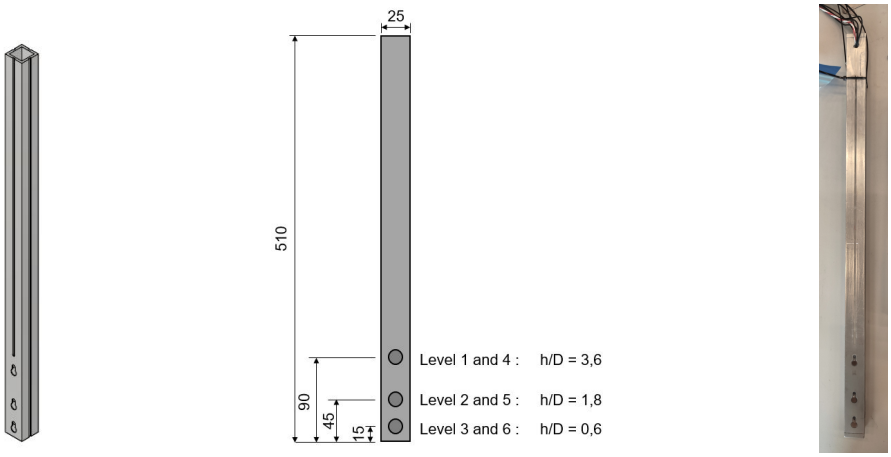
The instrumented pile was also provided with a 30mm long temperature sensor type RS PRO PT100 RTD inside of the pile for measuring the temperature during the driving processes to correct for thermal effects. The plastic patch around the sensor was, however, removed in order to obtain a quicker response to changes in temperature. Its maximum operating temperature is 150ºC.

The next Figure 5.4 shows (a) a drawing of the instrumented pile with the grooves for the sensors and the fibre-optic cable and (b) a schematic view of the instrumented pile indicating the main dimensions and the levels at which the sensors were located with respect to the pile tip as a function of h/D.



(a) (b)

Figure 5.3: a) Groove in the instrumented pile to glue the fibre-optic; b) 3D printed piece for crossing the fibre-optic cable through the pile.



(a) (b) (c)

Figure 5.4: a) Drawing of the instrumented pile. b) Schematic side view of the instrumented pile indicating main dimensions and location of the sensors (dimensions in millimetres). c) Instrumented pile.

5.4. Test procedure

The test procedure followed in this research was copied from the PhD study of Dirk de Lange (to be published) to enable comparison between clean silica sand and glauconitic sand, in the future. The procedure consists on sample preparation, test program, soil excavation and sampling after testing.

5.4.1. Sample preparation

The homogeneous sand layers were prepared mixing the techniques from Mulilis et al. (1975), Mitchell J.K et al. (1976), Poel and Schenkeveld (1998) and Rietdijk et al. (2010), in which the sand (dried or moist) was constantly pluviated with a scoop into the partially filled chamber with de-aired water, while the material was simultaneously being tampered with a flat cylindrical plate so that the air inclusions were reduced and a denser specimen could be achieved. With this method, a fully saturated soil model was achieved.

It was chosen to fill the bottom of the chamber with dry Baskarp B15 sand in order to avoid filling it only with glauconitic sand due to the laborious and physically demanding process of removal of fine particles (see subsection 4.2.1). Therefore, the preparation of 460mm height of dry Baskarp B15 sand with a water depth of 300mm was first. The soil depth was 4D (being *D* the diameter of the pile) below the expected tip of the cone or pile after the installations which was considered far enough for not affecting the stresses around it. After preparing this layer, the water table was lowered 250mm approximately below the surface level of the sand in order to flatten the surface with a ruler (see Figure 5.6a). This

step was possible due to the capillary action of the suction forces acting on the sand providing it with additional strength and ensuring its saturation.

Afterwards, the moist glauconitic sand layer was prepared on top of the Baskarp B15 sand following the same sample preparation. Since the glauconitic sand was humid (see section 4.2.1), the scoops with soil were submerged under the water in order to break the soil clumps. Moreover, the column of water was higher, approximately 400mm above the Baskarp B15 sand surface, so that there was a large distance for the clumps to separate (Figure 5.5).The top surface of the glauconitic sand was flattened with a guide, as shown in Figure 5.6b together with the ending result.

In addition to this, the glauconitic layer included two pink sand layers so that the deformation of the soil could be observed after excavation. This sand layer was poured and tampered too. However, the following first scoops of glauconitic soil poured above this interface were not tampered in order to avoid mixing two different soils. Tampering started again when the pink layer was not visible from the top and an expected 10-20mm thick layer of glauconitic sand was sedimented above it.



(a) (b)

Figure 5.5: Process of sample preparation of a) Baskarp B15 sand and b) Glauconitic sand (in this case pouring it above the water column to show the clumps due to moist content).



(a) (b) (c)

Figure 5.6: a) Process of flattening surface Baskarp B15 sand with ruler. b) Process of flattening surface glauconitic sand. c) Resulting flattened surface at the membrane level.

Since the glauconitic sand used for preparing the samples was moist, the water content was measured by taking samples of the soil being used at different depths, using equation 5.1. The water content results are plotted in the next Figure 5.7, where it can be observed that as the sample preparation evolves and the depth at which the sample is prepared decreases, the soil is more humid, since higher water content was observed for soil taken deeper from the container containing the soil. In Test 3, however, soil undisturbed from the previous tests was used for the top 220mm, which was in a different container

with different water content.

$$w = \frac{M_2 - M_3}{M_3 - M_1} \times 100 \tag{5.1}$$

Being:			
	w	Water content of the soil sample	[%]
	M_1	Mass of the bowl	[g]
	M_2	Mass of the bowl and humid soil	[g]
	M_3	Mass of bowl and dry soil	[g]

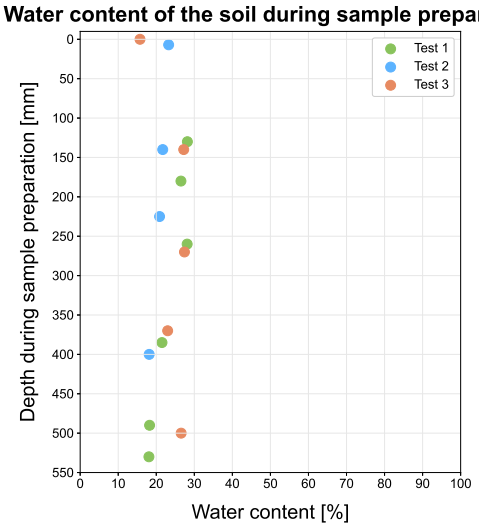


Figure 5.7: Water content of the soil poured in the sample preparation at specific depths below surface level.

The preparation of Baskarp B15 sand was only needed for Test 1. For Tests 2 and 3, only the excavated glauconitic sand was prepared again, leaving the intact Baskarp B15 sand in place (and few centimeters of the intact glauconite (Test 2) in place. Table 5.3 summarises the amount of soil used per test in addition to the average water content of the soil added for the glauconitic sand, height, volume and bulk density. The latter was monitored during sample preparation by measuring the sample height and chamber's diameter and the mass of soil added (see equation B.5). The bulk density indicated in the table concerns the dry mass only. For the Baskarp B15 sand the bulk density calculations were more accurate than the ones for the glauconitic sand due to difference in moist content and, therefore, the bulk density can be representative for the local density. This is not the case for the glauconitic sand, where local density measurements were performed after each test.

$$\rho_t = \frac{M_s}{V_s} \tag{5.2}$$

Being:			
	ρ_t	Bulk density of the soil sample	$[g/cm^3]$
	M_s	Mass of the soil used	[g]
	V_c	Volume of the soil used	$[cm^3]$

		Baskarp B15 sand	Glauconite sand Test 1	Glauconite sand Test 2	Glauconite sand Test 3
Moist mass added	**[g]**	-	635.467,6	565.655,60	612.528,4
Average moist content	**[%]**	-	24,2	20,3	24
Dry mass added	**[g]**	462.794,2	511.569,4	470.455,6	494.923,3
Height of the sample	**[mm]**	460	500	480	500
Volume	**[cm^3]**	261.027,1	283.725,1	272.376,1	283.725,1
Bulk density	**[g/cm^3]**	1,773	1,803	1,727	1,744

Table 5.3: Summary of sample preparation.

5.4.2. Pressurizing and consolidating the sample

In order to reach the desired stress levels up to 200kPa (vertically) and 100kPa (radially), the stresses from the membrane and the jacks were increased slowly in order to avoid any disturbance in the soil porosity and density. Once the objective levels were achieved, there was a consolidation time of 1h minimum between the end of pressurizing phase and the beginning of the test.

After the sample pressurization and consolidation time, the membrane pressure was no longer maintained constantly vacuumed for Tests 2 and 3 (see following section 5.5) and therefore, the lateral stresses were not controlled during the tests in order to observe the installation effect on the horizontal stresses. In Appendixes G, H and I, the membrane pressure recordings are plotted in time.

The pressurizing and consolidation phases for each test can be seen in the plots in Appendix G, H and I.

5.5. Testing program

Different tests were conducted with the objective to evaluate and validate the sample preparation technique chosen for the sand and its workability for future tests in the calibration chamber by testing in 3 different scenarios, namely, CPTu test (static and cyclic), impact driving and jacking installation methods with the instrumented pile, analysing also their results. The imposed initial stress conditions were kept the same for all the tests: σ_v = 200kPa and σ_h = 100kPa. These values were chosen accordingly in order to achieve soil resistances similar to the in-situ conditions.

The testing program was copied from the PhD study of Dirk de Lange (not yet published) to enable comparison between clean silica sand and glauconitic sand, in the future. This included the same stress levels, penetration rates, impact driving and load tests. For the aim of the research, the program followed is the one shown in Table 5.4 below.

Test id	Installation method	Stress state $\sigma'_{v0}/\sigma'_{h0}$ [-]	Penetration rate [mm/s]	Frequency [Hz]
1	Static CPTu	200/100	10	-
1.1	Cyclic CPTu		-	0,1
1.2	Cyclic CPTu		-	1
2	Impact driving		-	0,5
3.1	Jacking		10	-
3.2	Static CPTu		10	-

Table 5.4: Testing program matrix.

There were several reasons why the tests were performed in this particular order. The static CPTu was performed first, at a constant penetration speed of 10mm/s, faster than the standard 20mm/s, in order to characterise the soil sample, verify its homogeneity and continuity and, eventually, check the achieved resistance in the soil so that it could be continued in the same direction with the following tests. At the end of this test, two cyclic CPTu tests were performed at 0,1Hz and 1Hz with an ampli-

tude of 10mm. Afterwards, impact driving method was chosen since it was a less aggressive method for the instrumented pile. The jacking method was the last test performed because of the high risk of pile breakage due to bending, which ended happening. That is the reason why there was a Test 3.2 performed, where a CPTu was penetrated at a constant penetration speed of 10mm/s next to the instrumented pile. The measurements of this last CPTu are not included in this report, since it was just performed due to the availability of a larger space in the top plate and the boundary conditions were different compared to the rest of tests. The installation phases of Tests 2 and 3 were performed in different steps, since they also included 2 load tests in between.

5.5.1. Initial conditions

In order to keep the sample saturated, the water level was always a few centimeters above the soil surface, because the pressurizing phase was always drained. The head was remained constant by means of a connected hose at the same height.

The height of the water measured at the center of the hose (a), the height of the water inside the chamber at the start of the test (b), the diameter of the hole of the top plate (c) and the soil height (H_{soil}) are indicated in the following Figure 5.8 and summarised in Table 5.5. The hole of the top plate was larger in Test 3 since a piece was removed to bolt a guide to ensure the verticality of the pile, leading to a different boundary condition on the top.

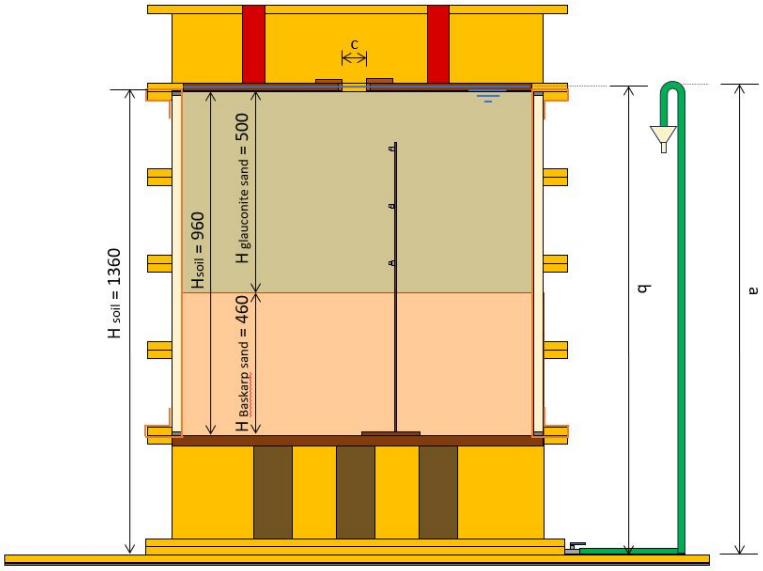


Figure 5.8: Chamber drawing indicating measurements a, b, c and H_{soil} from the bottom of the setup (6cm above the floor) and thicknesses of the soil layers. (Measurements in millimetres).

Test	a [mm]	b [mm]	c [mm]
1	1385	1390	35
2	1385	1390	35
3.1	1395	1405	120
3.2	1395	1405	120

Table 5.5: Summary of the initial water level conditions and hole diameter of top plate for each test.

Regarding the three pore pressure transducers (PPTs), these were saturated in silicone oil while connected to a vacuum pump. The saturation of the three PPTs was only possible before Test 1 and Test 3, since the excavation of the soil sample after Test 1 was not deeper than the cables, and PPT_1 could not be saturated. However, it could be kept saturated under the soil during the excavation process

from Test 1 and it was unsaturated only for some hours before increasing the water level for sample preparation of Test 2.

For Tests 2 and 3, the pile roughness was not considered, since the pile was sand papered before the tests in order to remove the extra glue around the fibre optics and therefore, the surface was smooth.

5.5.2. Cone penetration test (CPTu)

To characterise the soil profile a piezocone test (CPTu) was performed, pushing the aforementioned explained cone (see section 5.2) into the soil at a constant rate of penetration of 10mm/s by means of the hydraulic plunger. During penetration, the total force acting on the cone (Q_c), the total frictional force acting on the sleeve (F_s) and the pore pressure behind the base of the cone (u_2) during penetration were recorded. After the static CPTu, the cyclic loading tests were performed at 0,1 and 1Hz with an amplitude of 10mm at the tip of the cone. During all these tests, the drain was kept opened and the outflow water was measured (see Appendix G). More details on the procedure of these tests and equipment used is presented in Appendix E.1.

5.5.3. Impact driving

To study the effect of the impact driving method, a weight of 4kg was cyclically and manually dropped by means of a pulley through a 204cm long tube in order to impact on top of the pile. The distance between the gravitational centre of the weight and the top of the pile was between 160 to 167cm. By conservation of energy, the energy with which the pile was being impacted was approximately 8950J. Since the driving method was manual, the frequency of the impacts was tried to be kept approximately to 1 blow every 2 seconds, therefore, the frequency of the drivability was approximately 0,5Hz.

Additionally to the impact driving method, two load tests were performed in between the installation phases. These displacement controlled tests pushed the pile 9mm through the soil. To do so, the manual driving system had to be changed to the hydraulic plunger used for Test 1.
During this test, a constant head was created and the drain was kept opened. The reason for this is that during the pressurizing phase, the water level decreased, as it can be observed in the plots of the outflow of water in Appendix H.

Appendix E.1.1 presents figures showing the weight and guiding system used for penetrating the pile, in addition to a more detailed description of the test.

5.5.4. Jacking

The jacking method pushed the instrumented pile through the soil at a constant penetration speed of 10mm/s, using the same hydraulic plunger for the previous tests was used.

Similarly to the previous test, two load tests were aimed to be performed between the jacking installation phases. These displacement controlled tests pushed the instrumented pile 9mm through the soil using the same hydraulic plunger. The program for this test is summarised in the next Table 5.6. The penetration depths were determined based also on the reused soil used for sample preparation, where the top 220mm consisted of undisturbed soil excavated from the previous tests, and the 320mm below, with non-used sand fraction of glauconitic sand.

Phase	Target depth [mm]	Penetration rate [mm/s]	Remark
1	100	1	Jacking (Check verticality)
2	200	10	Jacking
3	209	0,01	Load test
4	390	10	Jacking
5	399	0,01	Load test
6	450	10	Jacking

Table 5.6: Testing program for jacking driving method.

This program, however, could not be fulfilled, since the resistance of the soil was too high and the instability of the force applied by the plunger on top of the pile lead to its bending and to the sudden detachment of the extra piece used in between during phase 4. Hence, phases 5 and 6 could not be performed since the pile broke 85mm before the phase target level, at approximately 305mm below the top soil.

Additionally, due to the larger hole in the top plate, a CPTu could be performed next to the pile. Nonetheless, for the same reason, the boundary conditions differed from the other tests, and the results from the CPTu were not compared in this research.

Like in the previous Test 2, during the pressurizing phase the water level decreased (as it can be seen in the plots of the outflow of water of Test 3 in Appendix I), reason why during Test 3 a constant head was also kept in order to have the top soil saturated, keeping the drain opened. More details on the procedure of Test 3 are presented in Appendix E.1.2.

5.6. Local relative density measurements

The sample preparation with glauconitic sand was with moist soil, therefore, the calculation of the relative density of the sample was not accurate, since the dry mass was obtained from the water correction for the moist soil. Hence, relative density needed to be calculated locally after each test was finished. Besides, these measurements allowed for local variation checks of the soil model prepared, since the samples were taken from undisturbed areas around the cone or pile.

To do so and in order to keep the soil saturated to take the samples, the water level was lowered no more than 25cm below the top soil surface so that the capillary action of the suction forces maintained the strength of the soil. In total, 12 samples of from each model prepared were taken after the tests: 4 samples of the same volume per layer. The thickness of the 3 layers were depending on the final depth penetration from the test installation. A detailed description on the procedure to obtain the samples, equipment, calculations and numerical results are presented in Appendix F.

Chapter 6

Results

6.1. Local relative density measurements after tests

After excavating the soil in 3 layers after each test and by taking 4 samples from each layer, the local density index measurements based on the relative position between the void ratio and the minimum and maximum void ratio measured, were determined. The results for each soil model with depth are shown in Figure 6.1a. It can be observed a more or less constant variety of the local density for the soil models and no trends with depth. Some deviations might be resulting from the difficulty of the determination of $\rho_{d,min}$ and $\rho_{d,max}$ and the small difference there is between them, and as a consequence, the e_{min} and e_{max}, and the accuracy in the obtention of the samples. Nonetheless, overall, the sample preparation led to a dense state of ranging between 60-80% relative density. In addition to this, the bulk densities from the samples taken at each layer are also plotted in Figure 6.1b, indicating a very constant value over depth ranging between 1,6 and 1,7g/cm^3 for all the soil samples.

The table including all the results from these calculations can be found in Appendix F.

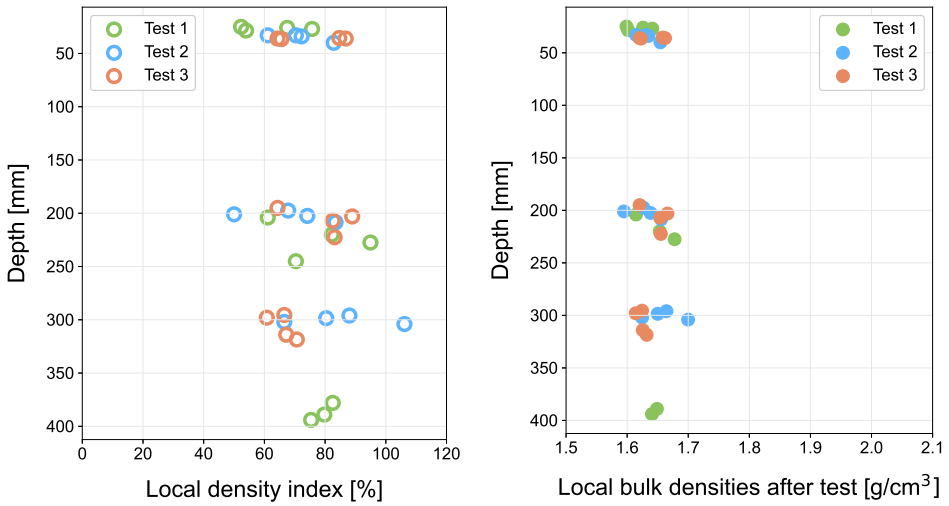


Figure 6.1: a) Local indexes and b) bulk densities, after tests over depth below the surface level where the samples where taken.

6.2. Test 1 - CPTu

In the following subsections, the results obtained from the static and cyclic CPTu performed in the glauconitic sand are shown. These include the cone readings. However, the pore pressure transducers (PPTs) recordings are not included since there was a strong correlation between the force applied and displacement of the cone and pile. Hence, the results seemed to be affected by mechanical deformations of the membrane of the PPTs indicating a reaction to the axial loads. Therefore, the readings

cannot be used as measurements of the horizontal pore pressures.

Regarding the cyclic loading, it should be mentioned that the CPTu is not designed for cyclic loading and maybe this is depicted in the results obtained.

The following measurements have been all zeroed at the moment of starting the tests.

6.2.1. Static CPTu

The static CPTu pushed the cone at a constant rate of 10mm/s for a distance of approximately 400mm below the top soil (≈16D).

- **CPTu readings**

  The difference between q_c and q_t was not visible, and they both rapidly increased with depth as a consequence of the constant vertical stress applied at the top boundary (200kPa) and an increment of vertical stresses with depth due to the weight of the soil. The strength of the material was reached and the maximum resistance was 35MPa. The sleeve friction (f_s) readings were reliable starting at depth 59,7mm when the friction sleeve was fully embedded in the soil. It increased with depth the first 120mm and reached its maximum value at approximately 0,15MPa, afterwards, it decreased with depth and reached another peak. The friction ratio (R_f) followed a similar curve to the sleeve friction, reaching its maximum approximately at 0,42%. The pore pressure (u_2) measurements were irregular at shallower depths and they increased linearly with depth from 110mm below the top surface, indicating a more constant generation of pore pressures. The u_2 reached 35kPa, about 10 times above the hydrostatic conditions at that depth. Figure 6.2 shows the results of the measurements.

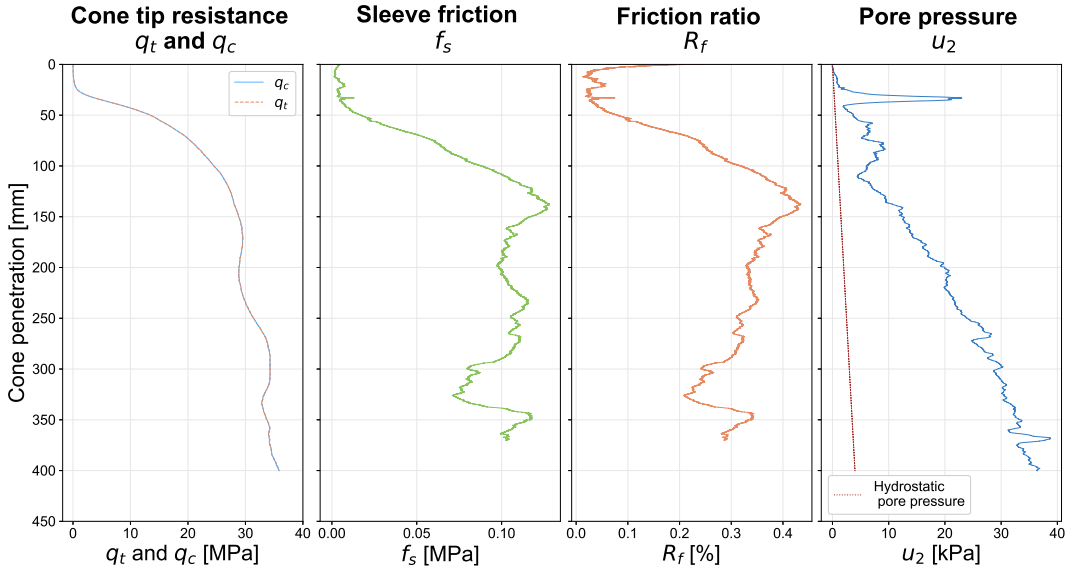


Figure 6.2: Profile showing the readings from CPTu static test over depth below top surface.

- **Force plunger and cone tip resistance**

  The force applied by the plunger on top of the cone increased with depth as so did the strength, as shown previously. The following Figure 6.3a shows the recordings of the force acting on the cone in comparison with the force applied by the plunger to push the cone into the soil, and a difference increasing with depth is observed, starting 750mm below the top soil, approximately. The difference of these two measurements indicate the overall side friction from the cone being penetrated in the soil, increasing with depth (Figure 6.3b). From dividing this value by the cone tip area and the length embedded in the soil, the overall shaft friction (τ) can be obtained. This is plotted in Figure 6.3c in comparison with the local sleeve friction (f_s) measured from the cone. It can be observed a reduction of overall friction with increasing cone penetration while the local sleeve friction measured at the

sleeve increased. The friction at the sleeve was higher than the overall friction. The negative values correspond to the negative force of the plunger at the beginning of the test, which might be a result of bending of the load cell.

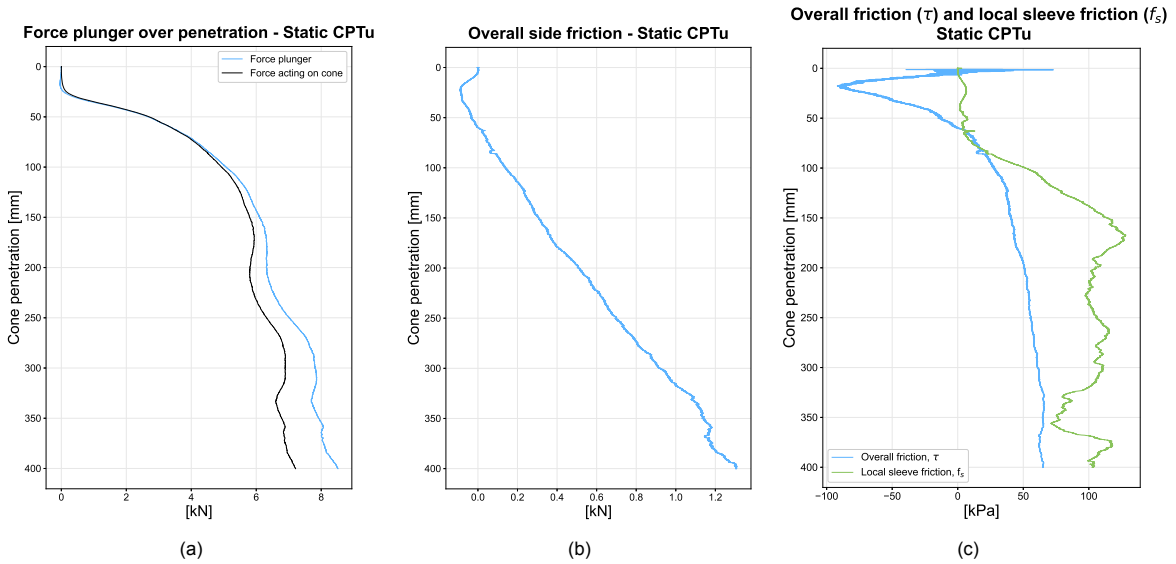


Figure 6.3: In static CPTu test, with depth: a) Force plunger and cone resistance; b) Overall side friction; c) Overall friction and local shaft friction.

6.2.2. Cyclic CPTu - 0,1Hz and 1Hz

In this subsection, the results from both cyclic CPTu performed at frequencies 0,1Hz and 1Hz are shown. The cyclic displacement half-amplitude (Δw_{cyclic}) was 5mm. The first loading regime at 0,1Hz started from the final penetration reached from the static CPTu, 16D (400mm), with a downward movement up to depth 405mm and the number of cycles applied were 165. Afterwards, the frequency was increased to 1Hz. In this second cyclic loading, 399 cycles were applied.

- **Cone readings**

  In the profiles shown in Figures 6.4 and 6.5, the results from the CPTu recordings with time are shown, together with specific number of cycles (N). For the loading regime at 1Hz, the R_f is not shown due to the insignificant values resulting from the small f_s values and large q_c.

  The initial value of the q_c readings for the first loading regime at 0,1Hz coincided with the last resistance registered from the previous static CPTu test (35MPa). On the contrary, for the cyclic test at 1Hz this does not occur since a progressive increment of the displacement amplitude was applied before starting the second loading. For the first scenario at 0,1Hz, the cone tip resistance, decreased as cyclic loading progressed during the early stages of cycling, in the first 65 cycles, reaching 12MPa. Starting from cycle 65, the resistance increased with the number of cycles, reaching up to 42MPa at the end of the loading (Figures 6.6 and 6.7). This change in resistance was correlated with a lower displacement amplitude of the plunger at the same time (t<700s). For the second scenario at frequency 1Hz, the resistance of the soil tended to increase 10kPa with the number of cycles. However, compared to the previous loading regime, the developed q_t profile over the number of cycles was not uniform over the loading and oscillations are observed (Figure 6.6).

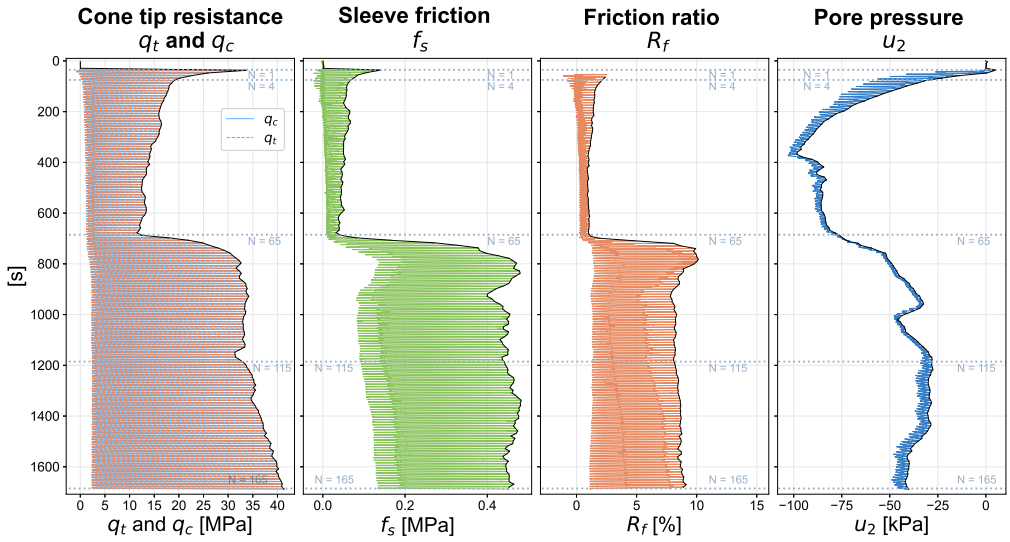


Figure 6.4: Profile showing the readings from cyclic CPTu test at 0,1Hz over time. The black line indicates the values in the downward movement of the plunger.

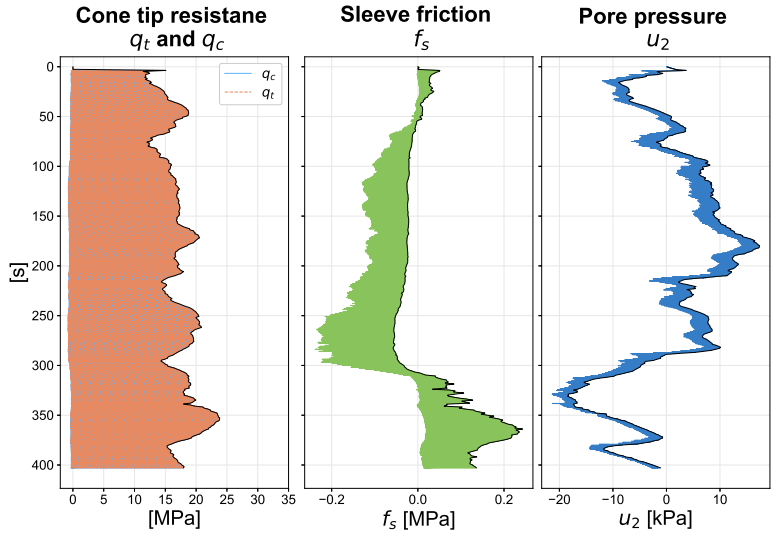


Figure 6.5: Profile showing the readings from cyclic CPTu test at 1Hz over time. The black line indicates the values in the downward movement of the plunger.

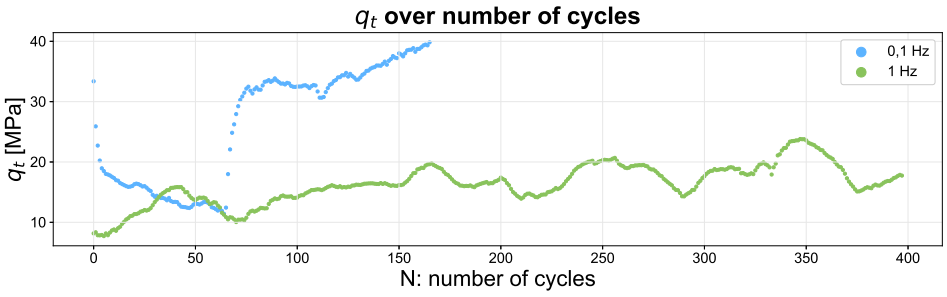


Figure 6.6: Evolution of q_t over number of cycles (N) in cyclic CPTu tests. q_t values correspond to the downward movement of the cone (maximum value).

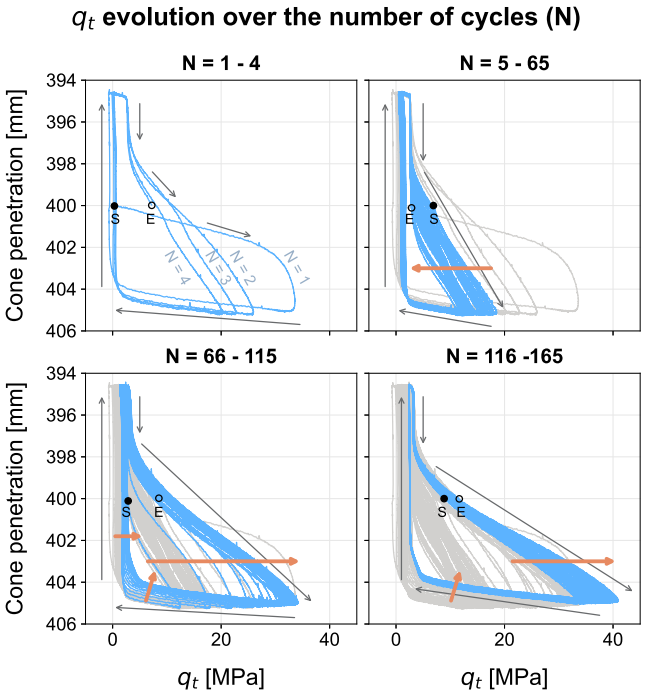


Figure 6.7: Evolution of q_t versus the displacement of the cone tip with the number of cycles (N) in cyclic CPTu test at 0,1Hz. *S* and *E* indicate the start and the end of the range of cycles plotted.

The evolution of f_s with number of cycles can be compared with respect to the faster cyclic loading at 1Hz. In Figure 6.8 similar initial values are observed for both tests. Nonetheless, while the f_s increased suddenly after 63 cycles in the 0,1Hz loading, it decreased smoothly during 290 cycles during the 1Hz test, developing negative values, and increasing 0,4MPa the following 70 cycles.

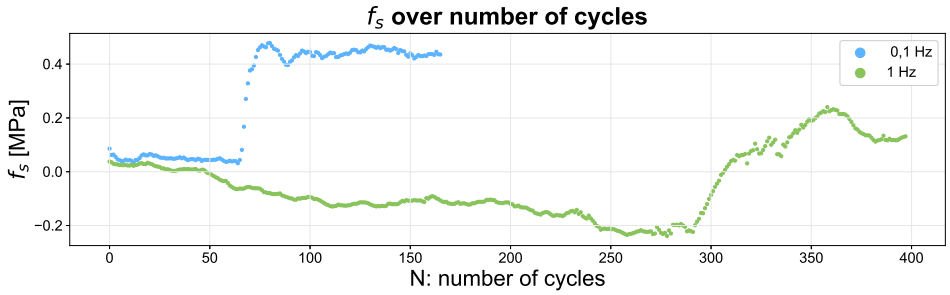


Figure 6.8: Evolution of f_s over number of cycles (N) in cyclic CPTu tests. f_s values correspond to the downward movement of the cone (maximum value).

Regarding the measured pore pressures, u_2, dissipation was registered as the cycling loading started reaching up to -100kPa (Figure 6.10), followed by a continuous increase up to -30kPa, during the first cyclic loading at 0,1Hz. The following cyclic loading at 1Hz registered oscillating positive and negative u_2 values, reaching 20kPa and -20kPa after 170 and 330 cycles, respectively. The decrease of u_2 coincides with the increment of f_s at approximately cycle N=290. The evolution of u_2 with the displacement of the cone over the number of cycles for the test at 0,1Hz is plotted in Figure 6.11. After the tests, the pore pressures tend to stabilise and recover to the initial pressure (see Appendix G.2 and G.3).

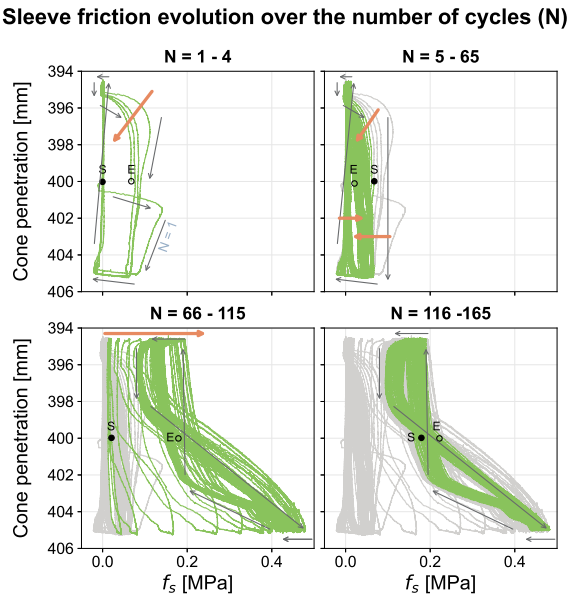


Figure 6.9: Evolution of the sleeve friction (f_s) versus the displacement of the cone tip with the number of cycles (N) in cyclic CPTu test at 0,1Hz.*S* and *E* indicate the start and the end of the range of cycles plotted.

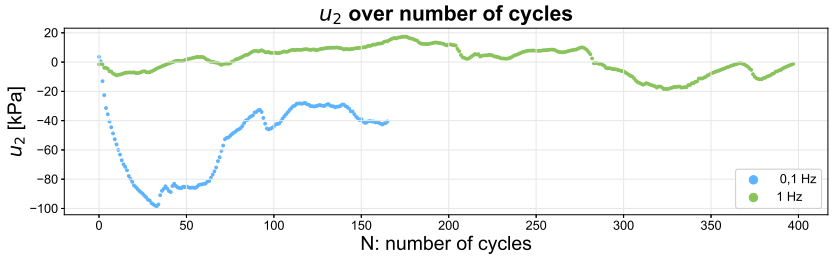


Figure 6.10: Evolution of u_2 over number of cycles (N) in cyclic CPTu tests. u_2 values correspond to the downward movement of the cone (maximum value).

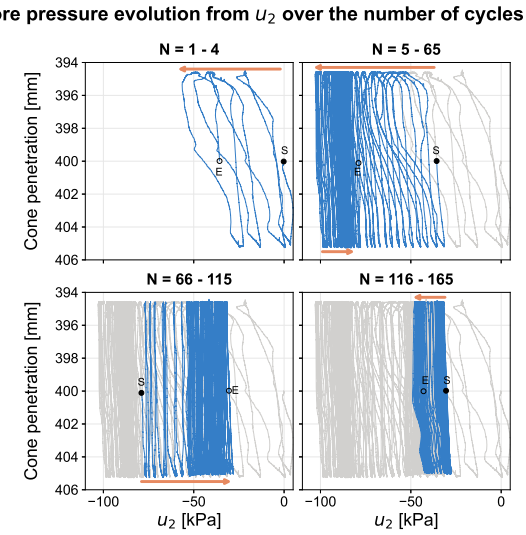
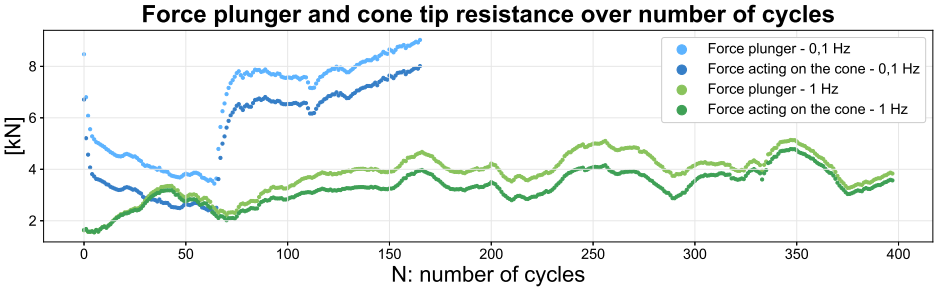


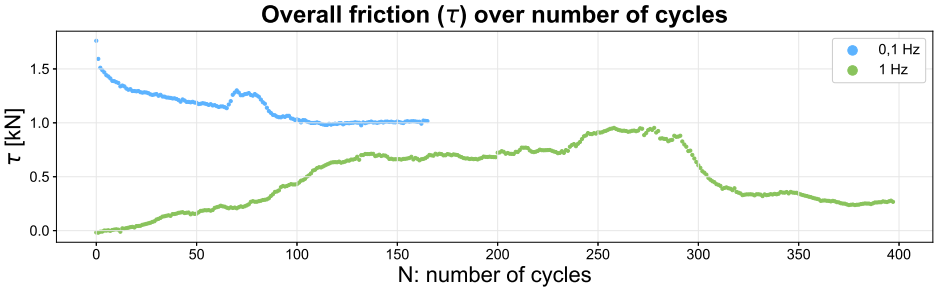
Figure 6.11: Evolution of the pore pressure (u_2) versus the displacement of the cone tip with the number of cycles (N) in cyclic CPTu test at 0,1Hz. *S* and *E* indicate the start and the end of the range of cycles plotted.

- **Force plunger and force acting on the cone**

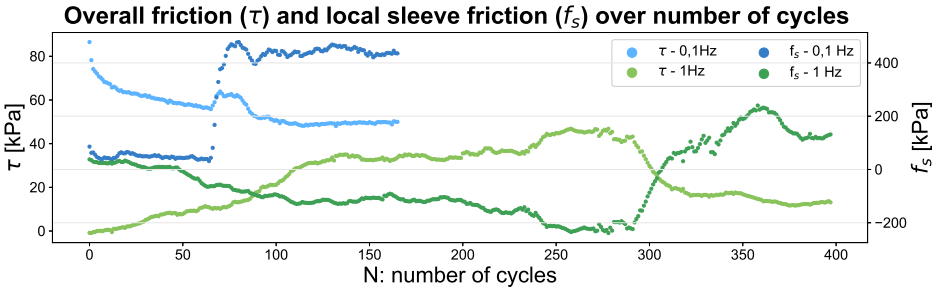
  During downward movement of the cone in both cyclic tests, the tip resistance showed good resemblance with the plunger (Figure 6.12a), both increasing as the loading progresses. Nonetheless, there was some difference between both measurements, for both tests, indicating friction from the side cone increasing with number of cycles. The following Figure 6.12b indicates the overall friction from both cyclic loading regimes calculated as the difference between the force of the plunger and the force acting on the cone tip, plotted as a function of number of cycles. The friction corresponds to the value measured during downward movement of the cone and it was larger for the test performed at 0,1Hz. The decrease of overall friction in test at 1Hz at N=300, approximately, coincides with the increase of f_s and the decrease of u_2. Moreover, the overall friction can be compared to the local sleeve friction measured in the cone, f_s (Figure 6.12c). For the case of cyclic loading at 0,1Hz, after the jump of the friction at the sleeve (f_s) at N=63, this was higher than the overall friction, like in friction fatigue models. The same occurred at the beginning and at the end of the second cyclic loading regime at 1Hz (0<N<100 and 300<N<399).



(a)



(b)



(c)

Figure 6.12: In cyclic CPTu loading, evolution of: a) Force of the plunger and cone resistance; b) Overall friction; c) Overall friction and local sleeve friction; with number of cycles (N). All the values correspond to the downward movement of the cone (maximum values).

6.3. Test 2 - Impact driving

This section provides the results obtained after penetrating the pile up to 17,6D depth (440mm) using impact driving method. The test was undrained and the total number of blows counts (BC) needed to achieve this depth was 583. Figure 6.13 includes the plot of the blow counts measured during pile installation and it shows an increase with depth. The relationships between BC and penetration (mm) are obtained from the slopes marked in the plot. These results together with the phases followed to fulfill this test are summarised in Table 6.1. The soil pressure measurements registered from the sensors located at different depths in the instrumented pile are shown hereafter.

Phase	Reached depth [mm]	Remark	Blows per phase	[mm/BC]	[BC/mm]
1	210	Impact driving	209	1	1
2	219	Load test	-	-	-
3	389	Impact driving	323	0,53	1,9
5	398	Load test	-	-	-
6	440	Impact driving	51	0,83	1,21

Table 6.1: Testing program and results from impact driving method test.

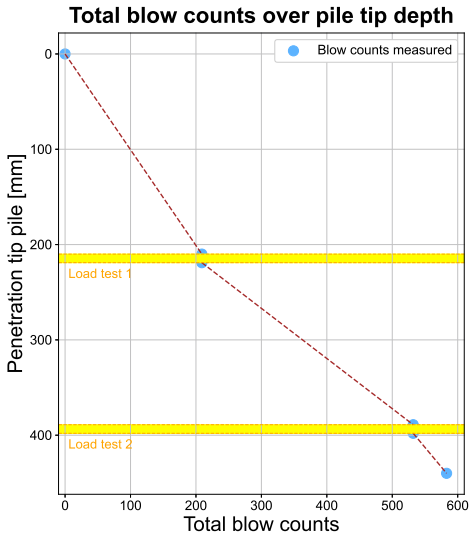


Figure 6.13: Blow counts measured over depth for pile installation during impact hammering.

- **Soil pressures**

  The continuous monitoring of the soil pressures throughout the test is provided in Figure 6.14a. The plot shows the measurements of the working sensors indicating their position in the pile relative to the pile diameter (D). In general, an increase in the total stresses in the soil around the lower part of the pile is noticed, indicating the soil being pushed radially away from the pile tip. More specifically, it can be observed the effect of the pile head being embedded in the soil during the first phase of driving, where the pressures increased more abruptly that in the rest of the phases. In the final measurement, the stresses measured at the same level h/D = 0,6 were very similar. On the contrary, the sensors at level h/D = 3,6 measured different values. Besides, the sensors responded to the weight impacting the pile, observed in the plot with spikes. The load tests measurements indicate a decrease in stresses followed by a stabilisation towards their initial value, except for sensor 4 which increases drastically.

  On the other hand, the measurements corresponding to the sensors located at the same level do not resemble. This could be due to the configuration of the sensors, being sensitive to the axial load applied by the blows and the non-homogeneous stress distribution around the pile. The average

results measured at each level are plotted in the next Figure 6.14b, indicating more stresses in the lower sensors during the first two installation phases using impact hammering, and similar stresses after the first load test.

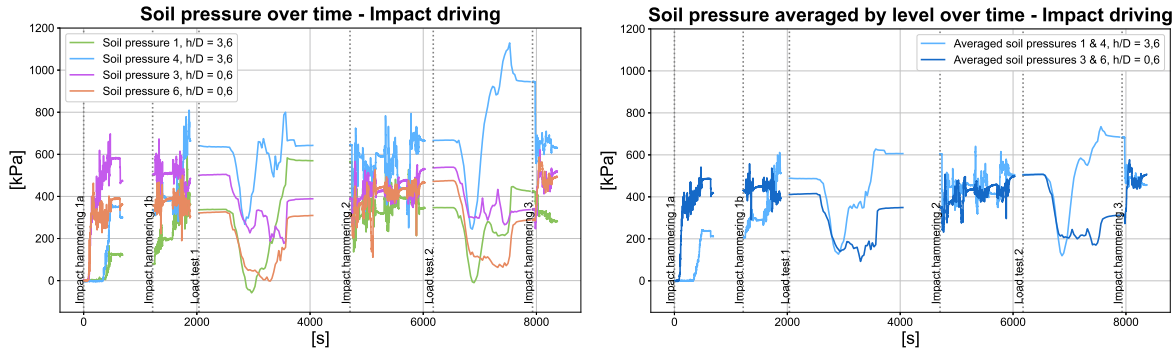


Figure 6.14: a) Evolution of the soil pressure measured in the pile over time during impact driving test; b) Evolution of the soil pressure measured in the pile, averaged by level over time during impact driving test.

6.4. Test 3 - Jacking

In this section, the recordings from the soil pressure sensors and the force of the plunger obtained during jacking installation are shown. Nonetheless, the pile was pushed at a constant penetration rate of 10mm/s approximately 12,5D (310mm) below the surface, when it bended.

- **Soil pressures**

  In this test, there were also differences in the measurements of the sensors located at the same level (Figure 6.15a). However, the average results of the soil pressures at lower level h/D = 0,6 indicated larger stresses than the ones at higher level at h/D = 3,6 during all the test, indicating a more uniform stress distribution in the soil (Figure 6.15b), in comparison to the impact driving results. In the initial installation phase, as the pile was pushed into the soil, the sensors responded rapidly to the stresses applied increasing more rapidly than in impact driving and registering larger values, except in sensor 3. During the load test, the stresses decreased and tended to stabilise afterwards, although each sensor behaved differently. The spike at approximately t = 3200s indicates the bending of the pile. After that, the sensors did not measure any change in stresses.

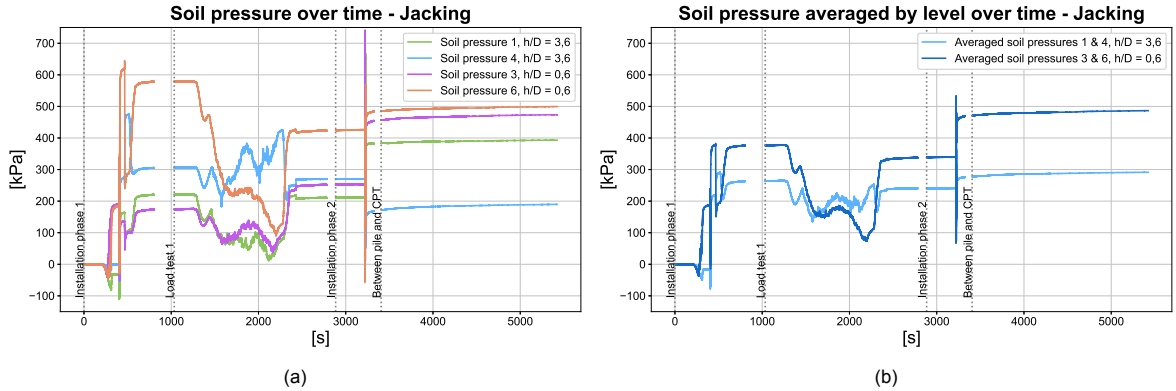


Figure 6.15: a) Evolution of the soil pressure measured in the pile over time during jacking test; b) Evolution of the soil pressure measured in the pile, averaged by level over time during jacking test.

- **Force of the plunger**

  The force of the plunger applied on top of the pile during jacking can provide information regarding the achieved resistance of the soil and the uniformity of the sample preparation, if compared to the first test results. In Figure 6.16a it can be observed that during jacking installation, the force applied by the plunger in order to drive the model pile was almost three times larger than the force to penetrate the cone throughout the soil in Test 1. In addition to this, the penetration of the pile was not smooth, as it can be observed in the oscillations of the profile. This was observed when the pile tip was 140mm, approximately, below the top soil. This could indicate a looser state on the first 100mm of soil in the model. During the load test, the force applied to install the pile 9mm deeper reached 17kN, 5kN less than the final force applied during the first installation phase. In the second installation phase the force applied by the plunger increases with depth and it kept oscillating. At depth 300mm the pile bended.

  If the force of the plunger in Test 3 is divided by the pile tip surface, the resistance during jacking the model pile can be obtained. In this case, however, no side frictions are considered. Figure 6.16b depicts the resistance curve calculated compared to the cone resistances from Test 1. In this case, the differences are smaller indicating similar resistances in the soil, reaching 35MPa, and therefore, similar soil uniformity as a result of the sample preparation.

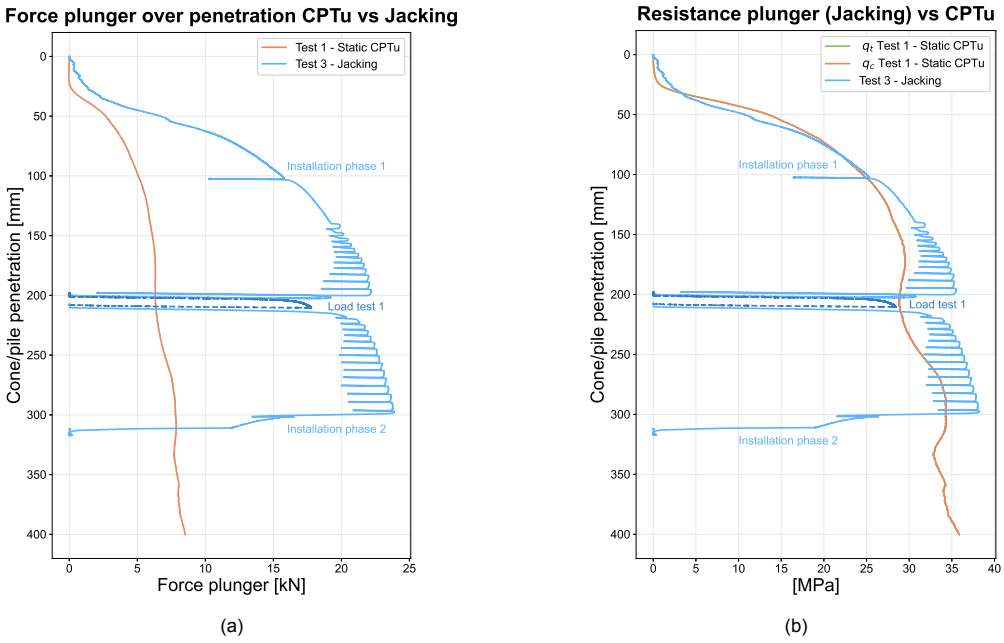


Figure 6.16: In cyclic CPTu loading, evolution of: a) Force of the plunger and cone resistance; b) Overall friction; c) Overall friction and local sleeve friction; with number of cycles (N). All the values correspond to the downward movement of the cone (maximum values).

6.5. Shear band and tip

After each test was completed and the density samples were obtained, the soil around the cone and pile was excavated. This section provides the taken photographs of the cross-sections showing the shear band adjacent to the cone and pile's shaft and around their tip due to crushing of glauconite pellets, distinguishing per test, in order to further analyse the following observations.

Due to the green color of the crushed particles compared to the darker sand undisturbed from the soil sample, the crushed zones can be easily identified. Moreover, as a result of the crushing leading to a higher plasticity and change in soil-type material, the clay-like soil can be separated from the coarser

sand particles.

6.5.1. Test 1 - CPTu Static and cyclic

The excavation to see the cross section of the soil to observe the crushed soil around the shaft was made in two phases. Firstly, the first 230mm were excavated. The green crushed soil from the shaft started to be observed at 5mm from the shaft (measured at the top soil). The deformation of the soil can also be observed in the pink sand layer (180mm depth), indicating the soil being pushed downward. See the following Figure 6.17.

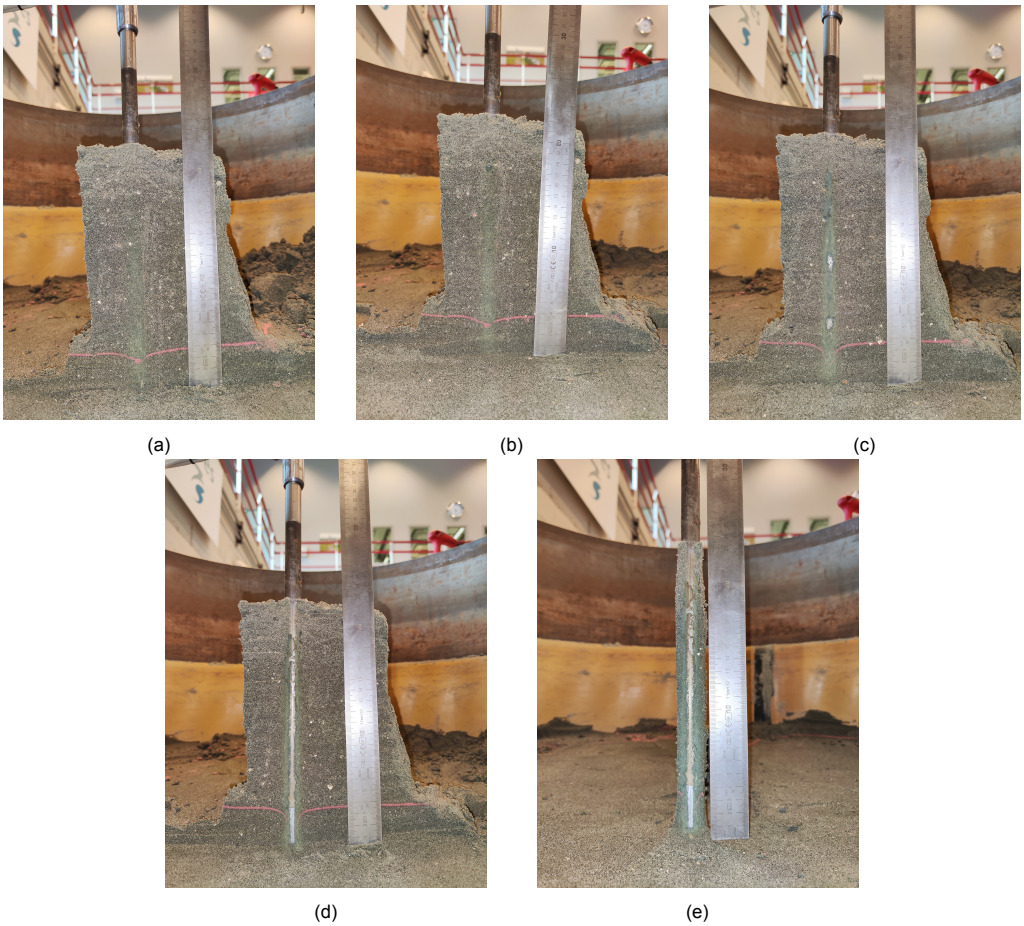
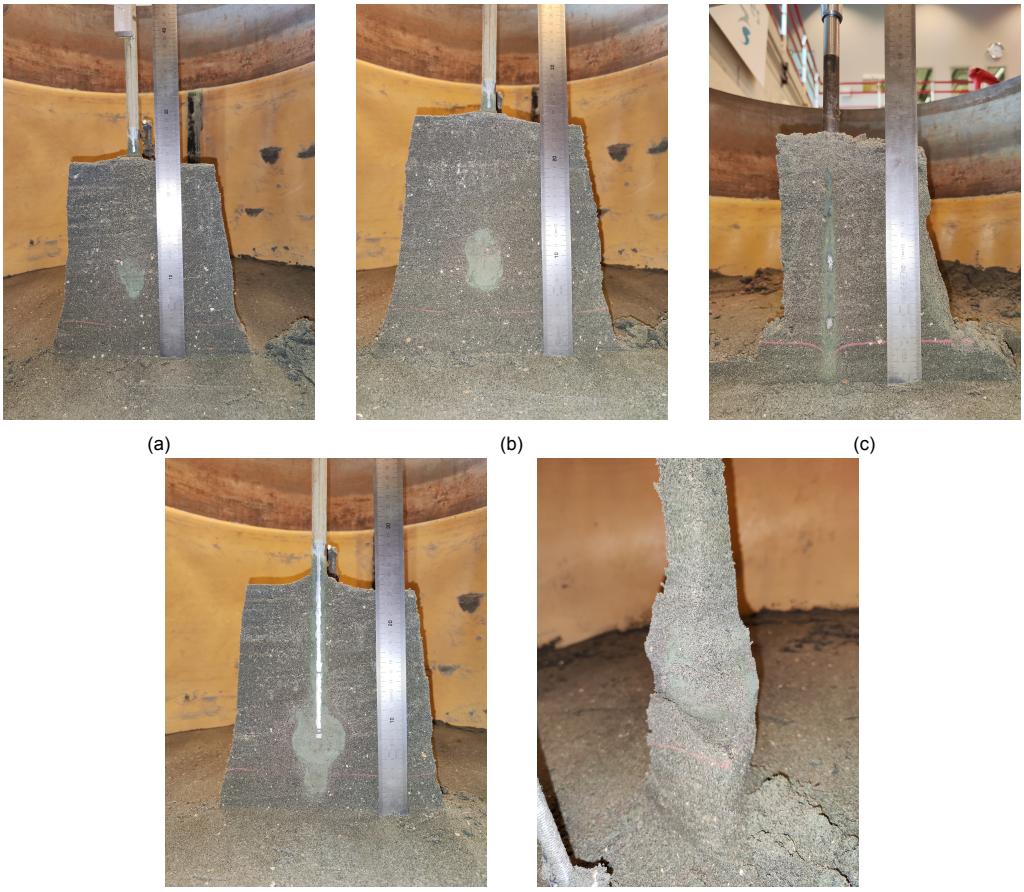


Figure 6.17: Cross section of 23cm excavated soil after Test 1 at different distances from the cone: a) 5mm, b) 3mm , c) 0-2mm, d) 0mm. e) Only crushed soil around the shaft.

The second phase reached the tip of the cone at 16D depth (Figure 6.18). In this case, the green crushed soil at the tip started to be observed 25mm from the cone, wile the crushed soil at the shaft was observed at the same distance as at the top excavation, meaning a larger crushed volume around the tip. In this case, the deformation of the soil could not be observed because the pink layer (at 435mm depth) was not thick enough closer to the cone and it was far from the tip.

The size of the bulb of crushed soil around the pile, indicates that the crushed soil has been pushed aside significantly. Moreover, it should be noted that in these photographs the tip of the cone is at 400mm depth and the cyclic displacement amplitude was 10mm, meaning the tip of the cone did not even reach the edge of the circular crushed soil shape (20mm below the tip of the cone) or the ”nose-shaped” (50mm below the tip) and the bulb was surrounding the whole tip and part of the friction sleeve.

Due to the clear difference in soil type between the transformed crushed soil and ”undisturbed” soil,



(a) (b) (c)

(d) (e)

Figure 6.18: Cross section of second phase of excavated soil after Test 1 at different distances from the cone: a) 25mm, b) 10mm , c) 0-2mm, d) 0mm. e) Excavation process after identifying sphere shape for tip bulb.

the bulb created around the tip could be collected. Figure 6.19 shows its dimensions. It can clearly be observed that the crushing occurred around the tip of the cone without this reaching the crushed zones.

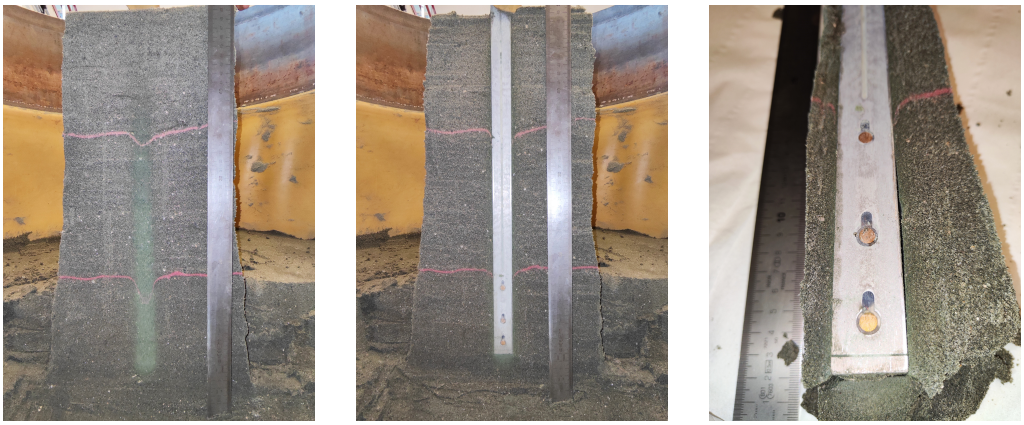


(a) (b) (c) (d)

Figure 6.19: Cross section of bulb tip excavated after Test 1: a) Front, b) Back , c) Side 1, d) Side 2.

6.5.2. Test 2 - Impact driving

The crushing happening after installing the pile using the impact driving method was observed 5mm from the pile's shaft. This crushing is affected by the shape of the pile, as suggested by Thi Viet Phuong (2019). The flat pile tip pushes the soil mainly downwards with the same displacement of the pile leading to slightly heave occurring in the layers adjacent to the pile. The following Figure 6.20 shows the deformation of the soil in the pink layers (at 130mm and 270mm deep) as well as the thin shear band attached to the pile's shaft. The resulting crushed soil around the tip of the pile is like a half spherical shape 20mm below the tip at final penetration (see Figure 6.21).



(a) (b) (c)

Figure 6.20: Cross section of the excavated soil after Test 2: a) 15mm (top) to 5mm (bottom) from the pile's shaft, b) 0mm from the shaft. c) Closer view at the pile tip and shaft crushed. -2mm, d) 0mm. e) Only crushed soil around the shaft.



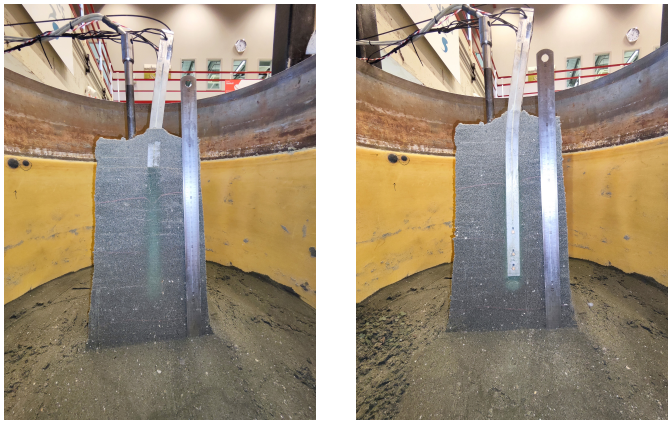
(a) (b)

Figure 6.21: Cross section of bulb tip excavated after Test 2: a) Front, b) Back , c) Side 1, d) Side 2.

6.5.3. Test 3 - Jacking

After the pile installation using jacking method, the observed crushed soil around the pile's shaft was observed 5mm from the pile. In Figure 6.22, it can be seen the effect of the larger hole through which the pile was penetrated, leading to a less compacted soil at the top, and as a consequence, a shear band starting 80 - 90mm below top surface. In this same figure, the resulting bending of the pile can be observed, as well as the soil deformation indicating downward movement of the soil in the pink sand layers. Moreover, since crushing is affected by the shape of the pile (Thi Viet Phuong, 2019), the bulb obtained around the tip of the pile resembles a half spherical shape 20mm below the tip of the pile. Figures 6.24a and 6.24b show the bulb collected at the tip of the pile, where lines can be observed showing large compression stresses as a result of penetration.

The cone penetrated 400mm next to the bended pile in Test 3, created a shear band 2mm thick around all the cone. In this case, no bulb was created around its tip. The following Figure 6.23 shows this crushing and how the shear bands resulting from the jacking installation of the pile almost interfere with



(a) (b)

Figure 6.22: Cross section excavated soil after Test 2: a) 1,5mm from the top and 5mm from the bottom, b) 3mm , c) Closer view at the pile tip and shaft crushed. -2mm, d) 0mm. e) Only crushed soil around the shaft.

each other due to the lost of verticality of the pile when it bended. moreover, the deformation of the soil is observed in the pink layers (located at 110mm and 210mm depth).



(a) (b) (c) (d)

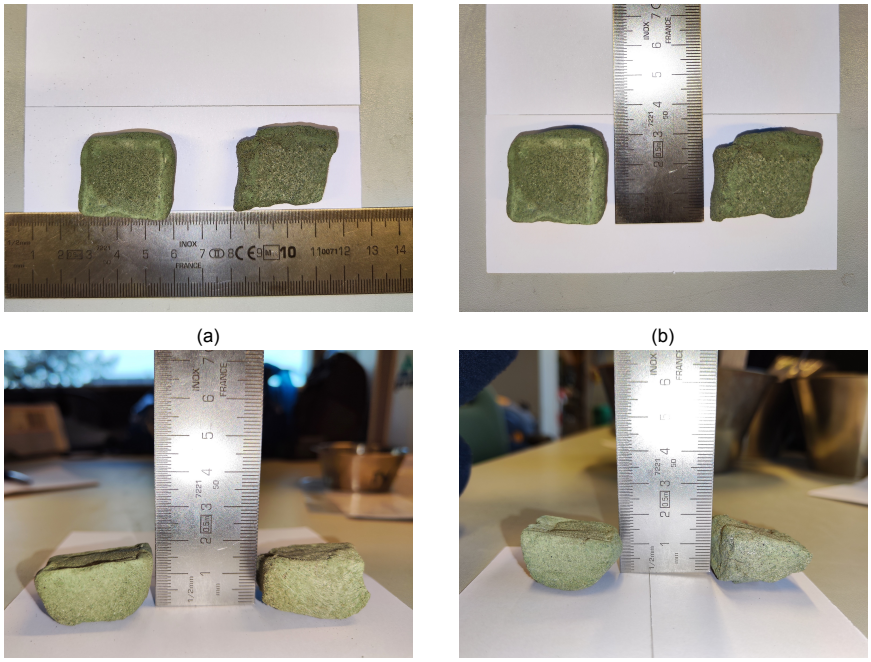
Figure 6.23: Cross section excavated soil after Test 3: a) and b) 0-2mm distance from the cone shaft, c) Corner view of the excavation and d) Front view of the excavation.



(a) (b) (c)

Figure 6.24: a) and b) Bulb tip excavated after Test 3 around pile tip. c) Tip of the cone after penetration, showing no bulb around it.

The following Figure 6.25 shows the bulbs obtained around the tip of the pile after the crushing of glauconite pellets in tests 2 and 3, namely, impact and jacking driving methods. Both have similar dimensions and shape, although the bulb obtained from jacking had lines indicating high compression stresses (Figure 6.26e).



(a) (b) (c) (d)

Figure 6.25: Photographs of the bulbs obtained from Test 2 (after impact driving, left bulb) and after Test 3 (jacking right bulb): a) Top, b) Top , c) Side 1, d) Side 2.

6.6. Crushing of the glauconite pellets

After performing the tests and excavating the soil around the cone and the pile, the crushed soil was collected and oven-dried to 110ºC in order to perform granulometry tests and study the crushability of the glauconite sand after different installation methods. The analysis were done using the Malvern Mastersizer 3000 equipment due to its better quantification of fines.

For the analysis, distinction is made between the crushed soil at the tip and the shaft for all the tests. Nonetheless, in every test, the soil corresponding to the shaft lead to smaller amount of fines compared to the soil collected from the tip. This could be due to the accuracy of the obtention of the samples, since the shear band was thinner and that might have included some coarser particles attached to the clay-like soil (see Figure 6.26). Figure 6.27 shows the percentage passing as a function of the opening of the sieve, indicating the Particle Size Distribution (PSD) curves. It can be noticed that there is almost no difference between the curves representing the soil collected at the tip of the piles using jacking or impact driving method, and they both indicate a slightly larger amount of fines regarding the soil collected at the tip of the Test 1. Nonetheless, the PSD curve for the crushed soil collected at the shaft of the cone after Test 3 indicates larger amount of fines in comparison to the one collected at the pile shaft after impact driving and jacking, respectively. Moreover, a difference can be observed in the amount of fines in the shaft crushed material collected from the first and second phases of excavation (in the plot referred as *top* and *bottom*) from Test 1, showing larger amount of fines in the top layer.

Figure 6.28 shows the comparison of the previously shown PSD curves from different samples obtained from the as-received soil, the sand fraction after removal of fines used for the sample preparations, in comparison to the crushed soil PSD curves just shown in Figure 6.27 previously shown without any



Figure 6.26: Photographs taken from the collection of crushed soil around the pile and cone shafts. a) Soil from the three other sides attached to the pile that were not excavated in the cross-section. b) Shaft soil around the cone. c) Thin layer of crushed soil at the shaft of the pile in Test 2. d) Side view of one of the blocks of the soil around the pile to show the 2mm thickness of the shear band and degradation from coarser material to crushed. e) Front view of the soil that was in contact with the pile and the thin shear band around it. f) Sand adjacent to the cone.

distinction between driving methods. These curves mix the results from the analysis obtained with the Malvern equipment (indicated with *M.* in the legend) and the sieve analysis according to ASTM, 2007. From the plot it can be clearly seen a transformation from a poorly graded silty sand from the as-received soil, to a homogeneous fine sand after removal of fines used for sample preparation, to an increase in fine-grained content as observed by Van Alboom et al., 2012 mainly from an increase in silt sized particles followed by clay sized particles (see Figures 6.26f, 6.29 and 6.30) after crushing particles due to cone and pile installations. Numerically, the fines production increased to 20 to 40 % approximately, with respect to the initial type of soil used for sample preparation. With it, an increase in plasticity is also noticed. This is shown in Figure 6.31.

6.7. Discussion of the results

From the results showed from the static CPTu, the generation of pore pressures increasing with depth after depth 110mm could be caused by the change in drainage conditions around the u_2 sensor due to the crushing of glauconite pellets and the transformation into a clayey-silty soil, leading to a partially undrained condition. The dissipation of pore pressures after the test is plotted in Appendix G.1. Moreover, as observed in Figure 6.3c, where the overall friction reduced as the cone was further penetrated into the soil, indicates the reduction of volume as a result of the crushing of glauconite pellets at the boundary between the cone (or pile) - soil interface, allowing the soil further from the shaft to relax the stresses acting on the cone or pile, therefore, leading to friction fatigue.

Concerning the cyclic loading at 0,1HZ, the decrease in pore pressures reaching -100kPa lead to suc-

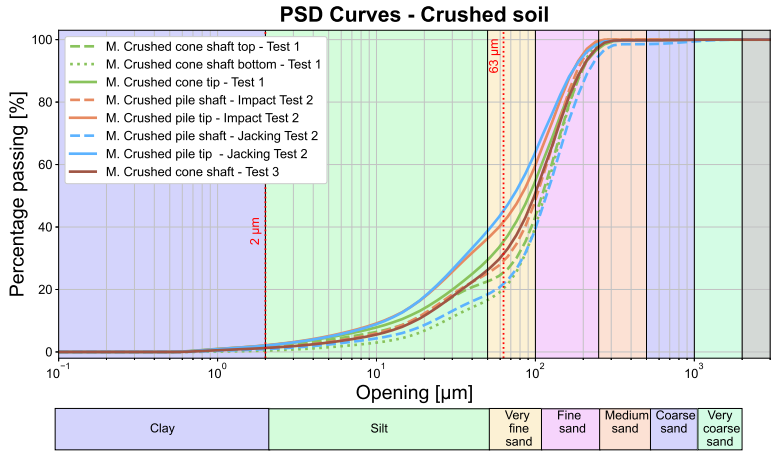


Figure 6.27: PSD curves of crushed soil from samples obtained from the shaft and the tip of the cone and pile after tests.

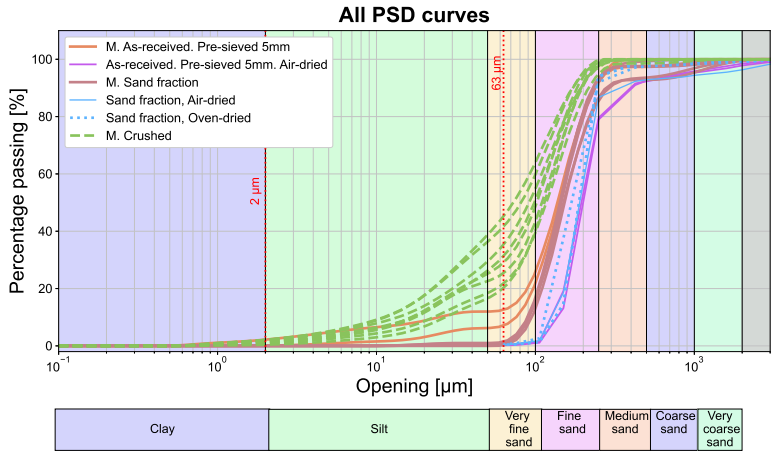
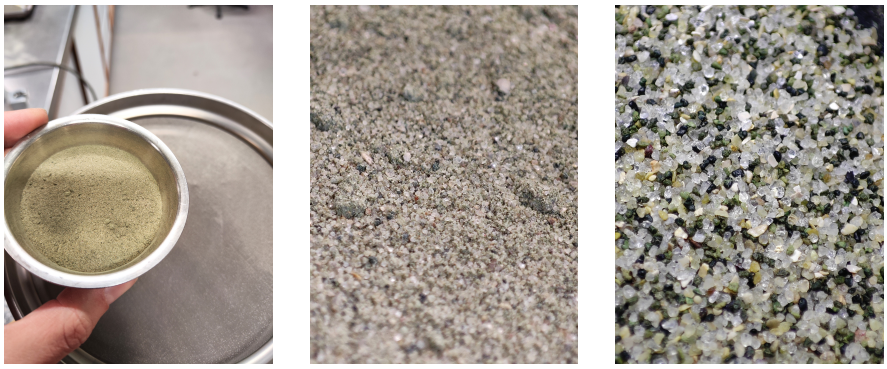


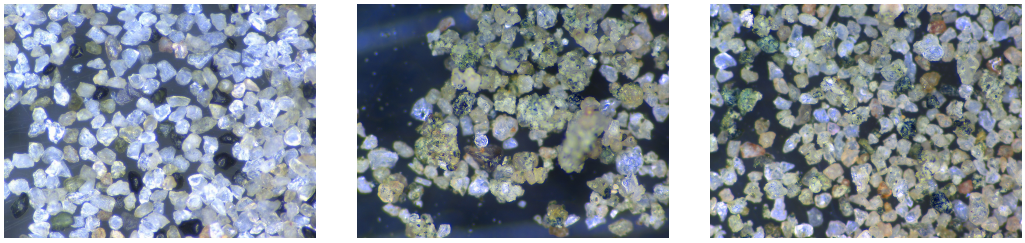
Figure 6.28: All PSD curves together combining as-received soil, sand fraction after washing out the fines and crushed soil.



(a) (b) (c)

Figure 6.29: a) Crushed soil oven-dried to 100ºC. Photographs taken with function *macro* of phone: b) Oven-dried to 110 ºC crushed soil from cone shaft (Test 1). c) Particles retained after performing traditional sieving tests at sieve 's opening 150 μm

tion and it could be thought to be caused by a loss of contact between the cone tip and the sand (Galvis-Castro et al., 2023), creating a small gap. However, the minimum values of q_c reached 0 the first 2 cycles, meaning there was a loss of contact only in these cycles (Figure 6.32). The following cycles, the minimum values of q_c always registered some resistance, meaning that maybe there was some crushed soil attached to the cone due to the increase in plasticity. The negative values, and therefore, the suction, were giving strength to the soil. Another cause for these negative values was



(a) (b) (c)

Figure 6.30: Images captured with the digital microscope using magnification range of 6x from: a) Soil used for sample preparation after removal of fines retained at sieve's opening 106 μm; b) and c) crushed soil around the pile tip after Test 2 (impact driving)



(a) (b) (c)

Figure 6.31: a) Observation of possibility of roll the particles indicating increase in plasticity. b) Increase in plasticity observed because of the difficulty of removing the soil around the cone (and pile) very adhered to shaft. c) Thin sheared dark soil from the shaft of the cone.

thought maybe to be caused by the smectite clay from the inside of the pellets, that once they were crushed, they allowed for the interaction between this swelling mineral and the water, leading to negative pore pressures.

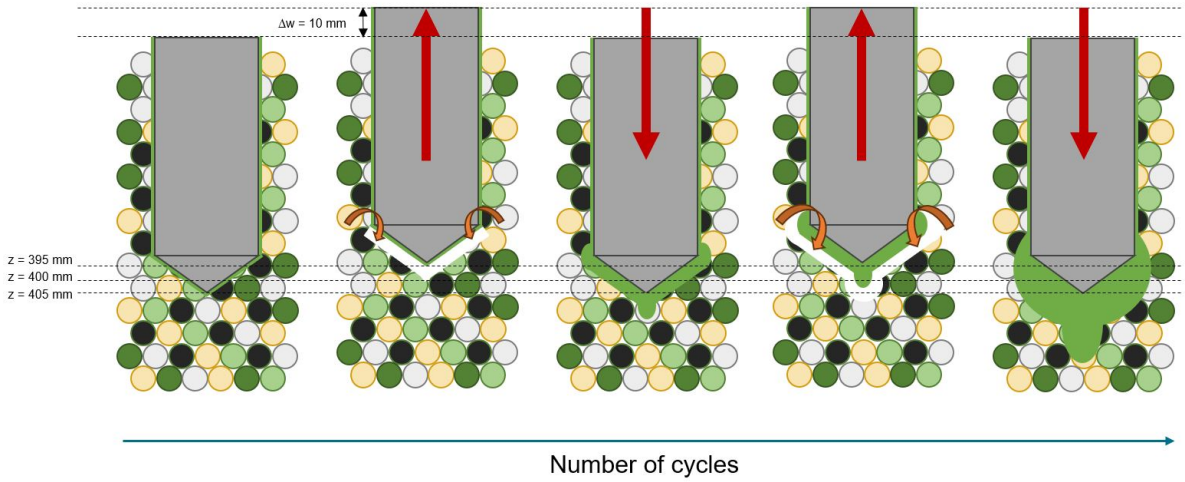


Figure 6.32: Hypothesis of the crushing mechanism during cyclic loading: Loss of contact between the cone and the soil in the first cycles, followed by the creation of a gap during upward movement between the crushed soil adhered to the tip and the non-crushed soil which, by suction non-crushed soil is moved into the empty space and is crushed in the next cycles. (Idea based from Galvis-Castro et al., 2023).

The negative sleeve friction developed around the cone during the second cyclic loading at 1Hz, might have been caused by the clayey soil transformed as a result of particle crushing or due to the friction sleeve moving from the rod due to large forces acting on the sleeve, fact that can record negative values. This could be caused by the plasticity of the soil around the sleeve. Nonetheless, as the loading continues, the f_s increases and reaches values higher than the initial ones.

With respect to the similar circular shape of the crushed soil at the tip of the piles after Test 2 and Test 3, compared to the first test, similar breakage mechanisms could be expected. However, the compression force acting on the crushed soil during jacking was kept constant, in comparison to the impact hammering. This lead to larger compression forces at the tip of the pile. In Figure 6.33, an illustration representing the crushing mechanism during these methods is shown.

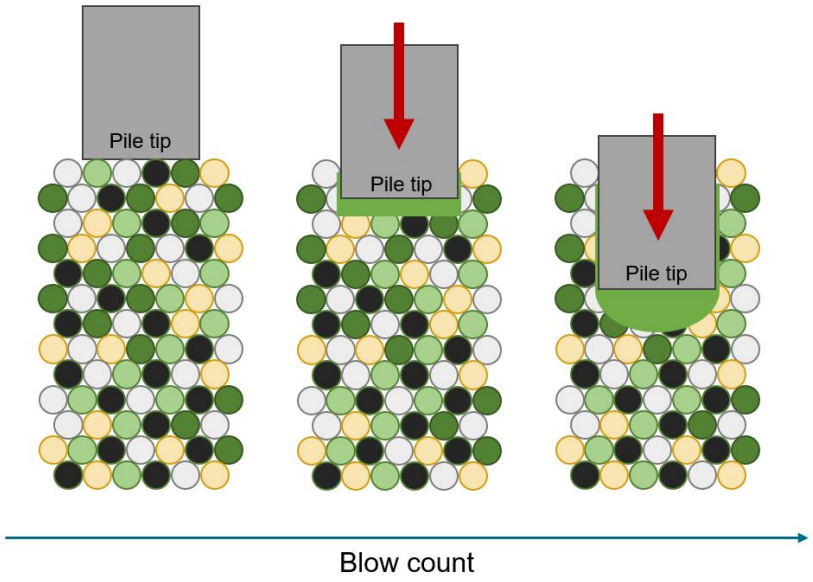


Figure 6.33: Hypothesis of the crushing mechanism during impact hammering and jacking: the crushing occurs outwards within the shear zone between the crushed soil and non-crushed soil. Under the base of the pile little crushing occurs. (Idea based from Mao et al., 2020)

Eventually, from the exhumation of the soil around the pile and the cone, difference was noticed between cyclic and static CPTu in Test 3. In the latter, although there was a larger size of crushed soil at the tip of the cone compared to the shaft, there was no bulb created (as observed by Bellotti et al., 1991). Besides, in all the tests crushed soil was also observed around the shaft, which was a result of the displacement of the soil below the tip, and the observed constant shaft thickness indicates that the crushing was occurring at the tip (also suggested by Galvis-Castro et al., 2019 and supported by Ciantia et al., 2019). Moreover, an increase in plasticity compared to the soil used for sample preparation was noticed, as observed by Westgate, Beemer, et al., 2023, Van Raak, 2009, Van Alboom et al., 2012, De Nijs et al., 2015.

Chapter 7

Conclusions and recommendations

7.1. Conclusions

This research focused on performing tests aiming at a better understanding of the mechanical behaviour of glauconitic sand during pile installation in a calibration chamber. To do so, first, the possibility of a large-scale sample preparation with a glauconitic sand containing a large amount of fines, received from a natural deposit in Antwerp, Belgium, had to be studied.

Due to the high sensitivity of the glauconite granules to sample preparation methods and the scale of the sample to be prepared, it was very challenging to come up with a final sample preparation to perform the tests. Moreover, the amount of fines and the interaction with the water leading to liquefaction lead to the final decision of removing the fine fraction of the as-received soil. Magnetic separation test results showed similar glauconite contents between as-received and sand fraction of the soil highlighting the fact that the bulk of glauconite granules were kept. Washing out the fines allowed the obtention of a homogeneous glauconitic sand for subsequently pluviate it under the water and compact it. From local density measurements after performing all the tests, the validity in obtaining dense saturated glauconitic soil samples (relative density approximately of 60-80%) was confirmed. Additionally, the constant values of bulk densities over depth indicated good repeatability of samples. This approach, therefore, allowed preparing repeatable and homogeneous samples under fully water saturated conditions. In all the calculations needed during the sample preparation, however, significant uncertainties were induced, due to the challenging determination of geotechnical parameters resulting from the non-homogeneity of the soil, the susceptibility to crushing of the glauconite granules and the moist retention capacity of the glauconite pellets.

After the sample preparation technique was clear and the tests could be performed, the soil response to cone penetration and pile installation in the calibration chamber was to be studied. During this research, three different tests could be conducted and, although they were all different, several conclusions can be made. Firstly, these tests proof the sample preparation achieved with this type of soil and the possibility to continue performing these same tests under the same boundary conditions but changing stress levels for further comparisons.

Regarding the results from the first test (CPTu), these were similar to a dense sand. The higher cone resistance obtained in the calibration chamber compared to the average q_c measured in the field (25MPa) could be attributed to the removal of fines and a denser sample prepared. Afterwards, under cyclic loading regimes, higher resistances were achieved. The large positive excess pore pressures in the static CPTu test indicated a change in drainage conditions from drained to partially undrained resulting from the crushing process leading to a transformation to a more clayey soil type. Concerning the cyclic loading, the immediate dissipation of the negative pore pressures as the cyclic loading stopped, indicated the silty-clayey behaviour from the crushed soil, which was in accordance to the PSD of the crushed soil.

Due to the change in boundary conditions between Test 2 and Test 3, the impact and jacking driving installation methods could not be compared. Also, the final penetration was different and there has been only one test performed for each method. Nonetheless, the soil pressure measurements registered increasing stresses with depth in both scenarios.

As observed from excavation of the soil after the tests, all the driving methods induced a certain level of particle crushing around the shaft and below the tip during installation. The exhumation of the soil around the instrumentation penetrated allowed the observation of the change in color of the crushed soil and the differences between the bulb tip using different methods. The particle breakage observed depended on the maturity of the pellets, therefore, on its composition. In this research, this is the case of nascent pellets. The particle size analysis of the crushed soil showed a significant increase in fines content, whose texture could also be noticed with the naked eye and from the observations in the microscope, it could be observed that mainly the glauconite pellets were crushed or partially crushed, in comparison to other minerals.

To finish, highlight the importance of laboratory testing emphasising the difficulties in carrying out an investigation of this scale for the first time and the difficulties to replicate the same conditions from the field to the laboratory since in laboratory testing, the in-place-behaviour of the glauconite sand is not captured. Hence, several recommendations for future research are discussed in the following section 7.2.

7.2. Recommendations

During this research only the sand fraction of the as-received soil was tested, removing the fine fraction including clay particles from crushed glauconitic sand. This could have lead to a more clayey soil after crushing, instead of silty size. However, this also depended on the resistance to crushing and Mohs hardness of the other minerals that composed the sand. In addition to this, only three different tests were performed. Therefore, further testing is needed to properly understand the mechanical behaviour of the sand fraction of the as-received soil, e.g. atterberg limits in the crushed soil, triaxial tests, oedometers, permeability.
Regarding the sample preparation procedure with the idealised soil, it allowed obtaining good-quality results and it is a recommendation to follow the same sample preparation for further tests using this soil. In addition to this, the non-disturbed soil from previous sample preparations can be reused. Nonetheless, it is also recommended to investigate the behaviour of the material containing fines. In this case, if the as-received soil containing all the fines wants to be tested, one solution could be moisturizing the soil, pouring it slowly in the cylinder and tampering it constantly, trying to avoid layering to occur. Afterwards, increase the water level of the cylinder from the bottom very slowly, ensuring there is no separation of layers and the compaction is kept. The 100 % saturation, however, would not be ensured.

In the last test, due to the large resistance of the soil the pile bended, therefore, a new model pile should be designed to continue performing tests in the calibration chamber. Moreover, the PPTs recordings showed a strong correlation between the force applied and displacement of the cone and pile, affecting the results by the mechanical deformations of the membrane of the PPTs. Therefore, recommendations for the new model pile design could be adding pore pressure transducers inside the pile to be able to measure horizontal pore pressures or redesigning the PPTs configuration.

To finish, the first steps into the calibration chamber explained in this report are also aimed to advise future researchers on the sample preparation and test procedures for testing glauconitic sand samples in large-scale samples in the future.

References

Adriaens, R., Vandenberghe, N., & Elsen, J. (2014). Natural Clay-Sized Glauconite in the Neogene Deposits of the Campine Basin (Belgium). *Clays and Clay Minerals*, *62*(1), 35–52. https://doi.org/10.1346/CCMN.2014.0620104

Alm, T., & Hamre, L. (2001). *Soil model for pile driveability predictions based on CPT interpretations* (tech. rep.).

API. (1993). *Recommended practice for planning, designing and constructing fixed offshore platforms.* American Petroleum Institute.

ASTM. (2007). D422-63 (2007) Standard Test Method for Particle-Size Analysis of Soils.

ASTM. (2016a). D4253-16e1 Standard Test Methods for Maximum Index Density and Unit Weight of Soils Using a Vibratory Table.

ASTM. (2016b). D4254-16 Standard Test Methods for Minimum Index Density and Unit Weight of Soils and Calculation of Relative Density.

Banerjee, S., Bansal, U., & Vilas Thorat, A. (2016). A review on palaeogeographic implications and temporal variation in glaucony composition. *Journal of Palaeogeography*, *5*(1), 43–71. https://doi.org/10.1016/j.jop.2015.12.001

Banerjee, S., Choudhury, T. R., Saraswati, P. K., & Khanolkar, S. (2020). The formation of authigenic deposits during Paleogene warm climatic intervals: a review. *Journal of Palaeogeography*, *9*(1), 27. https://doi.org/10.1186/s42501-020-00076-8

Bellotti, R., Fretti, C., Ghionna, V., & Pedroni, S. (1991). Compressibility and crushability of sands at high stresses. *roceedings of the First International Symposium on Calibration Chamber Testing*, 79–90.

Bond, A. J., & Jardine, R. J. (1991). Effects of installing displacement piles in a high OCR clay. *Géotechnique*, *41*(3), 341–363. https://doi.org/10.1680/geot.1991.41.3.341

Ciantia, M., O'Sullivan, C., & Jardine, R. (2019). Pile penetration in crushable soils: Insights from micromechanical modelling. *Proceedings of the XVII European Conference on Soil Mechanics and Geotehnical Engineering. Geotechnical Engineering foundation of the future*.

De Beer, E. (1974). Decrease in Penetration Resistance due to Excavation in an Overconsolidated Glauconitic Sand. *Proceedings of the European Symposium on Penetration Testing, 2:103-104*.

De Meuter, F., & Laga, P. (1976). Lithostratigraphy and biostratigraphy based on benthic foraminifera of the Neogene deposits of Northern Belgium. *Bulletin van de Belgische Vereniging voor Geologie*, *85/4*, 133–152.

De Nijs, R., Kaalberg, F., Osselaer, G., Couck, J., & van Royen, K. (2015). *"Full-scale field test (sheet) pile driveability in Antwerp", Geotechnical Engineering for Infrastructure and Development*. https://www.icevirtuallibrary.com/doi/abs/10.1680/ecsmge.60678.vol3.151

DeGroot, D., Westgate, Z., & Yetginer-Tjelta, T. (2023). Geological and geotechnical challenges of the East Coast United States for offshore energy transition.

Demars, K. (1982). *Geotechnical Properties, Behavior, and Performance of Calcareous Soils: A Symposium Sponsored by ASTM Committee D-18 on Soil and Rock, Ft. Lauderdale, Fla., 20 Jan. 1981* (K. Demars & R. C. Chaney, Eds.). American Society for Testing; Materials. https://books.google.nl/books?id=KWPKqsqWDmMC

Di Emidio, G., Verastegui Flores, R., & Van Impe, W. (2009). Crushability on granular materials by strain controlled oedometer testing at high stress levels. In M. Hamza, M. Shahien, & Y. El-Mossalbami (Eds.), *Proceedings of the 17th international conference on soil mechanics and geotechnical engineering : The academia and practice of geotechnical engineering* (pp. 127–130). https://doi.org/https://doi.org/10.3233/978-1-60750-031-5-127

Fellenius, B. H. (2015). Static tests on instrumented piles affected by residual load. *DFI Journal - The Journal of the Deep Foundations Institute*, *9*(1), 11–20. https://doi.org/10.1179/1937525515Y.0000000001

Fernández-Landero, S., & Fernández-Caliani, J. C. (2021). Mineralogical and Crystal-Chemical Constraints on the Glauconite-Forming Process in Neogene Sediments of the Lower Guadalquivir Basin (SW Spain). *Minerals*, *11*(6), 578. https://doi.org/10.3390/min11060578

Galvis-Castro, A. C., Tovar-Valencia, R. D., Salgado, R., & Prezzi, M. (2019). Effect of loading direction on the shaft resistance of jacked piles in dense sand. *Géotechnique*, *69*(1), 16–28. https://doi.org/10.1680/jgeot.17.P.046

Galvis-Castro, A. C., Tovar-Valencia, R. D., Prezzi, M., & Salgado, R. (2023). Effect of cyclic loading on the mobilization of unit base resistance of model piles jacked in sand. *Acta Geotechnica*, *18*(9), 4747–4766. https://doi.org/10.1007/s11440-023-01840-5

Giresse, P., Lamboy, M., & Odin, G. (1980). Évolution géométrique des supports de glauconitisation; application à la reconstitution du paléoenvironnement. *Oceanol. Acta*, 251–260.

Gourvenec, S. (2023a). Numerical modelling in geotechnical design of offshore infrastructure - Evolution and Revolution. *Proc. 10th European Conference on Numerical Methods in Geotechnical Engineering*. https://doi.org/10.53243/NUMGE2023-433

Gourvenec, S. (2023b). Offshore geotechnical challenges of the energy transition. *Symposium on Energy Geotechnics 2023*, 1–2. https://doi.org/10.59490/seg.2023.623

GWEC. (2023). *Global Wind Report 2023* (tech. rep.). Global Wind Energy Council.

Heerema, E. P. (1978). Predicting Pile Driveability: Heather As An Illustration Of The ”Friction Fatigue” Theory. *All Days*. https://doi.org/10.2118/8084-MS

Hesselbo, S. P., & Huggett, J. M. (2001). Glaucony in Ocean-Margin Sequence Stratigraphy (Oligocene-Pliocene, Offshore New Jersey, U.S.A.; ODP Leg 174A). *Journal of Sedimentary Research*, *71*(4), 599–607. https://doi.org/10.1306/112800710599

Hölscher, P., van Tol, A., & Huy, N. (2012). Rapid pile load tests in the geotechnical centrifuge. *Soils and Foundations*, *52*(6), 1102–1117. https://doi.org/10.1016/j.sandf.2012.11.024

Huggett, J. (2013). Minerals: Glauconites and Green Clays. In *Reference module in earth systems and environmental sciences*. Elsevier. https://doi.org/10.1016/B978-0-12-409548-9.02893-1

IRENA & GWEC. (2021). *A next Decade Action Agenda to ad-vance SDG7 on sustainable energy for all, in line with the goals of the Paris Agreement on Climate Change* (tech. rep.).

Jamiolkowski, M., Ladd, C., Germaine, J., & Lancellotta, R. (1985). New developments in field and laboratory testing of soils. *Proceedings, 11th International Conference on Soil Mechanics and Foundation Engineering*, 578–154.

Joustra, K., & De Gijt, J. (1982). Results and interpretation of cone penetration tests in soil of different mineralogic composition.

Lamboy, M., & Odin, G. (1975). Nouveaux aspects concernant les glauconies du plateau continental Nord-Ouest espagnol. *Rev. Géogr. phys. Géol. dyn.*, *17*, 99–120.

Long, X., Tucker, G., Gibbs, P., Westgate, Z., Diaz, A. T., & Senanayake, A. (2019). Soil Classification and Evaluation of Preconsolidation Stress of Atlantic Outer Continental Shelf OCS Sediments from Oedometer and Cone Penetration Testing. *Offshore Technology Conference*. https://doi.org/10.4043/29541-MS

López-Quirós, A., Sánchez-Navas, A., Nieto, F., & Escutia, C. (2020). New insights into the nature of glauconite. *American Mineralogist*, *105*(5), 674–686. https://doi.org/10.2138/am-2020-7341

Mao, W., Hamaguchi, H., & Koseki, J. (2020). Discrimination of Particle Breakage below Pile Tip after Model Pile Penetration in Sand Using Image Analysis. *International Journal of Geomechanics*, *20*(1). https://doi.org/10.1061/(ASCE)GM.1943-5622.0001535

Mitchell J.K, Chatoian, J., & Carpenter, G. (1976). *The Influences of Sand Fabric in Liquefaction Behaviour Report* (tech. rep.). U.S.Army Engineer waterways Experiment Station, University of California. Berkeley.

Mulilis, J., Chan, C., & Seed, H. (1975). *The Effects of Method of Sample Preparations on the Cyclic Stress-Strain Behaviour of Sands* (tech. rep.).

Obasi, C. C., Terry, D. O., Myer, G. H., & Grandstaff, D. E. (2011). Glauconite Composition and Morphology, Shocked Quartz, and the Origin of the Cretaceous(?) Main Fossiliferous Layer (MFL) in Southern New Jersey, U.S.A. *Journal of Sedimentary Research*, *81*(7), 479–494. https://doi.org/10.2110/jsr.2011.42

Odin, G. S., & Matter, A. (1981). De glauconiarum origine. *Sedimentology*, *28*(5), 611–641. https://doi.org/10.1111/j.1365-3091.1981.tb01925.x

Odin, G., & Dodson, M. (1982). Zero isotopic age of glauconites.

Osborne Hutton, C., & Seelye, F. (1941). Composition and properties of some New Zealand Glauconites. *26*, 595–604.

Perikleous, G., Meissl, S., Troya Diaz, A., Stergiou, T., & Ridgway-Hill, A. (2023). Monopile installation in glauconitic sands. *9th International Offshore Site Investigation and Geotechnics (OSIG):Innovative Getechnologies for Energy Transition*, 132–138.

Poel, J., & Schenkeveld, F. (1998). A preparation technique for very homogeneous sand models and CPT research. In Kimura & Kusakabe (Eds.), *Proceedings of the international conference centrifuge 98* (pp. 149–154).

Randolph, M., & Gourvenec, S. (2011). Piled foundations. In *Offshore geotechnical engineering* (pp. 145–235). Taylor; Francis.

Rietdijk, J., Schenkeveld, F., Schaminee, P., & Bezuijen, A. (2010). The drizzle method for sand sample preparation. In *Physical modelling in geotechnics* (pp. 267–272).

Robertson, P. (2016). Cone penetration test (CPT)-based soil behaviour type (SBT) classification system — an update. *Canadian Geotechnical Journal*, *53*(12), 1910–1927. https://doi.org/10.1139/cgj-2016-0044

Skempton, A. (1951). The Bearing Capacity of Clays. *Building Research Congress*, 180–189.

Tedrow, J. (2002). *Greensand and Greensand Soils of New Jersey: A Review* (tech. rep.). Department of Ecology, Evolution and Natural Resources Rutgers University, New Brunswick, NJ 08901.

Thi Viet Phuong, N. (2019). *Numerical Modelling Of Pile Installation Using Material Point Method* (Doctoral dissertation). Delft University of Technology (TU Delft). Delft.

Thompson, G. R. (1975). The Mineralogy of Glauconite. *Clays and Clay Minerals*, *23*(4), 289–300. https://doi.org/10.1346/CCMN.1975.0230405

Van Alboom, G., Maertens, J., Dupont, H., & Haelterma, K. (2012). Glauconite Holding Sands. *Geotechnique*, 32–37.

Van Raak, R. (2009). Geotechnical Properties of Glauconite Sands.

Ventouras, K., & Coop, M. (2009). On the behaviour of Thanet Sand: an example of an uncemented natural sand. *Géotechnique*, *59*(9), 727–738. https://doi.org/10.1680/geot.7.00061

Westgate, Z. J., Beemer, R. D., & DeGroot, D. J. (2023). Implications of glauconite sands on US offshore wind development.

Westgate, Z. J., DeGroot, D. J., McMullin, C., Zou, Y., Guo, D., Van Haren, S., Beemer, R. D., Zeppilli, D., Miller, K. G., & Browning, J. V. (2023). Effect of degradation on geotechnical behavior of glauconite sands from the U.S. Mid-Atlantic Coastal Plain. *Ocean Engineering*, *283*, 115081. https://doi.org/10.1016/j.oceaneng.2023.115081

Westgate, Z. J., McMullin, C., & DeGroot, D. (2022). Glauconite Sand Challenges for US Offshore Wind Development. *Proceedings of the ASME 2022 4th International Offshore Wind Technical Conference. ASME 2022 4th International Offshore Wind Technical Conference. Boston, Massachusetts, USA. December 7–8*. https://doi.org/https://doi.org/10.1115/IOWTC2022-98666

Westgate, Z. J., McMullin, C., Zeppilli, D., Beemer, R., & DeGroot, D. J. (2022). Geological and Geotechnical Characteristics of Glauconitic Sands. *Geo-Congress 2022: Site and Soil Characterization, Computational Geotechnics, Risk, and Lessons Learned.* https://doi.org/https://doi.org/10.1061/9780784484036.012

White, D. (2005). A general framework for shaft resistance on displacement piles in sand. *First International Symposium on Frontiers in Offshore Geotechnics*, 697–703.

Yoon, Y.-W., & Van Impe, W. (1991). *Static and Dynamic Behavior of Crushable and Non-crushable Sands : Validation of Stress-dilatancy Theory.* (Doctoral dissertation). Ghent University.

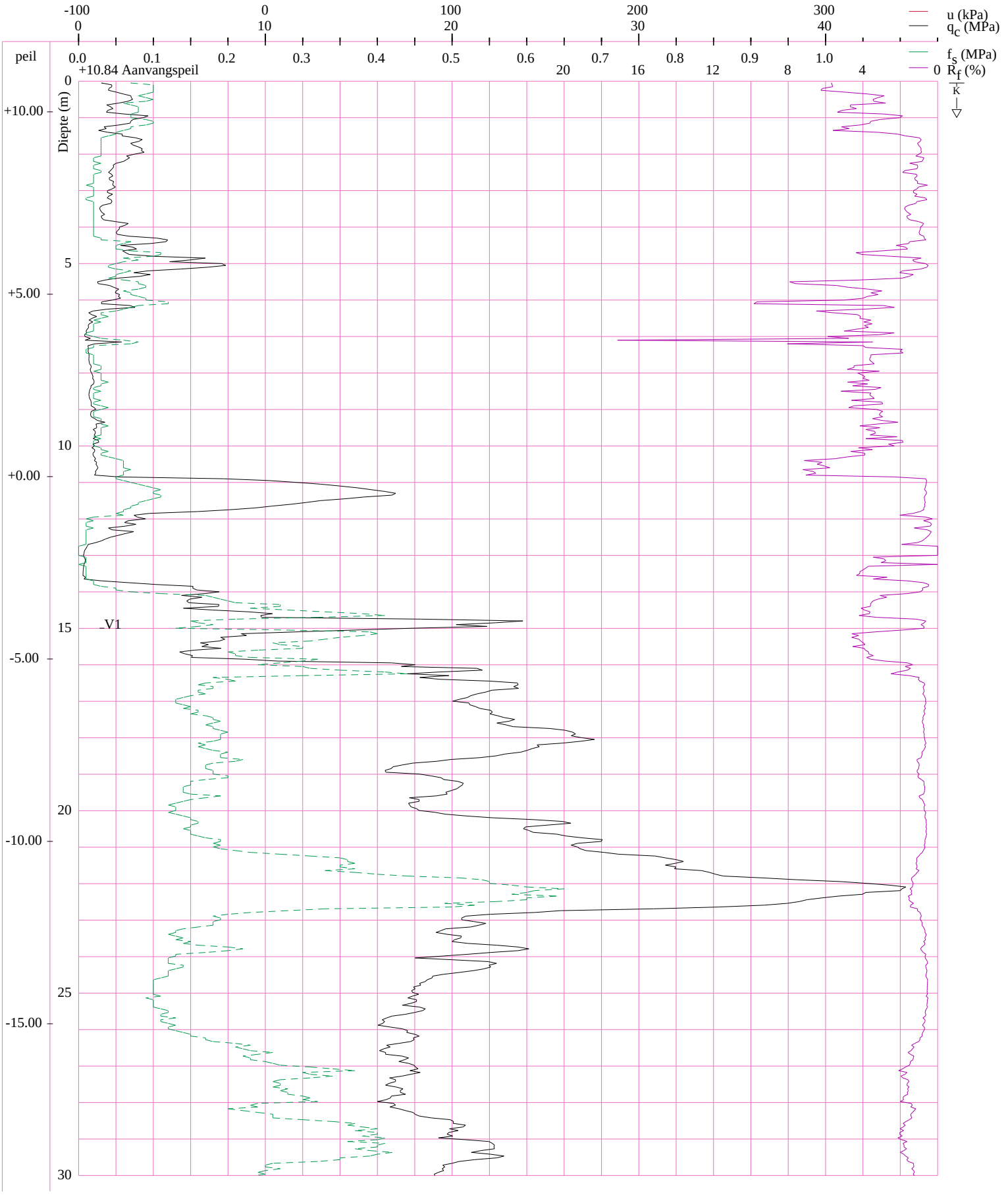
Appendix A

Site investigation data

Vlaanderen
is ondergrond

Sondering

Proefnummer:	GEO-04/157-SP-S2	Aanvangsdatum:	28/09/2004	Norm:	
X(Lambert):	150645.70	Sondeerapparaat:	200 kN - TRACK-TRUCK		
Y(Lambert):	214584.20	Conus:	U	Uitvoeringsmethode:	continu elektrisch
Z (mTAW):	+10.84	Lengte (m):	0.05 tot 34.00		
Gemeente:	Antwerpen	Sondeergat dicht op :	3.30 m(peil +7.54)		
Uitvoerder:	MVG - Afdeling Geotechniek				

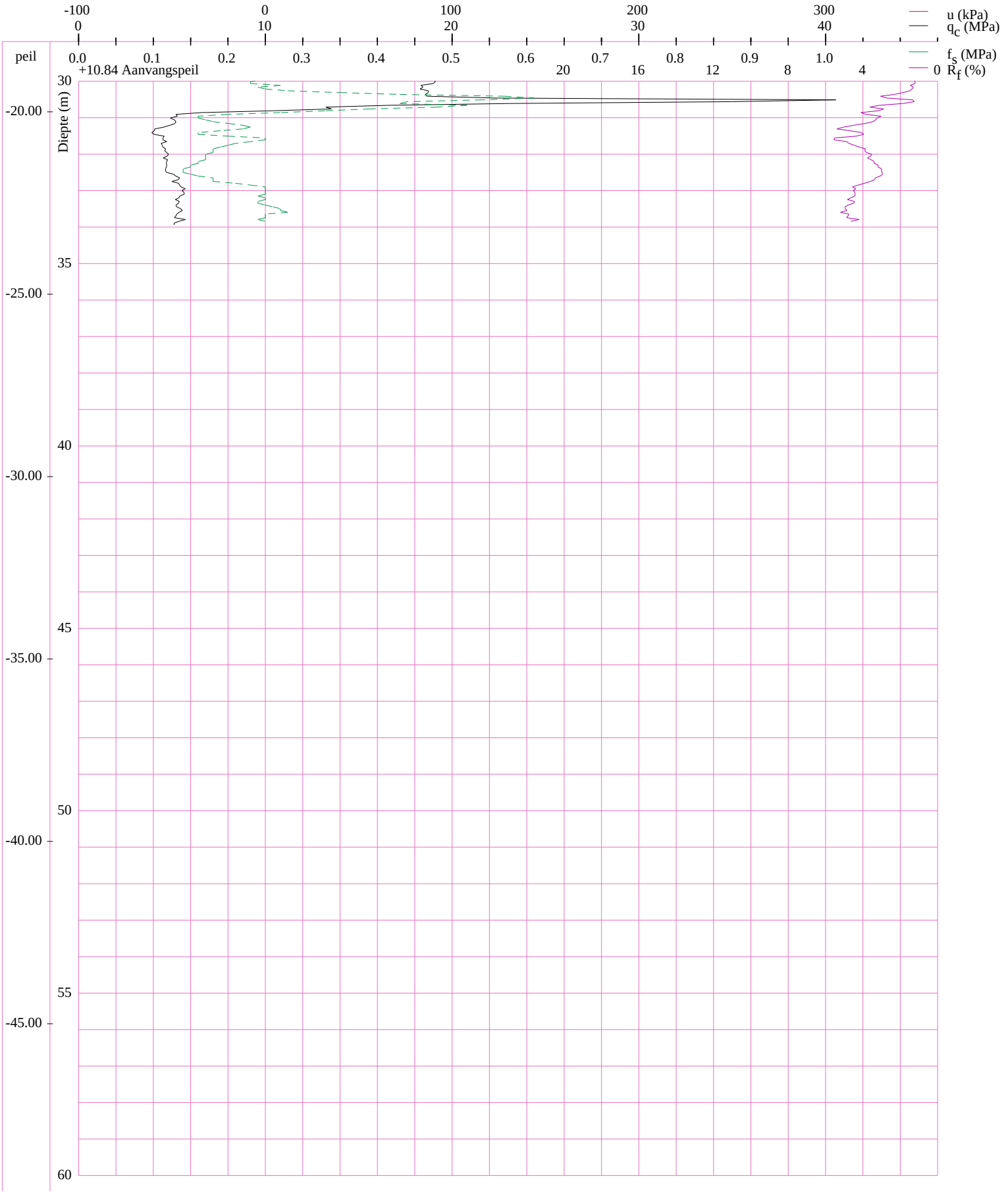


De gegevens worden enkel meegedeeld ter informatie. Het Vlaams Gewest kan niet aansprakelijk worden gesteld voor de gevolgen van welk gebruik dan ook.

Vlaanderen
is ondergrond

Sondering

Proefnummer:	GEO-04/157-SP-S2	Aanvangsdatum:	28/09/2004	Norm:	
X(Lambert):	150645.70	Sondeerapparaat:	200 kN - TRACK-TRUCK		
Y(Lambert):	214584.20	Conus:	U	Uitvoeringsmethode:	continu elektrisch
Z (mTAW):	+10.84	Lengte (m):	0.05 tot 34.00		
Gemeente:	Antwerpen	Sondeergat dicht op :	3.30 m(peil +7.54)		
Uitvoerder:	MVG - Afdeling Geotechniek				



De gegevens worden enkel meegedeeld ter informatie. Het Vlaams Gewest kan niet aansprakelijk worden gesteld voor de gevolgen van welk gebruik dan ook.

Sondering

Algemene gegevens

Opdrachtnummer:	GEO-04/157
Proefnummer:	**GEO-04/157-SP-S2**
Datum uitvoering:	28/09/2004
Norm:	
Plaats:	
Lambertcoordinaten:	X=150645.7 - Y=214584.2
XY afkomstig van:	MVG - Afdeling Wegen Antwerpen
XY bepaald volgens:	XY_topografisch ingemeten
Aanvangspeil (mTAW):	10.84
Aanvangspeil afkomstig van:	MVG - Afdeling Wegen Antwerpen
Aanvangspeil bepaald volgens:	Z_topografisch ingemeten
Huidig maaiveld (DHMVII) (mTAW):	10.64
Uitvoeringsmethode:	continu elektrisch
Apparaat Type:	200 kN - TRACK-TRUCK
Conus Type:	U
Conus serienummer:	
Conus calibratiedatum:	
Meetlichaam:	CFIP
Operator:	De Bruyn, Chris
Grondsoort aan de conus:	
Diepte* water:	Geen opmeting waterpeil
Datum opmeting waterpeil:	28/09/2004 12:40
Diepte* put:	
Sondeergat dichtgevallen op*:	3.30 m (tov het aanvangspeil)
Diepte* plaatsen kleefvanger:	0.05 m (tov het aanvangspeil)
Aantal buizen:	0
Opgemeten lengte:	
Uitgevoerd door:	MVG - Afdeling Geotechniek
Totale drukkracht bij einde sondering (kPa):	
Stopcriterium:	niet nader gespecificeerd
Opvullen van sondeergat:	

(* : diepte werd niet gecorrigeerd met helling van de sondeerstang)

Formele stratigrafie - 22/04/2005

Auteur(s): Van Orsmael, Joseph (MVG - Afdeling Natuurlijke Rijkdommen en Energie) Betrouwbaarheid: goed

Opmerking: De dieptes van de Formele Stratigrafie zijn bepaald t.o.v. de sondeerlengte. Meer informatie hierover op de documentatie pagina: https://www.milieuinfo.be/confluence/x/jKn8C.

Van(m)	Tot(m)	Beschrijving	Betrouwbaarheid
0.00	10.70	Q - Groep van Quartaire afzetting	goed
10.70	31.00	Li - Formatie van Lillo tot Bc - Formatie van Berchem	goed
31.00	34.00	Bm - Formatie van Boom	goed

De gegevens worden enkel meegedeeld ter informatie. Het Vlaams Gewest kan niet aansprakelijk worden gesteld voor de gevolgen van welk gebruik dan ook.

Appendix B

Geotechnical characterisation

B.1. Particle size distribution (PSD) analysis

The grain-size analyses were performed using two different methods: (1) laser diffraction and (2) traditional sieving using a mixer. The former used the particle size analyzer Malvern Mastersizer 3000 to obtain the particle size measurements using a wet dispersion method of sample dispersion for laser diffraction of the sample. The results showed the decrease in particle size occurring during dispersion. This method is very suitable for samples containing very fine particles. The latter, followed the traditional sieving method according to standard ASTM D422 (ASTM, 2007) in which the soil was sieved through a series of sieves ordered from larger to smaller mesh sizes (see Table B.1) in order to separate the particles by size while vibration was applied during a specific time (in this case, 15 minutes) (Figure B.1). Eventually, the percentage of material that passed through each sieve was measured and the PSD curve could be obtained.



Figure B.1: Series of sieves used for performing the test on top of the mixer.

Opening sieve
4 mm
2 mm
1,6 mm
1 mm
850 μm
500 μm
425 μm
250 μm
150 μm
106 μm
75 μm
63 μm
Pan

Table B.1: Openings of the sieves used according to ASTM (2007) with extra sieves.

B.2. Specific gravity, G_s

To measure the specific gravity (G_s) of the glauconitic sand, the Gas Pycnometer type Ultrapyc 5000 was used in the Geoscience and Engineering Laboratory at TUDelft (Figure B.2a). Firstly, 5 samples of as-received soil were tested. Since each of the results were obtained after a 5 times iteration proccess and they showed little variation, it was decided to test 3 samples of the sand fraction of the glauconitic soil after removal of fines. All the samples used for the tests were oven-dried to 77ºC prior to testing. Moreover, it should be highlighted that the as-received samples 1 and 2 were firstly sieved using the 1mm sieve and samples 3 and 4 using the 2mm sieve in order to remove the larger particles such as shells or clumps and to have a more homogeneous soil sample (Figure 4.1b and Figure 4.1c). Sample

5 was not pre-sieved. All the measurements obtained are showed in the following Table B.2 and Table B.3.



(a)



(b)



(c)

Figure B.2: a) Setup for the measurement of G_s. From oven-dried as-received soil, material retained in b) sieve with opening 1mm from sample 1; c) sieve with opening 2mm from sample 3.

Sample	Bag	Sieved	Sample weight [g]	G_s [g/cm^3]	$G_{s,average}$ [g/cm^3]
1	B3	Yes: 2mm opening	105,507	2,8692 2,8604 2,8538 2,8496 2,8458	2,85576
2	B4	Yes: 2mm opening	117,080	2,7021 2,6990 2,6979 2,6952 2,6958	2,6963
3	B5	Yes: 1mm opening	109,976	2,6985 2,6961 2,6950 - -	2,6965
4	B6	Yes: 1mm opening	112,399	2,6965 2,6939 2,6937 - -	2,6947
5	B7	No	128,811	2,6933 2,6940 2,6925 - -	2,693

Table B.2: G_s measurements in pycnometer from as-received soil.

Sample	Sample weight [g]	G_s [g/cm^3]	$G_{s,average}$ [g/cm^3]
1	138,567	2,6727 2,6696 2,6678	2,670
2	132,392	2,6664 2,6653 2,6648	2,666
3	132,491	2,6603 2,6589 2,6597	2,660

Table B.3: G_s measurements in pycnometer from sand fraction of glauconitic sand after removal of fines.

B.3. Maximum and minimum density

The maximum and minimum density tests were performed with the as-received soil and the sand fraction of the glauconitic sand after removal of fines using the dry method. However, since the soil used for preparing the samples in the calibration chamber was moist and poured into water while being tampered, the wet method was also performed in the sand fraction of the glauconitic soil due to its similarity to the test conditions.

To perform these tests, a cylindrical mold of volume 531 cm^3 (V_s) and weight 476,7 g was used. The setup and equipment used is shown in Figure B.3.



Figure B.3: Equipment used for maximum and minimum density tests.

- **Dry method**

  For this method, the soil was oven-dried to 110ºC. The loosest state was achieved by pouring, first, the soil into the funnel until half-full. Afterwards, the funnel was pulled carefully upwards to try to keep a constant speed and, as a consequence, a constant flow of soil poured into the mold. To finish, the top surface was flattened with a ruler. To achieve the densest state, the mold was filled by layers with the soil with the help of a spoon. Each layer was densified by applying a weight on top while vibrating the mold with a vibratory instrument (see Figure B.4). The top of the surface was flattened with a ruler too.

- **Wet method**

  In this method, the soil was moist with a water content of 20% and mixed with sufficient water to achieve full saturation of the sample but not accumulation of free water in the mold. In this method, the mold was approximately 1/3 filled with water prior to be filled with soil. For the loosest state, the wet soil was slowly poured into the mold with a scoop and the top surface was flattened with a ruler. For the dense state, two methods were used. Firstly, the mold was kept vibrating during the whole process by placing it on top of a vibratory surface while the soil was poured inside with a scoop (see

Figure B.5). The top surface was also flattened with a ruler. The other method aimed to replicate the sample preparation used for densifying the soil in the calibration chamber. In this case, the moist soil was poured into the mold while it was being tampered. The results were not altered by the change of method, indicating similar densities.

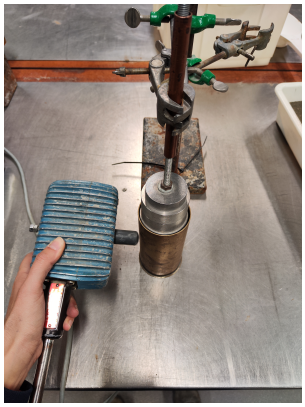


Figure B.4: Densification process for a layer, with a weight on top of the soil and the vibration applied on the walls of the mold.



Figure B.5: Mix of soil with water (left) and mold on top of vibratory surface used to densify sample (right).

To obtain the results for the minimum and maximum densities, the following formulation was followed:

- **Minimum density**

  The minimum dry density ($\rho_{d,min}$) and unit weight ($\gamma_{d,min}$) of each test specimen was calculated as follows:

$$\rho_{d,min} = \frac{M_s}{V_s} \tag{B.1}$$

$$\gamma_{d,min} = \rho_{d,min} \times g \tag{B.2}$$

Being:			
	$\rho_{d,min}$	Minimum density of the tested soil	[g/cm^3]
	$\gamma_{d,min}$	Minimum unit weight of the tested soil	[kN/m^3]
	M_s	Mass of the tested soil	[g]
	V_s	Volume of the tested soil	[cm^3]
	g	Acceleration of gravity equal to 9.81	[m/s^2]

  For the wet method, the soil filling the mold was oven-dried after the test in order to obtain the mass (M_s).

The corresponding maximum void ratio (e_{max}) and maximum porosity (n_{max}) for each test specimen was derived from the previous obtained values:

$$e_{max} = \left(\rho_w \times \frac{G_S}{\rho_{d,min}}\right) - 1 \quad \text{(B.3)}$$

$$n_{max} = 1 - \frac{\rho_{d,min}}{G_s} \quad \text{(B.4)}$$

Being:			
	e_{max}	Maximum void ratio of the tested soil	[-]
	n_{min}	Minimum porosity of the soil	[-]
	G_s	Average specific gravity of the soil	[g/cm^3]
	ρ_w	Density of water at 20ºC equal to 1	[g/cm^3]

- **Maximum density**

The maximum dry density ($\rho_{d,max}$) and unit weight ($\gamma_{d,max}$) of each test specimen was calculated as follows:

$$\rho_{d,max} = \frac{M_s}{V_s} \quad \text{(B.5)}$$

$$\gamma_{d,max} = \rho_{d,max} \times g \quad \text{(B.6)}$$

Being:			
	$\rho_{d,max}$	Maximum density of the tested soil	[g/cm^3]
	$\gamma_{d,max}$	Maximum unit weight of the tested soil	[kN/m^3]
	M_s	Mass of the tested soil	[g]
	V_s	Volume of the tested soil	[cm^3]
	g	Acceleration of gravity equal to 9.81	[m/s^2]

For the wet method, the soil filling the mold was oven-dried after the test in order to obtain the mass (M_s).

The corresponding minimum void ratio (e_{min}) and minimum porosity (n_{min}) for each test specimen was derived from the previous obtained values:

$$e_{min} = \left(\rho_w \times \frac{G_S}{\rho_{d,max}}\right) - 1 \quad \text{(B.7)}$$

$$n_{min} = 1 - \frac{\rho_{d,max}}{G_s} \quad \text{(B.8)}$$

Being:			
	e_{max}	Maximum void ratio of the tested soil	[-]
	n_{max}	Maximum porosity of the soil	[-]
	G_s	Average specific gravity of the soil	[g/cm^3]
	ρ_w	Density of water at 20ºC equal to 1	[g/cm^3]

In the following Table B.4 the results obtained in the tests are shown. These values are the average of each of the tests, which were performed 3 times.

		Dry		Wet
Parameter		**As-received**	**Sand fraction**	
Maximum dry density ($\rho_{d,max}$)	[g/cm³]	1,33	1,58	1,66
Minimum dry density ($\rho_{d,min}$)	[g/cm³]	1,06	1,33	1,48
Maximum unit weight ($\gamma_{d,max}$)	[kN/m³]	13,08	15,54	16,24
Minimum unit weight ($\gamma_{d,min}$)	[kN/m³]	10,39	13,04	14,55
Maximum porosity (n_{max})	[-]	0,61	0,50	0,44
Minimum porosity (n_{min})	[-]	0,51	0,41	0,38
Maximum void ratio (e_{max})	[-]	1,55	1,00	0,80
Minimum void ratio (e_{min})	[-]	1,03	0,68	0,61

Table B.4: Summary of the measurements obtained from the maximum and minimum density tests.

		Sample 1	Sample 2	Sample 3	Sample 4
Volume cylinder	**[cm³]**	531,00	531,00	531,00	531,00
Soil added (loose state)	**[g]**	563,10	567,80	538,50	579,4
Soil added (dense state)	**[g]**	714,30	714,70	701,60	701,60
Minimum dry density ($\rho_{d,min}$)	**[g/cm³]**	1,06	1,07	1,01	1,09
Maximum dry density ($\rho_{d,max}$)	**[g/cm³]**	1,35	1,35	1,32	1,32
Specific gravity (G_s)	**[-]**	2,70	2,70	2,70	2,70
Maximum porosity (n_{max})	**[-]**	0,61	0,60	0,62	0,60
Minimum porosity (n_{min})	**[-]**	0,50	0,50	0,51	0,51
Maximum void ratio (e_{max})	**[-]**	1,55	1,53	1,66	1,47
Minimum void ratio (e_{min})	**[-]**	1,01	1,01	1,04	1,04
Minimum unit weight, (γ_{min})	**[kN/m³]**	10,40	10,49	9,95	10,70
Maximum unit weight, (γ_{max})	**[kN/m³]**	13,20	13,20	12,96	12,96

Table B.5: Measurements from maximum and minimum density tests from as-received soil using dry method.

		Sample 1	Sample 2	Sample 3
Volume cylinder	**[cm³]**	531,00	531,00	531,00
Soil added (loose state)	**[g]**	707,30	703,00	708,00
Soil added (dense state)	**[g]**	849,5	837,6	836,10
Minimum dry density ($\rho_{d,min}$)	**[g/cm³]**	1,33	1,32	1,33
Maximum dry density ($\rho_{d,max}$)	**[g/cm³]**	1,60	1,58	1,57
Specific gravity (G_s)	**[-]**	2,67	2,67	2,67
Maximum porosity (n_{max})	**[-]**	0,50	0,50	0,50
Minimum porosity (n_{min})	**[-]**	0,40	0,41	0,41
Maximum void ratio (e_{max})	**[-]**	1,00	1,01	1,00
Minimum void ratio (e_{min})	**[-]**	0,67	0,69	0,69
Minimum unit weight, (γ_{min})	**[kN/m³]**	13,07	12,99	13,08
Maximum unit weight, (γ_{max})	**[kN/m³]**	15,69	15,47	15,45

Table B.6: Measurements from maximum and minimum density tests from the sand fraction of the glauconitic sand after removal of fines using dry method.

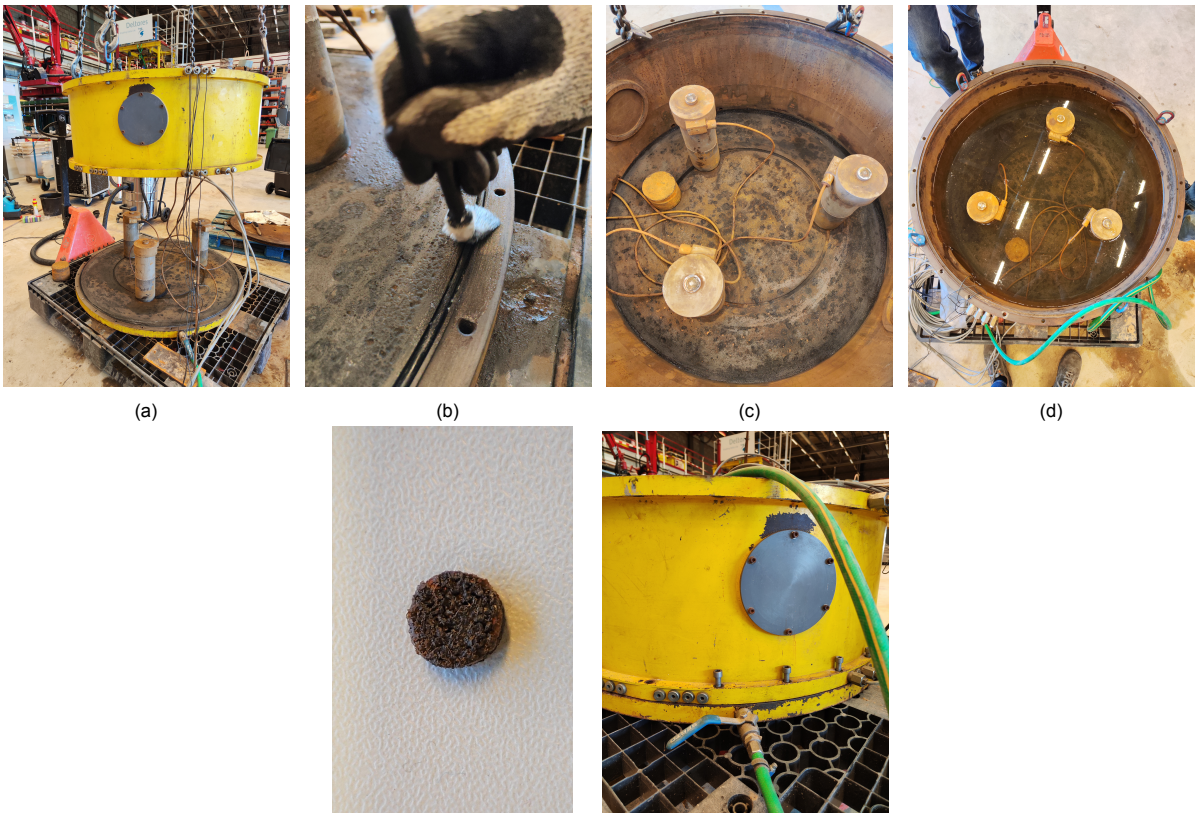
		Sample 1	Sample 2	Sample 3
Volume cylinder	**[cm^3]**	531,00	531,00	531,00
Soil added (loose state)	**[g]**	805,6	777,6	779,9
Soil added (dense state)	**[g]**	885,8	883,2	868,4
Minimum dry density ($\rho_{d,min}$)	**[g/cm^3]**	1,52	1,46	1,47
Maximum dry density ($\rho_{d,max}$)	**[g/cm^3]**	1,67	1,66	1,64
Specific gravity (G_s)	**[-]**	2,67	2,67	2,67
Maximum porosity (n_{max})	**[-]**	0,43	0,45	0,45
Minimum porosity (n_{min})	**[-]**	0,37	0,38	0,39
Maximum void ratio (e_{max})	**[-]**	0,76	0,82	0.81
Minimum void ratio (e_{min})	**[-]**	0,60	0,60	0,63
Minimum unit weight, (γ_{min})	**[kN/m^3]**	14,88	14,37	14,41
Maximum unit weight, (γ_{max})	**[kN/m^3]**	16,36	16,32	16,04

Table B.7: Measurements from maximum and minimum density tests from the sand fraction of the glauconitic sand after removal of fines using wet method.

Appendix C

Calibration chamber setup

C.1. Bottom ring



(a) (b) (c) (d)

(e) (f)

Figure C.1: a) Opened bottom ring to show assembly. b) Placement in the groove the O-ring brushed with vaseline to ensure good attachment with the walls. c) Closed bottom ring with three load cells and weight on top of porous stone to avoid leakage of the system. d) Bottom ring checked for watertightness and fully prepared. e) Porous stone. f) Valve to allow drainage at the bottom of the ring.



(a) (b) (c) (d)

Figure C.2: a) Self-expanding material glued to the edge of the plate. b) Material expanded after applying heat to ensure the tightness of the plate and its position. c) Final position of the top plate of the bottom ring. d) Sealant applied to the top plate to ensure its position, allowing the cables to move.



(a) (b) (c) (d)

Figure C.3: a) Permeable porous filter to allow water flow preventing any grain to pass through it. b) Geotextile 2mm thick to allow water infiltration. c) Geotextile and filter plate with holes on top of the porous filter, screwed to stay in that position. d) Final set-up of the bottom ring.

C.2. Sensors

C.2.1. Pore pressure transducers



Figure C.4: Connection of the pore pressure transducers (top) and the load cells cables (bottom).

C.2.2. Pressure transducer of the membrane



(a) (b) (c)

Figure C.5: a) Opening for connecting cable to measure pressure (left) and opening to allow inlet of air or water (used to apply vacuum) (right). b) Connection of the pressure sensor to the computer (left) and vacuum applied (right). c) Inside of ring 3 with opening for applying vacuum (left) and pressure transducer (right).

C.3. Inner lining installation

C.3.1. Foam installation



(a) (b) (c) (d)

Figure C.6: a) PVC ring placed at the bottom of Ring 1 and at the top of Ring 4, to ensure position of foam. Afterwards sealed with sealant to keep them in place. b) Side view foam, thickness 2.5cm. c) Top PVC ring sealed with sealant to ensure its position and fixation of the foam around the inside walls of Rings 1 to 4 using sealant too. d) Final foam installation.

C.3.2. Membrane installation



(a) (b) (c) (d)



(e)

Figure C.7: a) 3mm thickness membrane before installation. b) Top of membrane clamped for easier installation. c) Clamped bottom of the membrane to avoid it slides, since also it cannot be screwed. d) Final position membrane (no vacuum applied). Visible wrinkles due to the space between the foam and the membrane. d) Final membrane installation after positioning Ring 5 on top.

C.4. Top plate

C.4.1. CPT and jacking

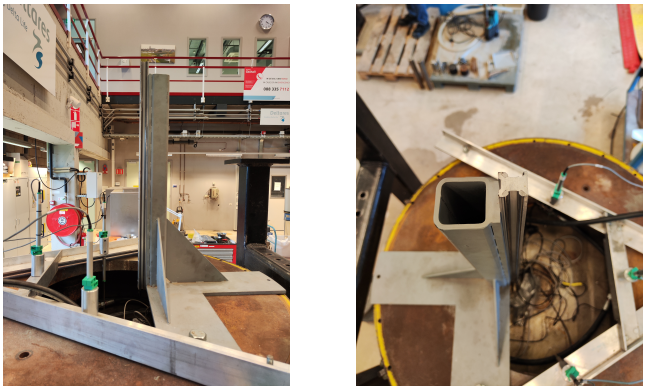


(a) (b) (c) (d)

(e) (f) (g) (h)

Figure C.8: a) Top ring with long bolts to fix membrane in place. b) Three layers of foam on top of the soil to ensure contact with top plate. c) Top plate with pressure distributor and hydraulic jacks. d) Shaped edge of the top plate to avoid contact with the membrane. e) Top plate with weights on top of the hydraulic jacks and rubber plates to make less stiff the displacement of the jacks. f) Highest plate with guiding for three potentiometric displacement sensors. g) Final installation of the potentiometric displacement sensors to determine the relative displacement of the top plate. h) Rollers to guide the pile during jacking installation and ensure its verticality.

C.4.2. Impact driving

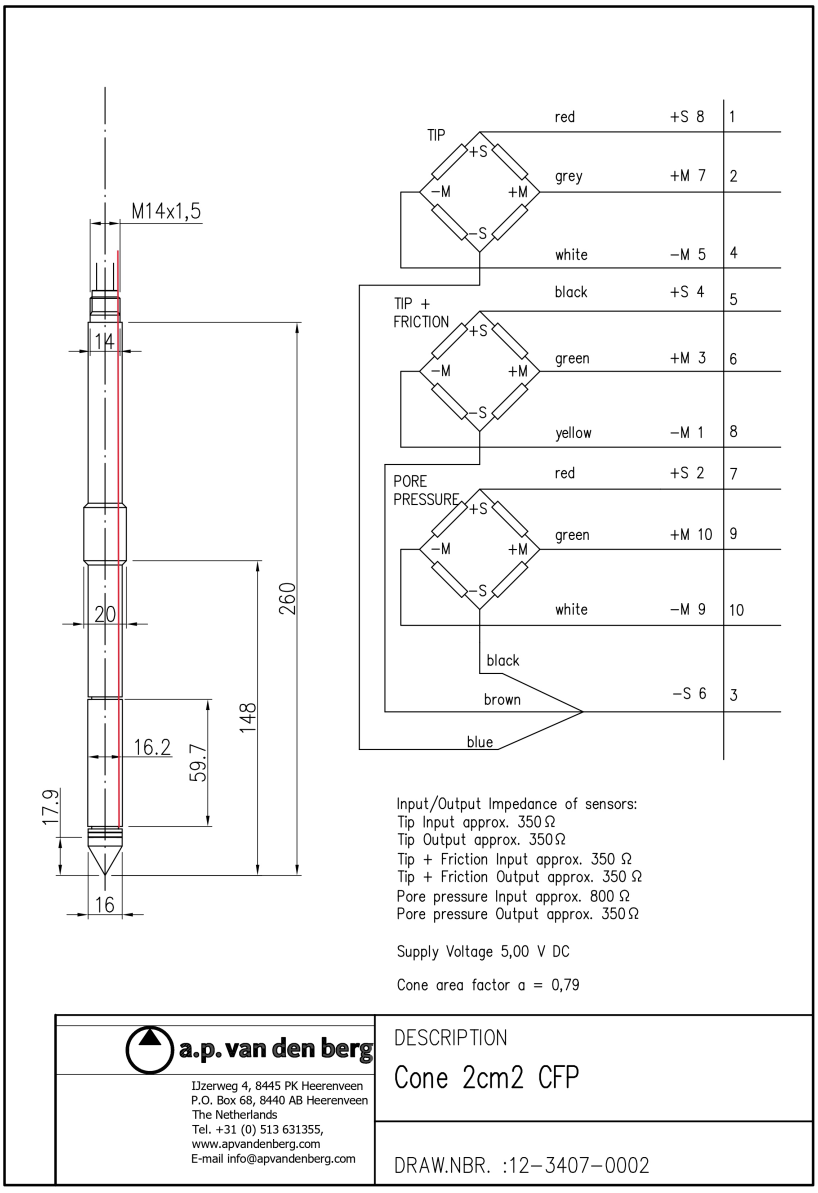


(a) (b)

Figure C.9: a) Configuration to guide the falling weight for impacting on the pile. b) Guide to attach the tube.

Appendix D

Cone drawing



Deze tekening blijft ons eigendom en mag zonder nadrukkelijke toestemming op generlei wijze worden gekopieerd. Auteursrechten voorbehouden volgens de wet.

Figure D.1: Drawing of the cone.

Appendix E
Description of the tests

In the following sections, a detailed description of the tests performed during this research is provided.

E.1. Test 1: Cone penetration test (CPTu)

The piezocone test (CPTu) was pushed into the soil at a constant rate of penetration of 10mm/s by means of the hydraulic plunger (see Figure E.1). During penetration, the total force acting on the cone (Q_c), the total frictional force acting on the sleeve (F_s) and the pore pressure behind the base of the cone (u_2) during penetration were recorded.

The cone resistance (q_c) was obtained from the following correlation:

$$q_c = \frac{Q_c}{A_c} \tag{E.1}$$

Being:	q_c	Cone resistance acting on the cone	[kN]
	Q_c	Total force acting on the cone	[kN]
	A_c	Projected area of the cone	[mm^2]

Moreover, a correction for pore water effects for cone tip and friction sleeve readings (Jamiolkowski et al., 1985) are needed. See equations E.2 and E.4 below. Although the sand fraction of the soil was tested and in clean sands $q_t = q_c$, the net area ratio (a_n) was applied (given by the cone drawings).

$$q_t = q_c + u_2(1 - a_n) \tag{E.2}$$

$$f_s = \frac{F_s}{A_s} \tag{E.3}$$

$$f_t = f_s - \frac{(\pi d_2 t_2 u_2)}{\pi d_c h_s} \tag{E.4}$$

The friction ratio (R_f) was calculated from its definition:

$$R_f = \frac{f_s}{q_t} \times 100 \tag{E.5}$$

Being:	q_t	Corrected cone resistance	[MPa]
	u_2	Pore water pressure measured behind the cone	[kPa]
	a_n	Net area ratio	[-]
	f_s	Sleeve friction	[MPa]
	F_s	Total friction force acting on the sleeve	[kN]
	A_s	Surface area of the sleeve friction	[mm^2]
	f_t	Corrected sleeve friction	[MPa]
	d_2	Internal diameter of the sleeve	[mm]
	t_2	Thickness of friction sleeve	[mm]
	d_c	Diameter of the cone	[mm]
	h_s	Height of the sleeve	[mm]
	R_f	Friction ratio	[%]

After the CPTu, the cyclic loading tests were performed at 0,1 and 1Hz with an amplitude of 10mm at the tip of the cone. During all these tests, the drain was kept opened and the outflow water was measured (see Appendix G).

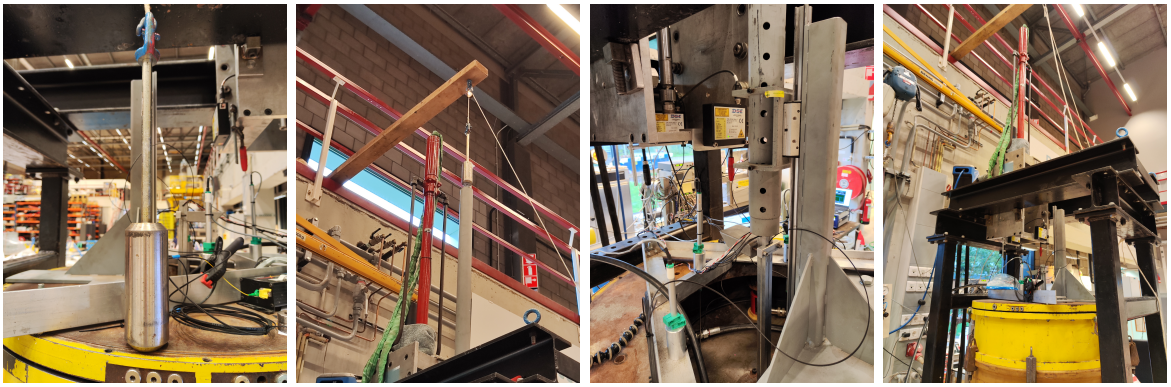


Figure E.1: Cone connected to the hydraulic plunger before starting the test.

E.1.1. Test 2: Impact driving

To drive the pile using impact driving, a weight of 4kg was cyclically and manually dropped by means of a pulley through a 204cm long tube in order to impact on top of the pile. The distance between the gravitational centre of the weight and the top of the pile was between 160 to 167cm. The following Figures E.2a, E.2b and E.2c show the weight and the guiding system used for penetrating the pile.

The load tests performed in between the installation phases consisted in pushing the pile 9mm through the soil. To do so, the manual driving system had to be changed to the hydraulic plunger: the tube was removed and the plunger placed on top of the pile (see Figures E.2d). After the load tests, the manual system could be installed again to continue with the impact driving method. For this test, there was not a specific program to follow, since it would depend on the driving process itself and its progress, but the load tests would be preferably between 8-16D (200 and 400mm) below the top soil.



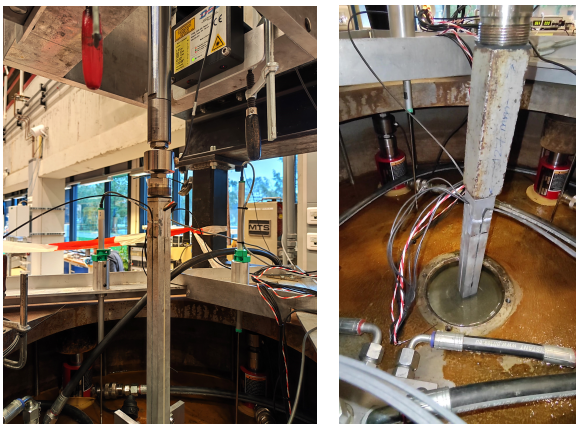
(a) (b) (c) (d)

Figure E.2: a) Weight used for impact driving method. b) Pulley configuration with weight and tube for guiding. c) Guiding system for the tube and instrumented pile before starting the test. d) Hydraulic plunger to push the pile during load tests.

E.1.2. Test 3: Jacking

During jacking, the instrumented pile was pushed through the soil at a constant penetration speed of 10mm/s. To do so, the same hydraulic plunger for the previous tests was used (Figure E.2d).

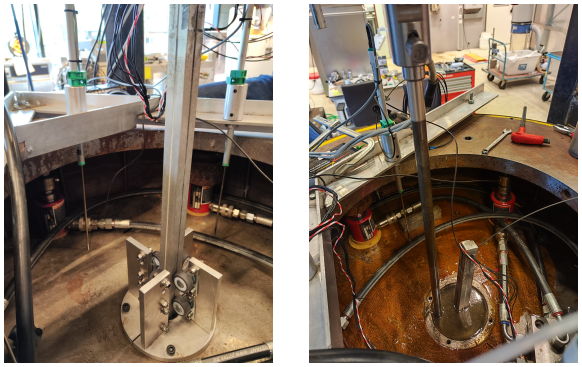
After installation phase 3, an additional loose piece (1kg) was placed in between the base of the plunger and the top of the pile since the stroke of the plunger was too short to push the pile until the last penetration target depth (Figure E.3).



(a) (b)

Figure E.3: a) Contact between plunger and pile by means of a 2mm thick rubber piece in between to soften and better control the displacement rate. b) Extra piece to ensure contact between plunger and top of the instrumented pile.

Since the target penetration depth using the jacking method was not reached and due to the additional space on the top plate because of the error of removing a piece on the top plate to install the rollers for the pile guiding, leading to different boundary conditions than the previous tests, a piezocone (CPTu) test could be performed next to the pile at 10mm/s penetration speed to a final penetration depth of 400mm (Figure E.4). However, the measurements recorded are not included in this report, since the boundary conditions compared to the first CPTu test were different and it was performed due to the larger space in the top plate.



(a) (b)

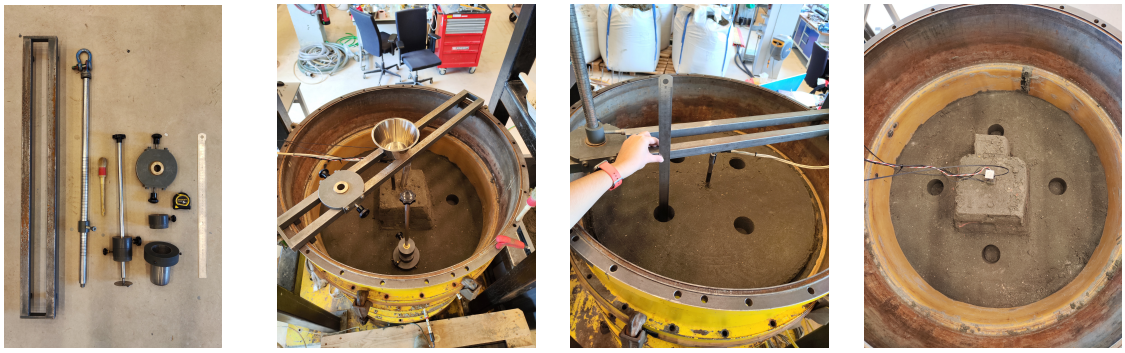
Figure E.4: a) Guiding system consisting of rollers to ensure the verticality of the instrumented pile before being penetrated into the soil and for the first installation phases. b) Cone next to the instrumented pile before penetration.

Appendix F

Relative density

F.1. Relative density, D_{rel}

The samples were all taken using the same guide and mold with diameter 6,63cm and height 5cm, so that the volume of the sample was always the same, 172,62cm^3. After scrapping the soil for the sample, this was oven dried for 1 day to 100ºC. The following Figure F.1 shows the equipment used to take the samples and a photo during the process.



(a) (b) (c) (d)

Figure F.1: a) Equipment used for taking samples; b and c) Photos during the process of taking samples; d) Final result from a layer after excavating 4 samples after Test 1.

The bulk or dry density (ρ_d) and dry unit weight (γ_d) of the samples taken after performing the tests were calculated using equations B.5 and B.6. Then, the void ratio was determined by the following equation:

$$e = \frac{G_s \times \gamma_w - \gamma_d}{\gamma_d} \tag{F.1}$$

Being:	e	Void ratio of the soil sample	[-]
	G_s	Specific gravity of the soil	[-]
	γ_w	Unit weight of water	$[kg/m^3]$
	γ_d	Dry unit weight of the soil sample	$[kN/m^3]$

The following tables summarise all the local measurements obtained from taking the samples during excavation of the models after performing the tests. Three relative density formulations have been used: $D_{rel,1}$ (equation F.2), $D_{rel,2}$ (equation F.3) and $D_{rel,3}$ (equation F.4). The former formulation using the wet method for determination of minimum and maximum densities have been used during the report.

$$D_{rel,1} = \frac{e_{max} - e}{e_{max} - e_{min}} \times 100 \tag{F.2}$$

$$D_{rel,2} = \frac{\rho_{d,max}(\rho_d - \rho_{d,min})}{\rho_d(\rho_{d,max} - \rho_{d,min})} \times 100 \quad \text{(F.3)}$$

$$D_{rel,3} = \frac{\rho_d - \rho_{d,min}}{\rho_{d,max} - \rho_{d,min}} \times 100 \quad \text{(F.4)}$$

Being:

D_{rel}	Relative density of the soil sample	[%]
e	Void ratio of the soil sample	[-]
e_{min}	Minimum void ratio	[-]
e_{max}	Maximum void ratio	[-]

						Using dry method for determining min and max density test			Using wet method for determining min and max density test		
	Sample	**Weight dry soil [g]**	**Bulk density, ρ_t [g/cm^3]**	**Unit weight, γ_t [kN/m^3]**	**Void ratio, e [-]**	**Relative density, $D_{rel,1}$ [%]**	**Relative density, $D_{rel,2}$ [%]**	**Density index, $D_{rel,3}$ [%]**	**Relative density, $D_{rel,1}$ [%]**	**Relative density, $D_{rel,2}$ [%]**	**Density index, $D_{rel,3}$ [%]**
Layer 1	1	276,50	1,60	15,71	0,70	95,84	105,84	107,03	53,96	71,05	68,74
	2	283,30	1,64	16,10	0,66	108,50	118,25	122,53	75,71	92,43	91,62
	3	280,70	1,63	15,95	0,67	103,73	113,58	116,60	67,51	84,38	82,88
	4	276,00	1,60	15,69	0,70	94,89	104,90	105,89	52,32	69,44	67,06
Layer 2	1	289,6	1,68	16,46	0,62	119,70	129,24	136,89	94,94	111,33	112,82
	2	278,7	1,61	15,84	0,68	100,01	109,92	112,04	61,11	78,08	76,15
	3	285,4	1,65	16,22	0,64	112,29	121,97	127,32	82,21	98,82	98,69
	4	281,6	1,63	16,00	0,67	105,40	115,21	118,65	70,37	87,18	85,90
Layer 3	1	224,7	1,30	12,77	1,09	-25,75	-13,42	-11,03	-154,91	-134,22	-105,53
	2	284,6	1,65	16,17	0,65	110,85	120,56	125,49	79,74	96,40	96,00
	3	283,2	1,64	16,09	0,66	108,32	118,08	122,30	75,39	92,12	91,29
	4	285,5	1,65	16,23	0,64	112,47	122,14	127,54	82,52	99,12	99,02

Table F.1: Summary of all the samples obtained excavating the soil per layers after Test 1.

						Using dry method for determining min and max density test			Using wet method for determining min and max density test		
	Sample	**Weight dry soil [g]**	**Bulk density, ρ_t [g/cm^3]**	**Unit weight, γ_t [kN/m^3]**	**Void ratio, e [-]**	**Relative density, $D_{rel,1}$ [%]**	**Relative density, $D_{rel,2}$ [%]**	**Density index, $D_{rel,3}$ [%]**	**Relative density, $D_{rel,1}$ [%]**	**Relative density, $D_{rel,2}$ [%]**	**Density index, $D_{rel,3}$ [%]**
Layer 1	1	282,20	1,63	16,04	0,66	106,50	116,29	120,02	72,26	89,04	87,92
	2	281,60	1,63	16,00	0,67	105,40	115,21	118,65	70,37	87,18	85,90
	3	278,70	1,61	15,84	0,68	100,01	109,92	112,04	61,11	78,08	76,15
	4	285,60	1,65	16,23	0,64	112,65	122,32	127,77	82,83	99,43	99,36
Layer 2	1	280,8	1,63	15,96	0,67	103,92	113,76	116,83	67,83	84,69	83,21
	2	282,8	1,64	16,07	0,66	107,59	117,36	121,39	74,14	90,89	89,94
	3	275,3	1,59	15,65	0,70	93,54	103,58	104,30	50,01	67,17	64,71
	4	285,8	1,66	16,24	0,64	113,01	122,67	128,23	83,44	100,03	100,03
Layer 3	1	280,4	1,62	15,94	0,67	103,18	113,03	115,92	66,56	83,44	81,87
	2	287,3	1,66	16,33	0,63	115,67	125,28	131,65	88,02	104,53	105,08
	3	293,4	1,70	16,67	0,60	126,22	135,64	145,55	106,15	122,34	125,60
	4	284,8	1,65	16,19	0,65	111,21	120,91	125,95	80,36	97,01	96,67

Table F.2: Summary of all the samples obtained excavating the soil per layers after Test 2.

						Using dry method for determining min and max density test			Using wet method for determining min and max density test		
	Sample	**Weight dry soil [g]**	**Bulk density, ρ_t [g/cm^3]**	**Unit weight, γ_t [kN/m^3]**	**Void ratio, e [-]**	**Relative density, $D_{rel,1}$ [%]**	**Relative density, $D_{rel,2}$ [%]**	**Density index, $D_{rel,3}$ [%]**	**Relative density, $D_{rel,1}$ [%]**	**Relative density, $D_{rel,2}$ [%]**	**Density index, I_d [%]**
Layer 1	1	286,20	1,66	16,26	0,64	113,72	123,37	129,14	84,67	101,23	101,38
	2	280,10	1,62	15,92	0,67	102,62	112,49	115,24	65,60	82,50	80,86
	3	286,90	1,66	16,30	0,63	114,96	124,59	130,73	86,80	103,33	103,73
	4	279,70	1,62	15,90	0,68	101,88	111,76	114,32	64,32	81,24	79,51
Layer 2	1	285,5	1,65	16,23	0,64	112,47	122,14	127,54	82,52	99,12	99,02
	2	285,7	1,66	16,24	0,64	112,83	122,50	128,00	83,13	99,73	99,70
	3	287,6	1,67	16,34	0,63	116,20	125,80	132,33	88,93	105,42	106,09
	4	279,7	1,62	15,90	0,68	101,88	111,76	114,32	64,32	81,24	79,51
Layer 3	1	280,6	1,63	15,95	0,67	103,55	113,40	116,38	67,20	84,07	82,54
	2	278,6	1,61	15,83	0,68	99,82	109,74	111,82	60,79	77,77	75,81
	3	280,4	1,62	15,94	0,67	103,18	113,03	115,92	66,56	83,44	81,87
	4	281,7	1,63	16,01	0,66	105,58	115,39	118,88	70,68	87,49	86,24

Table F.3: Summary of all the samples obtained excavating the soil per layers after Test 3.

Appendix G

Additional measurements Test 1

The force acting on the bottom load cells, the membrane pressure to apply the radial stresses, the outflow of water, the forces applied vertically by means of the of the hydraulic jacks to apply the vertical stresses, the displacement of the top plate and the pore pressures were monitored during the test. The following graphs show the results of these measurements from the pressurization phase until the end of Test 1, including the static CPTu and the cyclic loading at 0,1 and 1Hz. Additionally, the full recordings of u_2 are given.

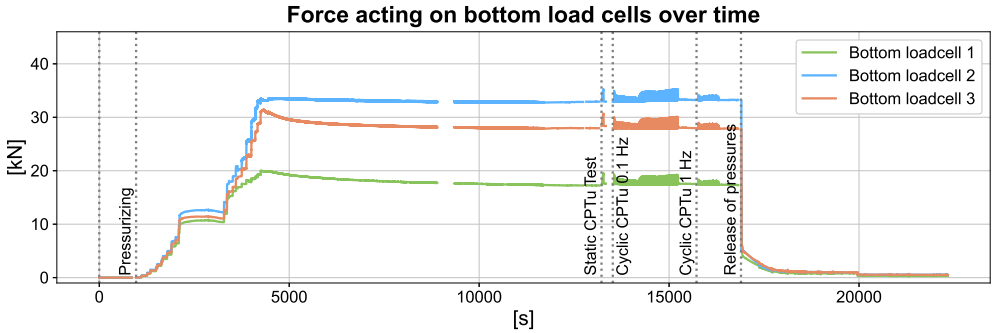


Figure G.1: Bottom load cells measurements over time - Test 1

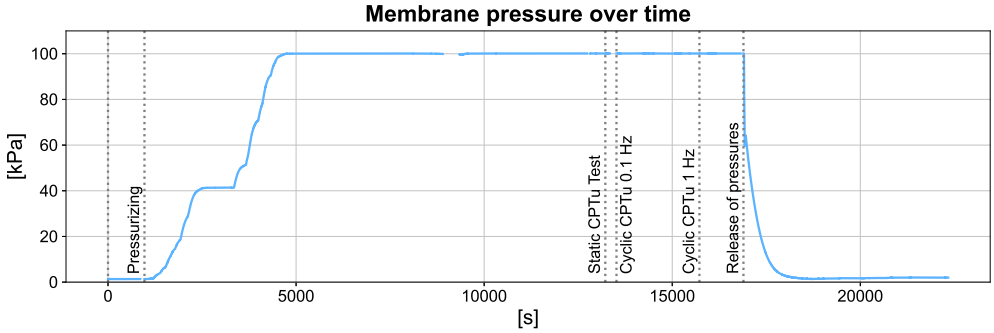


Figure G.2: Membrane pressure measurements over time - Test 1

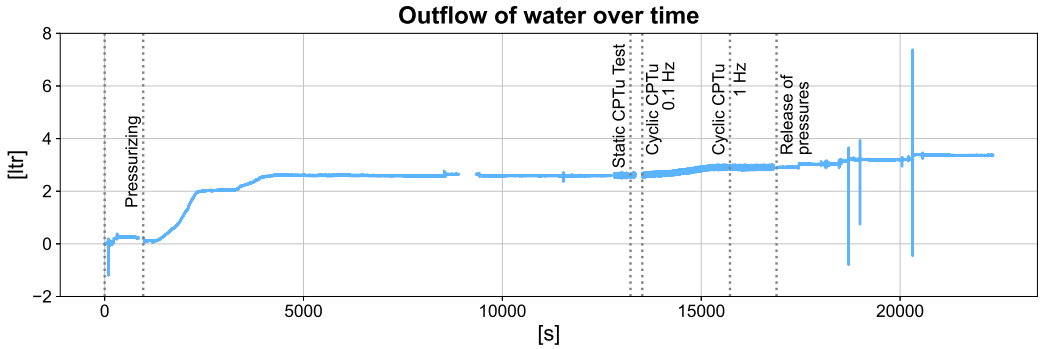


Figure G.3: Outflow of water over time - Test 1

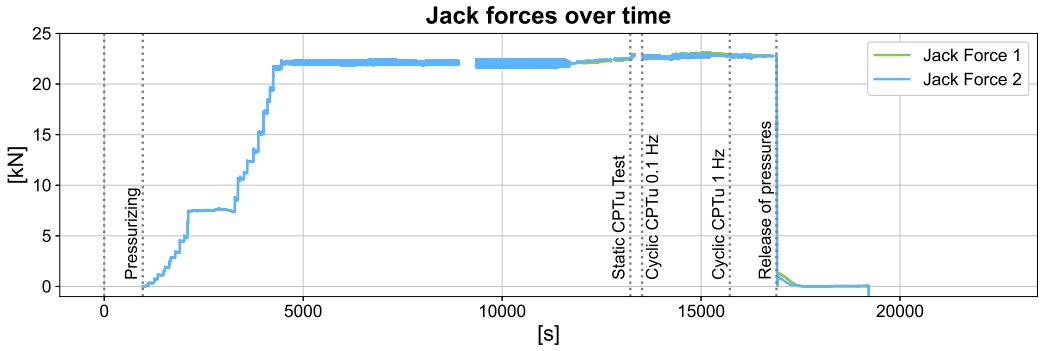


Figure G.4: Jack Forces over time - Test 1

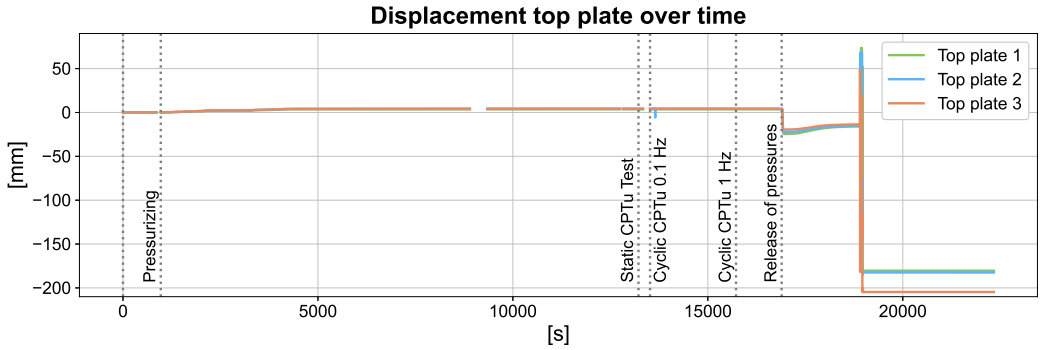


Figure G.5: Displacement top plate over time - Test 1

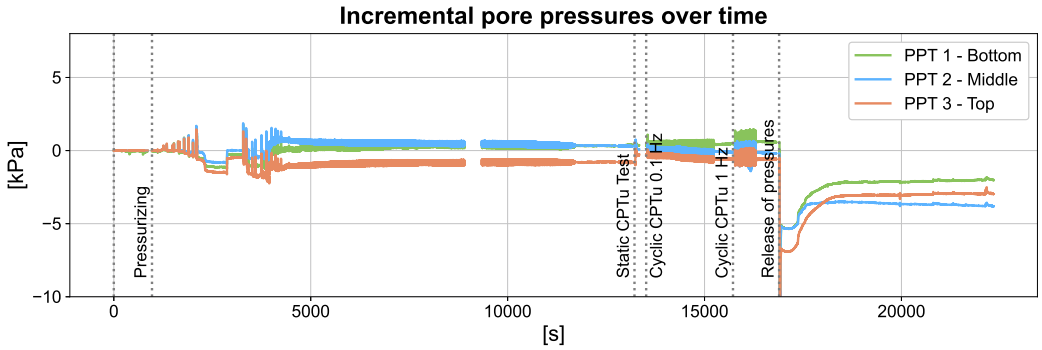


Figure G.6: Pore pressures measured in PPTs over time - Test 1

G.1. Pore pressure, u_2, after static CPTu

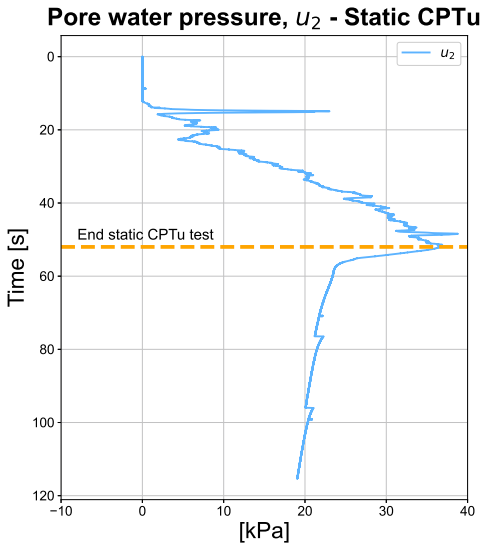


Figure G.7: Pore pressure, u_2, measured during and after static CPTu.

G.2. Pore pressure, u_2, after cyclic CPTu at 0,1 Hz.

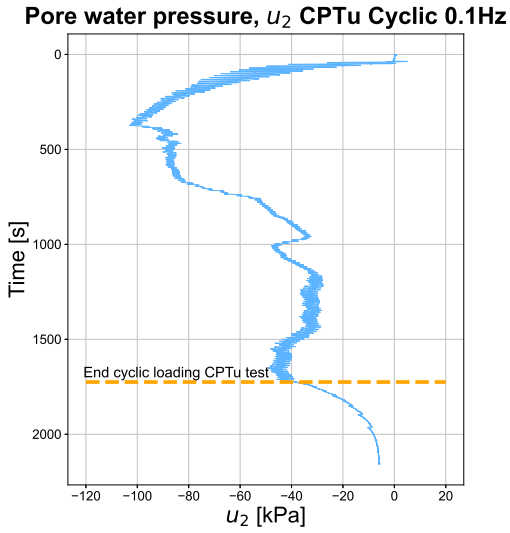


Figure G.8: Pore pressure, u_2, measured during and after cyclic CPTu test at 0,1 Hz.

G.3. Pore pressure, u_2, after cyclic CPTu at 1 Hz.

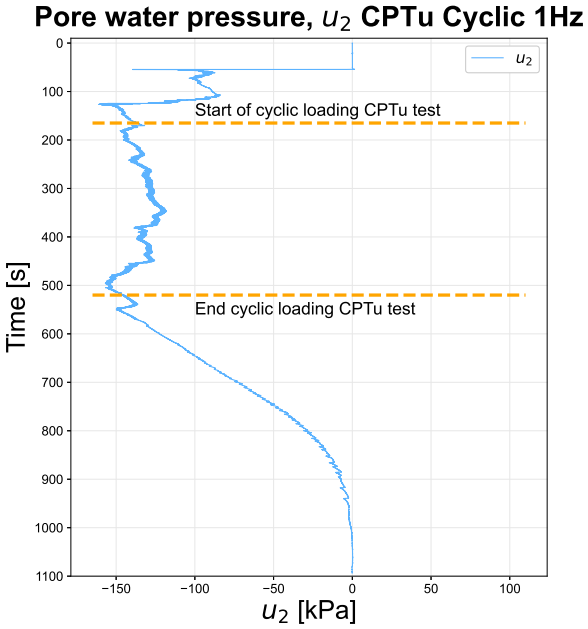


Figure G.9: Pore pressure, u_2, measured during and after cyclic CPTu test at 1 Hz.

Appendix H

Additional measurements Test 2

The force acting on the bottom load cells, the membrane pressure to apply the radial stresses, the outflow of water, the forces applied vertically by means of the of the hydraulic jacks to apply the vertical stresses, the displacement of the top plate and the pore pressures were monitored during the test. The following graphs show the results of these measurements from the pressurization phase until the end of Test 2.

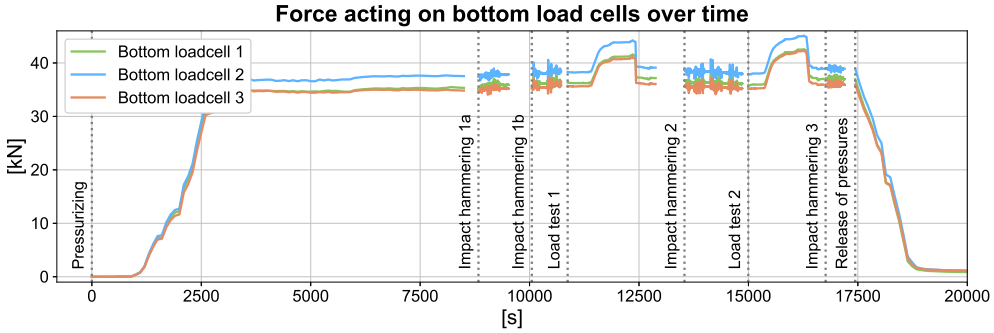


Figure H.1: Bottom load cells measurements over time - Test 2

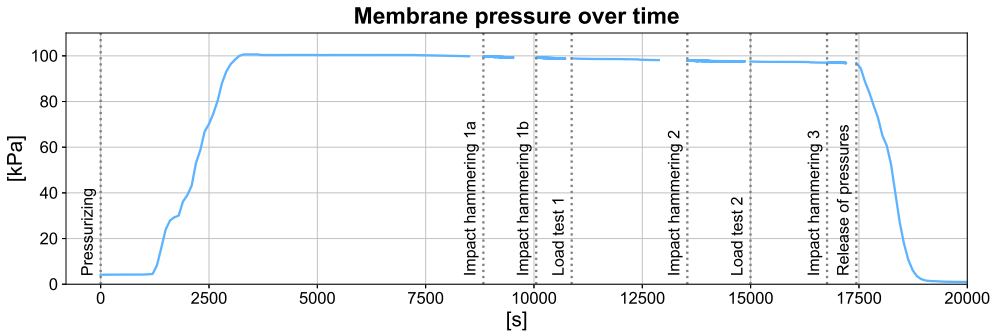


Figure H.2: Membrane pressure over time - Test 2

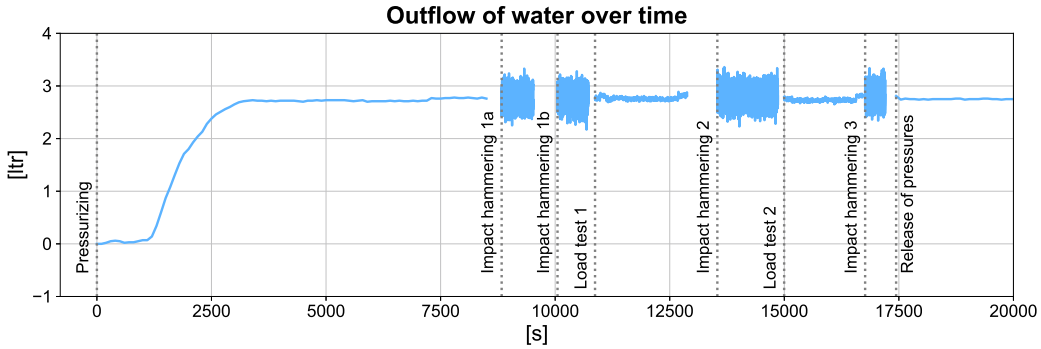


Figure H.3: Outflow of water over time - Test 2

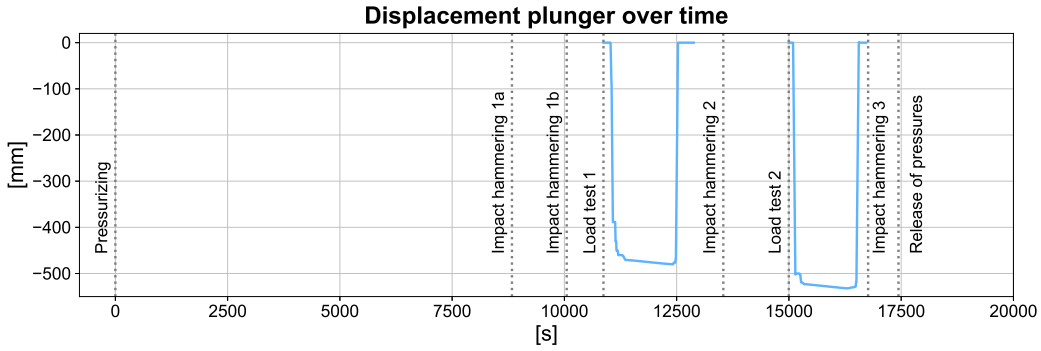


Figure H.4: Displacement of the plunger during load tests over time- Test 2

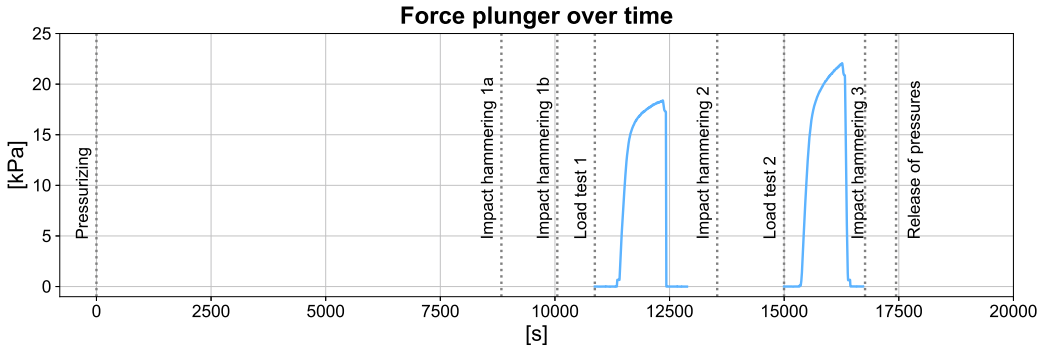


Figure H.5: Force of the plunger during load tests over time- Test 2

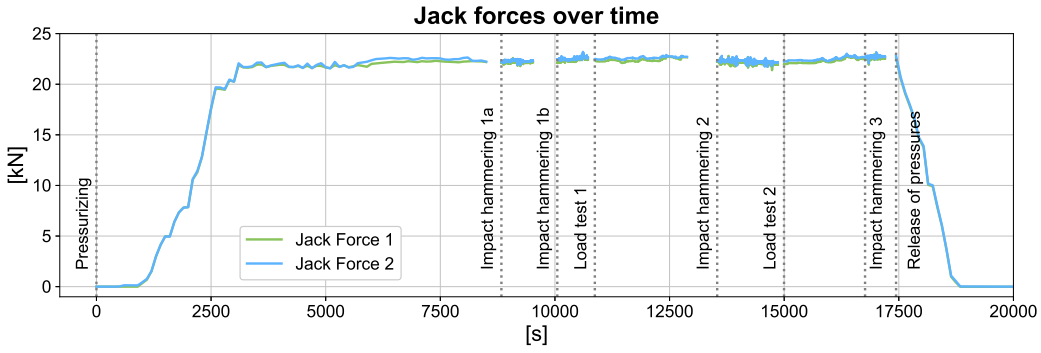


Figure H.6: Jack Forces over time - Test 2

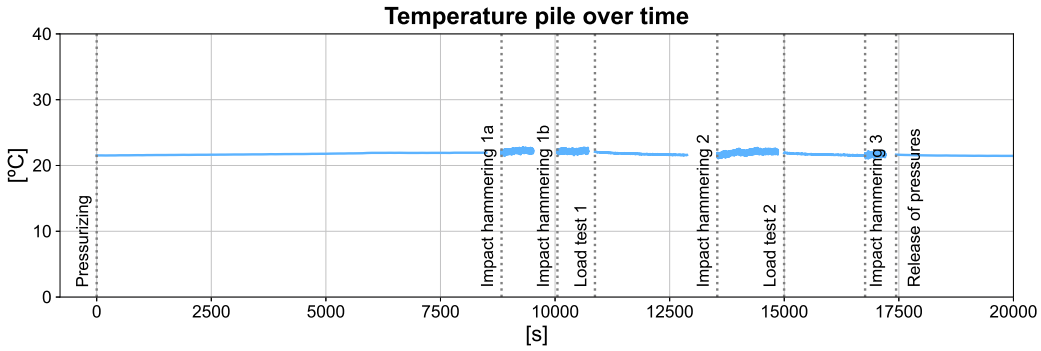


Figure H.7: Temperature of the pile over time - Test 2

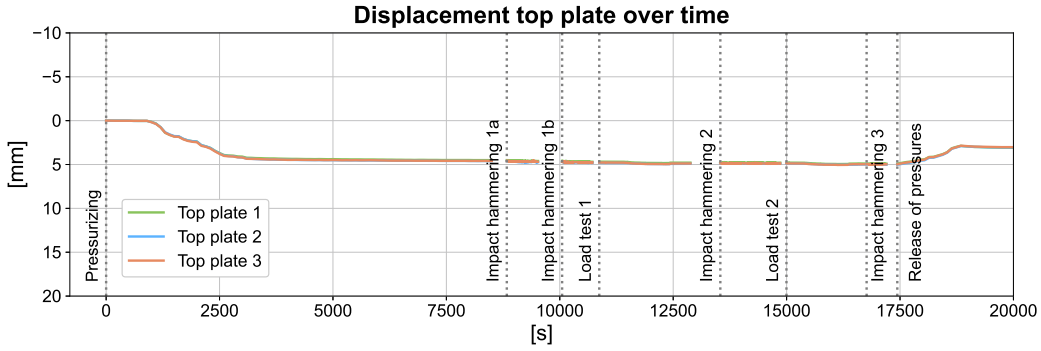


Figure H.8: Displacement top plate over time - Test 2

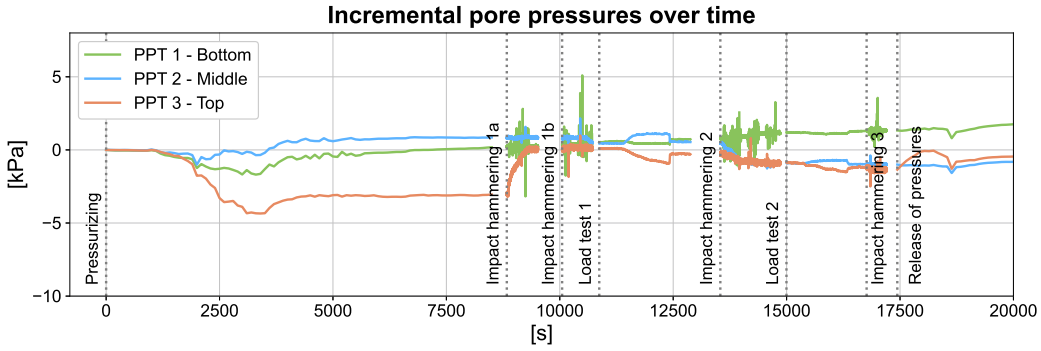


Figure H.9: Pore pressures measured in PPTs over time - Test 2

Appendix I

Additional measurements Test 3

The force acting on the bottom load cells, the membrane pressure to apply the radial stresses, the outflow of water, the forces applied vertically by means of the of the hydraulic jacks to apply the vertical stresses, the displacement of the top plate and the pore pressures were monitored during the test. The following graphs show the results of these measurements from the pressurization phase until the end of Test 3, including the jacking installation and the CPTu.

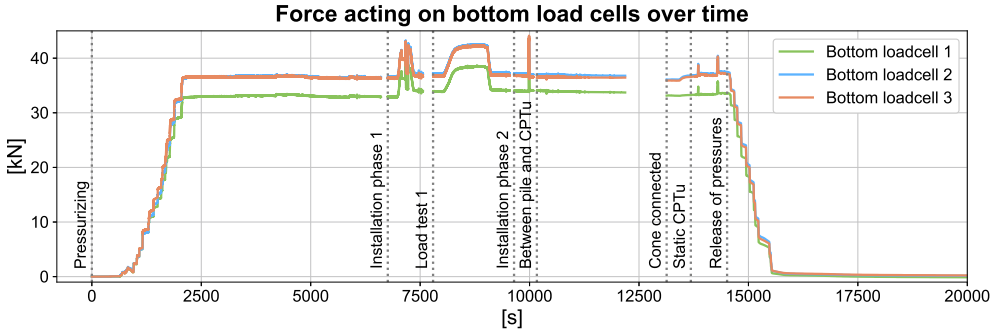


Figure I.1: Bottom load cells measurements over time - Test 3

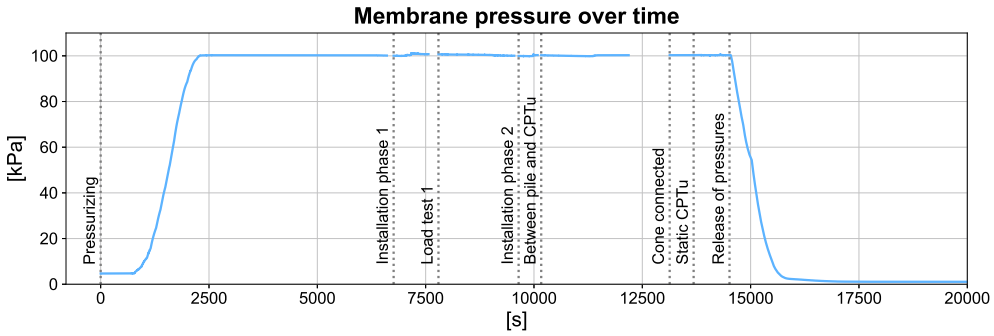


Figure I.2: Membrane pressure over time - Test 3

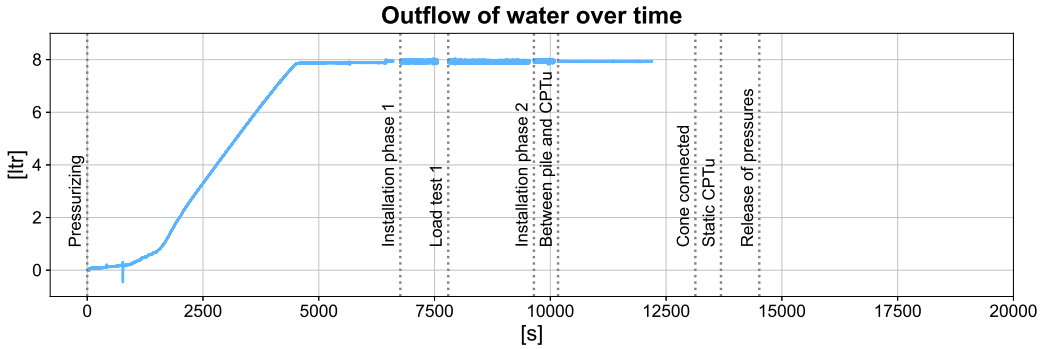


Figure I.3: Outflow of water over time - Test 3

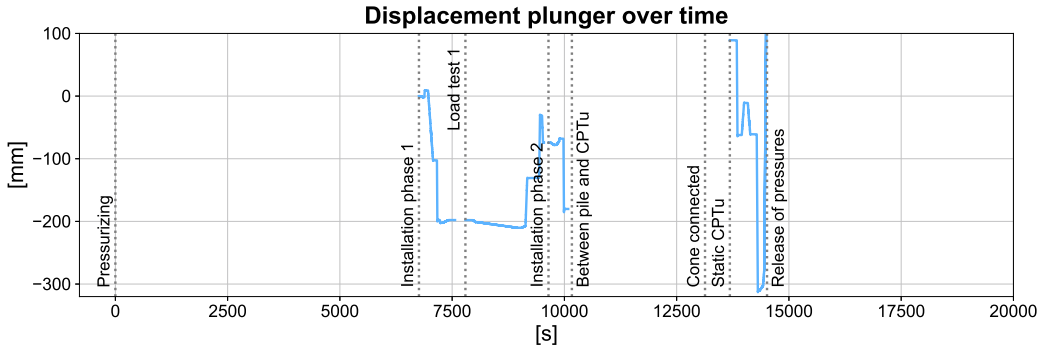


Figure I.4: Displacement of the plunger during load tests over time- Test 3

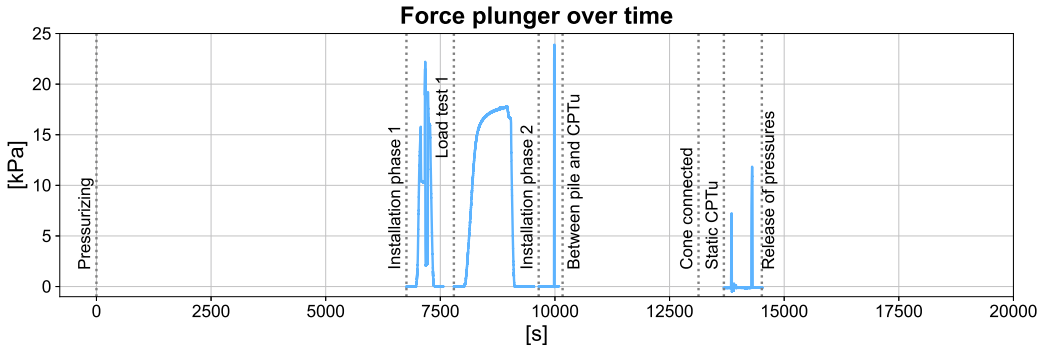


Figure I.5: Force plunger over time- Test 3

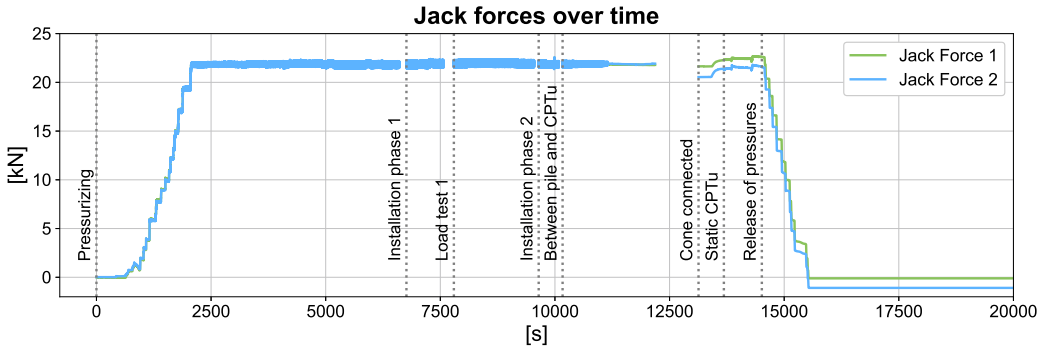


Figure I.6: Jack Forces over time - Test 3

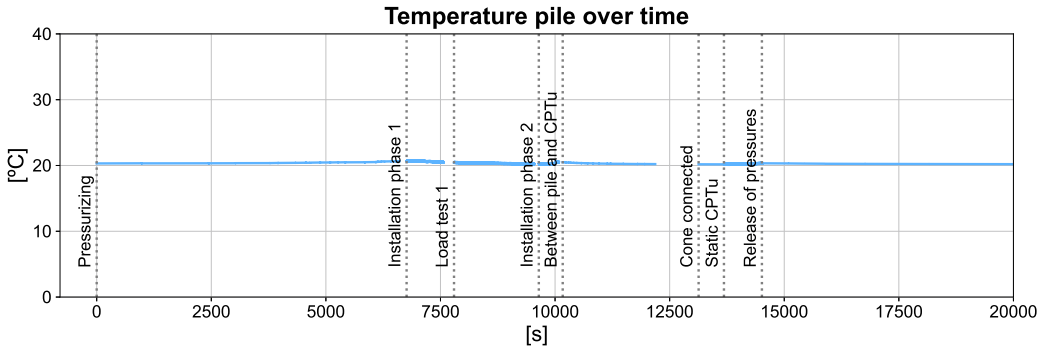


Figure I.7: Temperature of the pile over time - Test 3

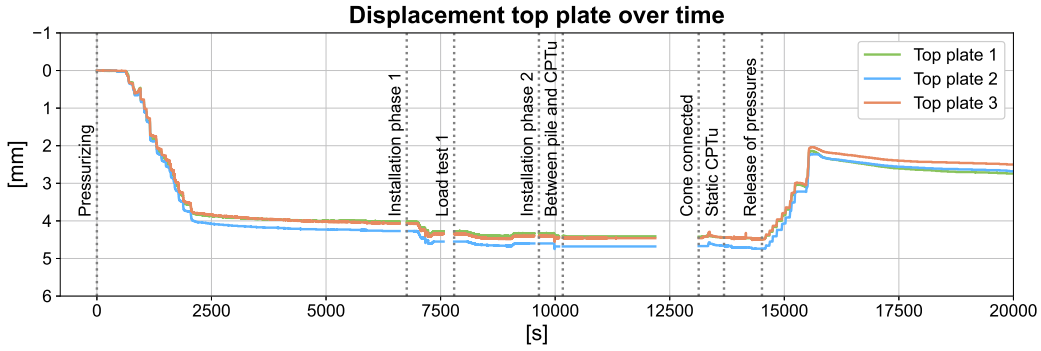


Figure I.8: Displacement top plate over time - Test 3

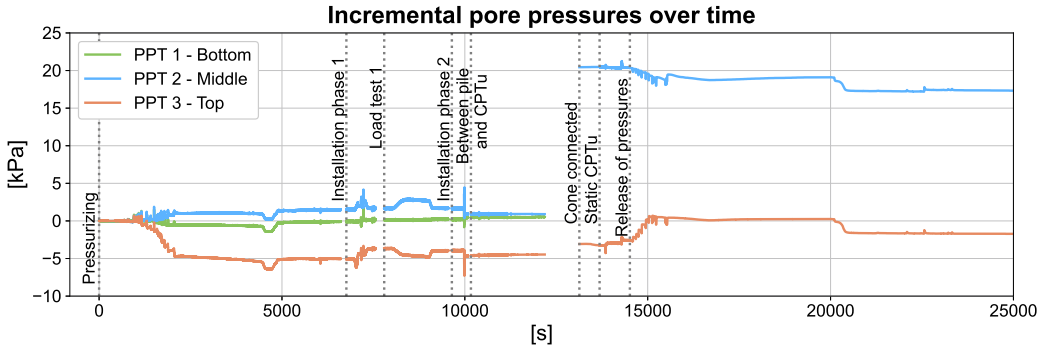


Figure I.9: Pore pressures measured in PPTs over time - Test 3